IPR-06-25

Äspö Hard Rock Laboratory

Reduction of hexavalent chromium by green rust sulphate: determination of end product and reduction mechanism

Lone Lindbæk Skovbjerg

Master Thesis accepted by the
Geological Institute
University of Copenhagen

April 2005

Svensk Kärnbränslehantering AB
Swedish Nuclear Fuel
and Waste Management Co
Box 5864
SE-102 40 Stockholm Sweden
Tel 08-459 84 00
+46 8 459 84 00
Fax 08-661 57 19
+46 8 661 57 19

Äspö Hard Rock
Laboratory

Report no.	No.
IPR-06-25	F123K
Author	Date
Lone Lindbæk Skovbjerg	April 2005
Checked by	Date
John Smellie	November 2006
Approved	Date
Anders Sjöland	2006-11-29

Äspö Hard Rock Laboratory

Reduction of hexavalent chromium by green rust sulphate: determination of end product and reduction mechanism

Lone Lindbæk Skovbjerg

Master Thesis accepted by the
Geological Institute
University of Copenhagen

April 2005

Keywords: Green Rust, Chromium, Redox

Reduction of Hexavalent Chromium by Green Rust Sulphate:

Determination of End Product and Reduction Mechanism

Master Thesis in Geology

Lone Lindbæk Skovbjerg

Advisor
Susan L. S. Stipp

Geological Institute
University of Copenhagen
April 2005

Sammanfattning

Cr (VI) är ett cancerogent ämne som ibland läcker ut från industrier eller från flygaska till jord och grundvatten. Den är löslig och giftig i låga koncentrationer. Cr(III) däremot anses vara ogiftig även vid höga koncentrationer och är ett viktig spårelement i däggdjurens ämnesomsättning. Av denna anledning försöker man reducera Cr(VI) till Cr(III) i samband med rening av grundvatten och spillvatten. Grön rost (GR), en lageruppbyggd Fe(II)-Fe(III) hydroxid med anjoner och vatten i mellanlagren har visat sig kunna reducera Cr(VI) till Cr(III) snabbt och effektivt. För att optimera grön rost som ett potentiellt reningsmedel är det nödvändigt att förstå denna reaktion.

I denna studie har GR-sulfat fått reagera med Cr(VI). För att karakterisera den kemiska sammansättningen, strukturen och morfologin hos mellan- och slutprodukter makroskopiskt såväl som vid hög upplösning har följande tekniker använts: Röntgendiffraktion (XRD), atomär mikroskopi (AFM), transmissions elektron mikroskopi (TEM) med tillhörande tekniker: scanning TEM (STEM), röntgenenergi dispersiv spektroskopi (XEDS) samt elektrondiffraktion från utvalt område (SAED). Vid reaktion med Cr(VI) bildas initiellt Cr(III)-substituerad ferrihydrit och götit. Götit har låg löslighet och inkorporering av Cr(III) i kristallstrukturen sänker lösligheten ytterligare, därför utgör götit en effektiv deponi för trivalent krom.

Resultaten antyder följande mekanism: kromat byggs in i mellanlagren hos GR där det reduceras genom elektronöverföring från Fe(II) i hydroxidlagren. Samtidigt rör sig elektroner över Fe(II)-Fe(III)-hydroxidlagren för att reducera Cr(VI) som är absorberat på ytan. Båda mekanismerna är mycket snabba beroende på GR-sulfatets strukturella och kemiska natur. Tidigare publicerade studier visar att kromatreduktion med karbonatformen av GR huvudsakligen sker på ytan, varvid ett tunt lager av Cr(III) fälls ut på ytan av den trevärda slutprodukten av Fe. Krom bundet till ytan av en trevärd järnförening riskerar att hamna i miljön i större grad än krom bundet till strukturen hos svårlöst götit. Om man därför tänker använda GR för borttagning av Cr(VI) bör man använda GR-sulfat i stället för GR-karbonat.

Contents

1 ABSTRACT 3

2 RESUMÉ 4

3 INTRODUCTION 5

4 BACKGROUND 8

4.1 CHROMIUM 8

4.1.1 History, Properties and Behaviour 8

4.1.2 Use of Chromium 9

4.1.3 Release of Chromium to the Environment 12

4.1.4 Redox Cycle of Chromium 13

4.2 GREEN RUST 15

4.2.1 Green Rust Structure 16

4.2.2 Synthesis of Green Rust 20

4.2.3 Reactivity of Green Rust Compared to Other Fe(II)-Bearing Compounds 21

4.2.4 Green Rust Reduction of Various Compounds and Elements 23

5 TECHNIQUES AND EXPERIMENTAL DETAILS 29

5.1 METHODS AND MATERIALS 29

5.1.1 Glove Box and Glove Bag 29

5.1.2 Synthesis of Green Rust 30

5.1.3 Reacting GR with Cr(VI) 33

5.2 TECHNIQUES AND SAMPLE PREPARATION 35

5.2.1 X-Ray Diffraction (XRD) 36

5.2.2 Atomic Force Microscope (AFM) 42

5.2.3 Transmission Electron Microscopy (TEM) 46

5.3 UNCERTAINTIES AND REPRODUCIBILITY 55

5.3.1 Uncertainty Related to the Experimental Set Up 55

5.3.2 Reproducibility of Observations 56

6 GREEN RUST SYNTHESIS 58

6.1 SYNTHESIS OF GR_{SO4} 58

6.2 TREATMENT OF GREEN RUST BEFORE REACTION WITH CHROMATE 65

7 GREEN RUST SULPHATE INTERACTION WITH CHROMATE 67

7.1 RATES OF REACTIONS 67

7.1.1 General observations 67

7.1.2 Published Rates of Reaction 68

7.1.3 Conclusions About Rates of Reaction 72

7.2 END PRODUCT 75

7.2.1 End Product Obtained in This Work 76

7.2.2 End Products in The Literature 91

7.2.3 Conclusions About End Products 93

7.3 MECHANISM 95

7.3.1 Stage I - Reduction of Cr(VI) 95

7.3.2 Stage II - Formation of Cr-Goethite in GR Morphs 96

7.3.3 Mechanisms in The Literature 97

7.3.4 Conclusions About Mechanism 98

8 CONCLUSION 99

8.1.1 Implications 100

8.1.2 Future work 100

9 ACKNOWLEDGEMENTS 101

10 REFERENCES 102

11 APPENDICES 108

11.1 APPENDIX A 108

11.1.1 Solution Data 108

11.2 APPENDIX B 109

11.2.1 Measured Chemical Values 109

11.3 APPENDIX C 110

11.3.1 Pourbaix Equations 110

1 ABSTRACT

Cr(VI) is a known carcinogenic contaminant sometimes leaked from industry or leached from fly ash to soil and groundwater. It is soluble and toxic in low concentrations. Cr(III) is considered nontoxic, even in relatively high concentrations and is an important trace metal in mammalian metabolism. Therefore, groundwater remediation and waste water treatment seeks to reduce Cr(VI) to Cr(III). Green rust, a layered, mixed-valent iron hydroxide with anions and water in the interlayers, is known to reduce Cr(VI) to Cr(III) quickly and effectively. In order to optimise the potential of green rust as a remediation agent, understanding about the reaction is necessary.

In this study, green rust sulphate was reacted with chromate. The following techniques were used to characterize the composition, structure and morphology of the intermediate and end products at bulk and high-resolution: X-ray diffraction (XRD), atomic force microscopy (AFM), transmission electron microscopy (TEM) with associated techniques: scanning TEM (STEM), X-ray energy dispersive spectroscopy (XEDS) and selected area electron diffraction (SAED). Upon reaction with Cr(VI), Cr(III)-substituted ferrihydrite is initially produced together with Cr(III) substituted goethite. When left in solution, the ferrihydrite dissolves and re-precipitates as Cr(III)-substituted goethite. Goethite has low solubility and the incorporation of Cr(III) into the crystal structure decreases solubility even more, so goethite is an effective sink for trivalent chromium.

The results suggest the following mechanism: Chromate is exchanged into the interlayer of green rust where it is reduced by electron transfer from Fe(II) in the hydroxide layers. Simultaneously, electrons move across the layers of iron(II-III) hydroxide to reduce Cr(VI) adsorbed at the solid-solution interface. Both mechanisms are very fast because of the structural and chemical nature of green rust sulphate. In contrast, previously published studies reported that reduction of chromate by the carbonate form of green rust takes place mostly at the surface, resulting in precipitation of a thin Cr(III) surface layer on the ferric end product. Chromium, bound at the surface of a ferric compound, risks to return to the environment more than chromium bound in the structure of sparingly soluble goethite. Therefore, if green rust is considered for remediation of Cr(VI), efforts should be made to use green rust sulphate preferentially over green rust carbonate.

2 RESUMÉ

Cr(VI) er et kræftfremkaldende forureningsstof der sommetider udledes fra industrivirksomheder eller siver fra flyveaske til jord og grundvand. Det er letopløseligt og giftigt i lave koncentrationer. Cr(III) er ugiftigt, selv i relativt høje koncentrationer og det er et vigtigt sporelement i pattedyrs stofskifte. Man søger derfor at reducere Cr(VI) til Cr(III) i forbindelse med grundvands- og spildevandsrensning. Grøn rust, et lagdelt Fe(II)-Fe(III) hydroxid med anioner og vand i mellemlagene, har vist sig at kunne reducere Cr(VI) til Cr(III), hurtigt og effektivt. For at optimere grøn rust som et potentielt rensnings-stof, er det nødvendigt at forstå reaktionen.

I dette studium blev Cr(VI) bragt til at reagere med grøn rust sulfat. Følgende teknikker blev anvendt for at karakterisere den kemiske sammensætning, strukturen og morfologien af mellem- og slutprodukter makroskopisk såvel som ved høj opløsning: Roengent diffraktion (XRD), atomar kraft mikroskopi (AFM), transmission elektron mikroskopi (TEM) med associerede teknikker: skannende TEM (STEM), Roengent energi sprednings spektroskopi (XEDS) samt udvalgt-område elektron diffraktion (SAED). Ved reaktion med Cr(VI) dannedes Cr(III) - substitueret ferrihydrit og goethit. Når suspensionen fik lov at stå, blev ferrihydriten dog opløst og genudfældet som Cr(III)-substitueret goethite. Goethit er lavtopløseligt og inkorporeringen af Cr(III) i crystal strukturen sænker opløseligheden yderligere, så goethit kan betragtes som et effektivt depot for trivalent krom.

Resultaterne antyder følgende mekanisme: kromat diffunderer ind i mellemlagene i grøn rust hvor det reduceres. Samtidig bevæger elektroner sig på tværs af Fe(II)-Fe(III) hydroxid lagene for at reducere Cr(VI), der er adsorberet på overfladen. Begge mekanismer er meget hurtige på grund af sulfat grøn rusts strukturelle og kemiske natur. Tidligere publicerede studier indikerede derimod at krom reduktion ved karbonat formen af grøn rust hovedsageligt foregår på overfladen, hvorved et tyndt Cr(III) lag udfældes på overfladen af det ferritiske slutprodukt. Krom er mere udsat for at vende tilbage til miljøet når det er bundet i et overfladelag end når det er strukturelt bundet i goethit. Hvis man overvejer at bruge grøn rust i forbindelse med grundvands- eller spildevandsrensning for Cr(VI), bør man derfor benytte sulfat grøn rust frem for karbonat grøn rust.

3 INTRODUCTION

Chromium was discovered and named at the end of the 18th century by Vauquelin (1797, as cited by Lipscher and Douma, 2004a) and was in the beginning chiefly utilised as yellow and orange pigment in paints (Lipscher and Douma, 2004 a, b). Since then use has broadened. Chromium is now important in a wide range of industries. The major consumer of chromium today is the steel industry. Stainless steel contains from 12 to 30% Cr (Sandvik, 2004). Other industrial uses of Cr include wood preservation, treatment of metal and plastic surfaces, leather tanning and alloy fabrication. The extensive and often careless use of chromium compounds has led to severe contamination of water resources, soils and sediments. Chromium is released to air and water during manufacturing and to water and soil when chromium-containing products are used or deposited as waste. The toxicity of chromium depends on its oxidation state. Chromium has several oxidation states: 0, II, III and VI, but Cr(III) and Cr(VI) are by far the most common in the natural environment. Cr(VI) poses a severe threat to humans and animals. On inhalation, it can cause nasal discomfort, such as nosebleed and ulcers. Ingestion of larger amounts may lead to stomach ulcers, kidney and liver damage and even death. Cr(VI) present in leather can cause skin irritation and allergy. However it is cancer that poses the biggest threat of long-time exposure to Cr(VI), such as might happen if one drinks contaminated water. Cr(III) on the other hand is an essential trace nutrient, active in metabolism. To be considered toxic, Cr(III) needs to be present in much higher concentrations than does Cr(VI).

Because Cr(III) is considerably less toxic than Cr(VI), reduction of Cr(VI) to Cr(III) is preferred in remediation as opposed to adsorbing Cr(VI) to a substrate from where it may easily desorb. Furthermore Cr(VI) compounds are often highly soluble whereas Cr(III) tends to form sparingly soluble compounds or strong complexes with soil minerals under most pH conditions. The current literature describes experiments with several types of natural materials as Cr(VI) reductants, mostly reduced species of sulfur, iron and organic carbon. These reductants have proven effective to varying degrees, depending on environmental factors such as pH, the redox potential of the surroundings and availability of light and water. Among the more effective agents over a wide range of conditions is reduced iron as Fe(0), aqueous Fe^{2+} and Fe(II) structurally bound in minerals.

Green rust (GR) is a layered double hydroxide with structurally bound Fe(II). Its existence outside laboratories has only recently been verified (Koch & Mørup, 1991, Trolard et al., 1997), probably as a result of its very short lifetime in oxidising conditions. When exposed to air, Fe(II) oxidises to Fe(III), causing structural breakdown and transformation of the green rust into commonly-known red rust, such as ferrihydrite, lepidocrocite or goethite. During recent years, green rust has received a lot of attention because of its ability to reduce oxidised compounds such as NO_2^- (Hansen et al., 1994), NO_3^- (Hansen et al., 2001), Se(VI) (Myneni et al., 1997), U(VI) (O'Loughlin et al., 2003), TCE (Lee & Batchelor, 2002) and also Cr(VI) (Loyaux-Lawniczak et al., 1999; Loyaux-Lawniczak et al., 2000; Williams and Scherer, 2001; Bond and Fendorf, 2003; Legrand et al., 2004a). The reactions with synthesised GR are generally fast, even at ambient temperatures. GR is generally considered to be an active compound in permeable reactive barriers (PRBs) that are based on metallic iron. Fe-PRBs are often made with about 5% fine-grained recycled iron, dug down in trenches perpendicular to groundwater flows with migrating plumes of contamination. GR has been identified as a corrosion product in such a barrier (Philips et al., 2003) and assurance of its presence may enhance the long-term performance of PRBs.

In addition to Fe(II), GR also contains structural Fe(III), OH^-, H_2O, an anion and a cation (Christiansen et al., in progress). In synthetic samples used in reduction experiments, the anions are typically SO_4^{2-}, CO_3^{2-} or Cl^- and they determine the overall structure and reduction potential of the GR. Structure and chemical composition of chloride and sulphate forms of GR have been proposed (Refait et al., 1998; Simon et al., 2003), but much about GR structure and reactivity is still being debated. This makes modeling and prediction difficult, leading to somewhat diffuse or confusing concepts in the literature. Rates of reduction by the various green rust types have been studied leading to quite different models. A variety of results have similarly been presented regarding the end product obtained after redox reactions, including reduction of Cr(VI), and some of the interpretations are conflicting. This is an important point, because the end product has major influence on the fate of the reduced compound, so the properties of that compound influence the kind of action taken in a specific contaminated site. Possibilities for controlling mechanisms have likewise been made but often with little experimental evidence to support the conclusions. By investigating the reaction between GR_{SO4} and chromate, some of these issues may be illuminated.

The purpose of this work is: i) to characterise the oxidised end product when green rust is oxidised by Cr(VI) and ii) to propose a mechanistic model for Cr(VI) reduction by green rust sulphate. The overall reactions and solid products have been characterised with traditional wet chemistry methods and capillary tube X-ray diffraction (CT-XRD). Understanding of molecular scale behaviour has been obtained using high-resolution techniques namely atomic force microscopy (AFM), transmission electron microscopy (TEM) and its associated techniques: Scanning TEM (STEM), selected area electron diffraction (SAED) and X-ray energy dispersive spectroscopy (XEDS).

4 BACKGROUND

4.1 CHROMIUM

4.1.1 History, Properties and Behaviour

As early as 1766, Johann Gottlob Lehmann performed chemical experiments with the chromium-containing red mineral, crocoite ($PbCrO_4$), which was mined together with gold, silver, copper and lead in the Ural Mountains, Siberia. He did not get very far, though, because he died the following year in a laboratory explosion. In 1797, Nicolas-Louis Vauquelin set out to find the chemical composition of this beautiful and rare mineral. He dissolved crocoite, and mixed the solutions with all sorts of reagents. The resulting phases showed strong colors of yellow, red and green giving rise to the name chromium, from the Greek word “khroma” meaning color. In 1798, Vauquelin obtained metallic chromium (Trapp, 2002).

Chromium is number 24 in the modern periodic table of elements and in its ground state, it has the following electron configuration: $[Ar]3d^5 4s^1$ in its ground state. It has four energy levels with an unpaired electron in both the outermost and second outermost levels (Figure 4.1). The orbitals in the 3d-shell and the 4s-shell are only partially filled, with one electron in each of the five d-orbital positions and one in the outermost s-orbital. This configuration gives rise to several oxidation states and is responsible for the many colors of chromium compounds. Electrons can be excited, i.e. made to jump to a higher energy level, by absorbing energy from the surroundings. Colours may be produced when the electrons fall back again to their non-excited state. In the case of chromium, the light-prouducing jump occurs between orbitals of the same subshell, i.e. 3d. The orbitals, which

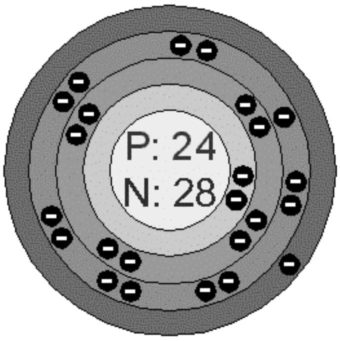

Figure 4.1: Electron configuration of chromium atom (from Bentor, 2005).

have the same energy in the zero-valent atom, obtain two different energy levels when Cr forms bonds with anions, where sharing of electrons takes place. Depending on how many anions surround the Cr atom (e.g. four when Cr is tetrahedrally coordinated and six when Cr is octahedrally coordinated etc.), the five orbitals respond differently. According to crystal field theory, three of the five orbitals feel the electrons from the anions when Cr is tetrahedrally coordinated and so obtain higher energy than the remaining two orbitals. This is referred to as crystal field splitting. An electron jump between these two energy levels requires an amount of energy that lies within the visible spectrum of light $(4\times10^{-7} < \lambda \text{ (m)} < 7\times10^{-7})$ so when the electron falls back again, light is emitted (Klein and Hurlbut, 1999). The stability of chromium, in its various oxidation states, is illustrated in Figure 4.2 as a function of pH and Eh.

It has been known for quite a while, that exposure to Cr(VI) can cause cancer in mammals. It is suspected to be mutagenic, meaning it can change the genetic information, usually DNA, and cause the frequency of mutations to increase. Chromium is also suspected to be teratogenic, meaning it can cause physical defects in mammal embryos. Chromate, CrO_4^{2-}, and dichromate, $Cr_2O_7^{2-}$, are oxidising agents often used in laboratories to clean organic material from the surfaces of glassware. This may lead to the assumption that when Cr(VI) compounds come into contact with the organic matter of living beings, it reacts in a harmful way. Cr(III) on the other hand is an important trace metal for organism function. It aids the hormone, insulin, in sugar metabolism (Chromiuminfo, 2004). Not only is Cr(VI) more toxic than Cr(III), it is also much more mobile in the environment, adding to the danger of this species. Table 4.1 compares the solubility of various Cr compounds

4.1.2 Use of Chromium

Industrial demand for chromium, in its various oxidation states, has continued to increase through the last century. In 2001, world Cr production was almost 4 million metric tonnes (t) (Goonan and Papp, 2003). Chromium does not exist in nature as free metal, but rather as a constituent in composite minerals. The only chromium ore is chromite ($FeCr_2O_4$). Chromium minerals, such as crocoite ($PbCrO_4$), are too rare to be of commercial value as chromium ores. Chromite is one of the first minerals to separate from a cooling magma and is usually associated with ultrabasic rocks such as peridotites and serpentines derived therefrom. (Klein & Hurlbut, 1999). It is mined in many countries, but more than 90% of chromite comes from South Africa, Kazakhstan, India, Brazil, Finland, Turkey and Zimbabwe (Hoffmann et al. 2002). The major part of this production is consumed by the steel industry. Steel is an alloy based on iron and is often mixed with various metals such as nickel and molybdenum to obtain specific properties such as strength, malleability and corrosion resistance. When iron is mixed with more than 12% Cr, the alloy becomes corrosion resistant and is termed stainless steel (Sandvik, 2004). A film of a few atomic layers thickness

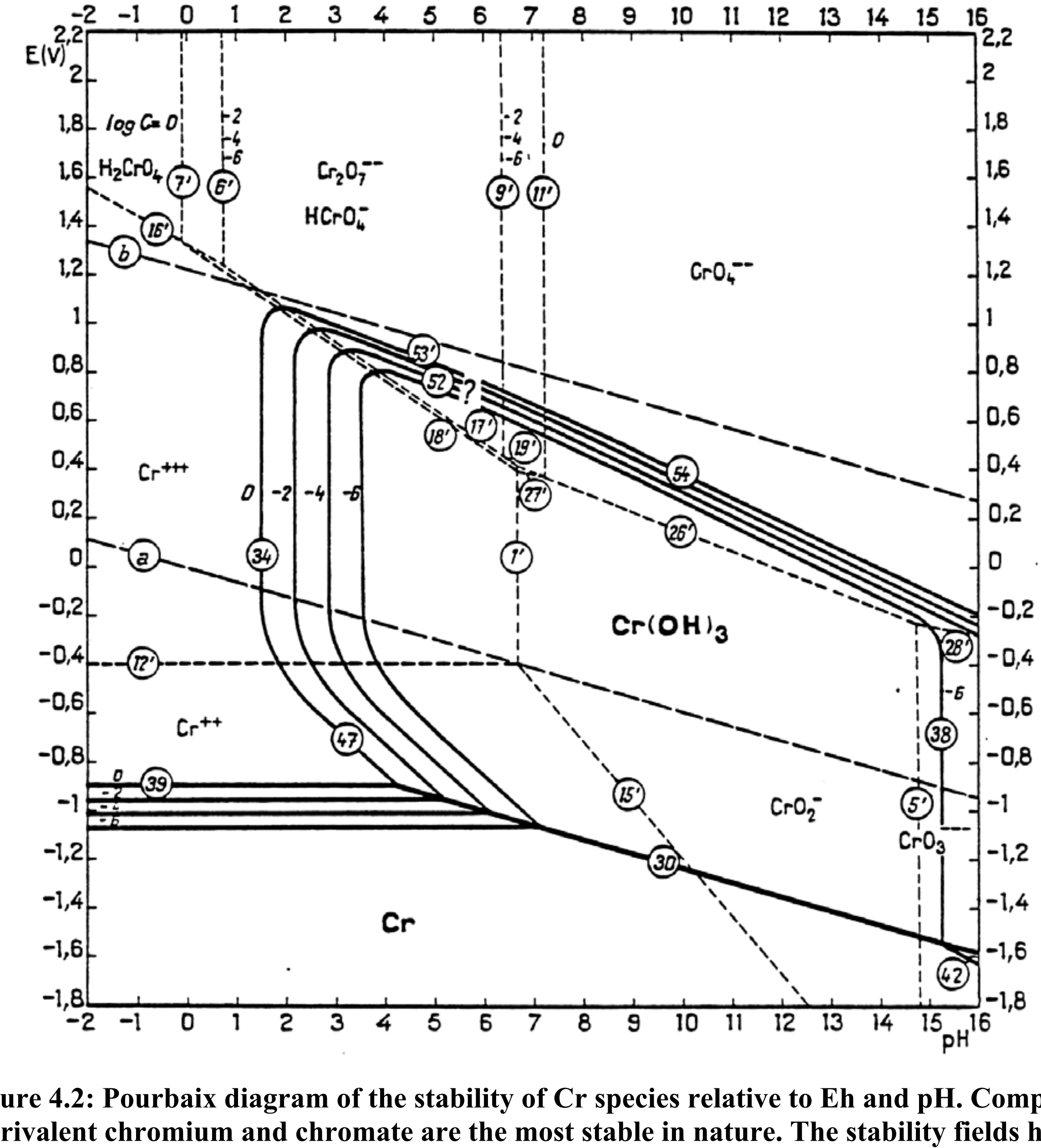

Figure 4.2: Pourbaix diagram of the stability of Cr species relative to Eh and pH. Compounds of trivalent chromium and chromate are the most stable in nature. The stability fields have been drawn for Cr concentrations 1, 10^{-2}, 10^{-4} and 10^{-6} as well as for water (lines a and b). $Cr(OH)_3$ was chosen to represent a sparingly soluble Cr^{3+} solid. $Cr(OH)_3 \cdot nH_2O$ and Cr_2O_3 have very similar stability fields (from Pourbaix, 1966). The equations are collected in Appendix C.

Table 4.1: Solubility of various Cr compounds in water. Some Cr(VI) compounds have a very high solubility but the Cr(III) compounds are insoluble (after Hoffmann et al., 2002).

Formula	Cr	$Cr(OH)_3$	Cr_2O_3	CrO_3	$PbCrO_4$	$BaCrO_4$	$Na_2Cr_2O_7$
Valence	0	3	3	6	6	6	6
Solubility in water (g/L)	Insoluble	Insoluble	Insoluble	625 (20°C)	$5.8 \cdot 10^{-5}$ (25°C)	$4.4 \cdot 10^{-3}$ (28°C)	1,800 (20°C)

develops on the surface of the steel as chromium combines with oxygen in the air. The chromium oxide acts as a passive layer and inhibits oxidation of the iron. If scratched, the layer quickly rejuvenates itself, provided enough oxygen is present. The outermost layers of the steel consequently become depleted in chromium and to restore equilibrium, chromium diffuses from the bulk to the surface by solid-state diffusion along grain boundaries and fractures. The production of an oxide protective layer works well under ambient conditions but it does not work when, for example, steel is placed in suboxic zones of the oceans (Helmenstin, 2004). In such an environment, a protective layer cannot form, so the iron in the steel oxidises, and GR has been observed as one of the oxidation products (Refait et al., 2003).

A lesser, but environmentally very important part of the world's chromium production, is used in smaller industries. The compounds are often soluble and therefore prone to end up in the natural environment. With its range of colors, chromium compounds are not surprisingly used as pigments. Orange pigment produced from chromium was formerly, so products containing this pigment are still a risk to the environment (Lipscher, 2004b). Chrome yellow continues in common use for products ranging from paints to plastics. It has the chemical formula $PbCrO_4$, identical to crocoite, but synthetic powder can be manufactured by mixing solutions of $Pb(NO_3)_2$ with K_2CrO_4 (Lipscher, 2004a). Cr_2O_3 makes a green pigment often used in paper, glassware and cosmetics (Sino-partner.com, 2004). Chromium in its metallic form is used as a coating, producing a shiny steel-grey surface on metal and plastic products. Chromium is also used in more than 80% of leather tanning processes (Miljøstyrelsen, 2002). Usually basic chromium(III)sulphate is brought to react with collagen fibers in the prepared hide. This protects the material from degradation and produces a cross-linking of the fibers, adding strength and flexibility (McLean, 1997). The non-toxic Cr(III) used may however oxidise to toxic Cr(VI), if the right procedure is not used. A test performed by the Danish Environmental Protection Agency (Miljøstyrelsen) has detected Cr(VI) in many leather products including watch bands, shirts, hats, shoes and baby shoes (Miljøstyrelsen, 2002).

As it preserves animal skin, chromium also preserves wood. Cr(VI) compounds have been used in wood preservatives for many decades, but this use is now declining because of the toxicity of Cr(VI) and its risk to the environment. In Denmark, for example, it has been illegal to use chrome preservatives since 1997, but there is still no law against importing chrome preserved wood from other countries (Miljøstyrelsen, 2000). Chromium may also be released as a side effect of other activities that do not have focus on this particular element. An example is the burning of fossil fuel and the leaching by rainwater through fly ash generated in fossil fuel and municipal waste incineration. Chromium finds its way to the natural environment as dust and as soluble compounds that are released during mining and processing unless a great deal of care is taken and some chromium is always given off during use of Cr-treated products.

4.1.3 Release of Chromium to the Environment

How much chromium is released on a world basis is difficult to determine, but estimates have been made for individual countries. Out of approximately 25,000 to 30,000 t consumed in Denmark, the current annual release is estimated to be in the range of 23 to 57 t. Table 4.3 and Table 4.3 give details of the estimated consumption and emission to air, water, soil and landfill (Hoffmann et al., 2002). For society, however, a more vital issue than the total amount of chromium released, is the concentration of the compounds available in the surroundings. Too high levels of chromium may cause serious illness; thus most countries operate with limits for drinking water and soils. The guideline for total chromium in drinking water given by the World Health Organization (WHO) is 0.05 mg/L. Although hexavalent chromium is much more toxic than Cr in its other valence states, WHO provides no specific limit value, because Cr(VI), as a separate species, apparently is too difficult to measure (WHO, 2004). However, essentially all Cr present in aqueous form is Cr(VI) because of the low solubility of Cr(III) compounds. The danger of Cr-rich dust has provoked setting of limits in soil in Canada (Table 4.4), with Cr(VI) limits between 0.4 and 1.4 mg/kg. Farmer et al. (1999) describe a particularly dangerous example of soil contamination by Cr(VI). In an area in Scotland with landfills of residuals from chromite ore processing from 1830 – 1968, the soils were contaminated with Cr(VI) at levels up to several g/kg!

Table 4.2: Consumption of chromium. Chromium compounds and chromium as a trace constituent in Denmark in 1999 (average of the years 1998, 1999 and 2000) divided among fields of application (modified from Hoffmann et al., 2002).

Field of Application	Consumption (t/year)	%	Of this Cr(VI) (t/year)
Chromium, metallic			
- Iron and steel	24,300-29,300	97	-
- Aluminum alloys	11-106	0.2	-
- Copper alloys	6-9	0.03	-
Chromium compounds			
- Tanning	164-302	0.8	0.016-0.035
- Surface treatment	37.7	0.14	37.7
- Hardeners	13-47	0.11	<<1
- Pigments in paint and plastic	12.6-116.7	0.23	1-2
- Impregnation	8.8	0.03	8.8
- Laboratory chemicals	<1	0	<1
- Other applications (drill mud, firebricks, ovenproof products, etc.)	208-522	0.77	-
Chromium as a trace constituent			
- Coal and oil	147	0.53	-
- Cement	67	0.24	2.1-4.2
- Municipal incinerator fly ash	62-183		
In total	25,026-30,537	100	49.6-52.7

4.1.4 Redox Cycle of Chromium

The only known oxidisers of Cr(III) in natural environments are manganese oxides. In a field test of 45 arable soils, Chung and Sa (2001) found that the oxidation potential of chromium was directly related to manganese content. Oxygen by itself could not easily transform Cr(III) to Cr(VI). The same investigation also showed that the reduction potential for chromium was proportional to the content of organic matter as well as soil pH. Cr(VI) reacts with organic matter and is reduced, ultimately to Cr(III). In well-oxygenated zones, microbial activity is also responsible for the reduction of Cr(VI), but under reducing conditions, abiotic reduction is the main pathway. Mainly

Table 4.3: An approximation of the amount of chromium that ended up in the environment in Denmark in 1999. Numbers are in t/year (Modified from Hoffmann et al., 2002)

Process/Source	Air	Water	Soil	Landfill	In total
Industrial processes					
- Processing, use and disposal of iron and steel	?	?	15.5-31	-	15.5-31
- Reuse of iron and steel	0.1-0.2	0.017-0.034	-	2.3	2.4-2.5
- Processing, use and disposal of aluminum	0-0.1	0.2-2	0.1-1	3-37	3.3-40
- Processing, use and disposal of copper	~0	-	0.1-0.2	1-2	1.1-2.2
- Conversion of energy (coal and oil)	3.5	-	-	?	3.5
- Other industrial processes	-	0.2	-	-	0.2
- Surface treatment	-	0.089	-	-	-
- Impregnation	-	?	-	-	?
- Tanning	-	0.27	-	-	0.27
- Transport	0.2	-	-	-	0.2
Use of products					
- Impregnated wood	-	0.3-0.6	0.3-0.6	-	0.6-1.2
- Chromium-plated products	-	-	??	-	??
- Paint	-	0.03-13	-	-	0.03-13
- Laboratory chemicals	-	<<1	-	-	<<1
Waste treatment					
- Waste incineration	0.3-1.5	-	-	36-96	36-98
- Biological waste treatment	-	-	0.086	-	0.086
- Deposit of solid waste	-	-	-	??	??
- Kommunekemi*	?	-	-	104-107	104-107
- Municipal waste water	-	1.2	-	-	1.2
- Residual sludge	-	-	2.1	1.4	3.5
In total	4.1-5.5	2.3-17	16-33	148-244	170-302

*** Kommunekemi is a Danish company that processes toxic waste. The waste undergoes incineration and what cannot be recycled is landfilled**

sulfur and iron in their reduced states act as electron donors with sulfur species dominating at low pH and iron species at neutral to high pH (Fendorf et al., 2000). In synthetic environments, iron, both in its metallic form and as structurally bound Fe(II), is a fast reducer of Cr(VI). Reduction by elemental iron and iron-bearing minerals has therefore been studied widely and recently, the Fe(II)-Fe(III) hydroxide green rust has caught attention as a very active compound in Cr(VI) reduction. It is easily synthesised in the laboratory and because Fe(II) and Fe(III) are common components in

Table 4.4: Maximum acceptable concentrations in Canada of chromium for various environments (after CEQG, 2002)

Parameter	Water: Aquatic life		Water: Agricultural		Soil			
	Freshwater μg/L	Marine μg/L	Irrigation μg/L	Livestock μg/L	Agri.[a] mg/kg	Res./Park[b] mg/kg	Comm.[c] mg/kg	Industrial[d] mg/kg
Chromium					64	64	87	87
Trivalent	8.9	56	4.9	50				
Hexavalent	1.0	1.5	8	50	0.4	0.4	1.4	1.4

[a]Agri.: Agricultural land uses, [b]Res./Park: Residential/Parkland uses, [c]Comm.: Commercial land uses, [d]Industrial: Industrial land uses.

soils and groundwater, it is likely that GR is common in these settings. A better understanding of the interaction between Cr(VI) and GR may thus be valuable in future remediation projects.

4.2 GREEN RUST

Green rust (GR) is a mixed-valent iron hydroxide with a beautiful dark bluish-green color. The earliest description in the accessible literature is by Ostwald in 1900 (as cited by Hansen, 2001). The term, green rust, refers to a family of compounds, where layers of Fe(II)-Fe(III) hydroxide alternate with interlayers of anions and water. The layered structure was demonstrated in the middle of the last century by Feitknecht and Keller (1950) and in 1959, Bernal et al. were able to classify separate GR types based on stacking sequences. Recent investigations in our group (Christiansen et al., in progress) suggest that a monovalent cation is a necessary element of the structure. Synthesising green rust in the laboratory is very easy, but confirmation of its presence in natural environments has been very difficult. Stampfl (1969) reported GR as a corrosion product in a water pipe. Koch & Mørup (1991) described green rust from an ochre sludge and Trolard et al. (1997) reported its presence in a hydromorphic soil. The scarcity of reports of natural GR almost certainly results from difficulty in sampling. GR is highly reactive in oxidising conditions. When exposed to air, the compound transforms to commonly known red rust within seconds to minutes. This behaviour, which is not common to other known Fe(II)-bearing minerals, such as magnetite, biotite or siderite, may be explained by the structure of GR.

4.2.1 Green Rust Structure

All GR types are layered double hydroxides (LDHs). This structure consists of brucite-like sheets of metal hydroxide (Figure 4.3) alternating with interlayers of anions and water. Brucite has the formula $Mg(OH)_2$, but in LDHs, some of the divalent metal ions are substituted for trivalent. In the case of GR, iron occupies both positions as Fe(II) and Fe(III). The incorporation of trivalent iron produces a surplus of positive charge in GR according to the formula: $Fe(II)_{(1-x)}Fe(III)_x(OH)_2^{x+}$. To restore neutrality, GRs are known to incorporate anions in the interlayers along with water molecules. The number of water molecules per formula unit is uncertain and ranges from two to eight depending on the GR type. In this thesis, the newest or most commonly used structure and composition results will be used. The steric nature of the incorporated anion affects the stacking of the hydroxide layers and results in different types of GR. Based on X-ray diffraction (XRD), which is a technique that identifies the structure of solid compounds, two main types, GR1 and GR2, are recognised (Figure 4.4). Anions responsible for a GR1 structure are two-dimensional ions, e.g. planar or spherical, and anions causing a GR2 structure are three-dimensional, typically tetrahedral (Bernal et al., 1959). The two-dimensional ions, which have been reported in the literature as interlayer anions in GRs, are Cl^-, Br^-, I^-, F^-, CO_3^{2-}, NO_3^-, $C_2O_4^{2-}$, SO_3^{2-} and perhaps OH^-. The three-dimensional anions comprise SO_4^{2-}, SeO_4^{2-}, ClO_4^-, $H_xPO_4^{(3-x)-}$ and probably the amino acid cysteine ($C_3H_7NO_2S$). References are listed in Table 4.5 and Table 4.6. GR1 has a smaller *d*-spacing in the basal layers than does GR2. A two-dimensional ion, such as CO_3^{2-}, typically gives a layer thickness of about 8 Å whereas a three-dimensional ion, such as SO_4^{2-}, produces a layer thickness of about 11 Å.

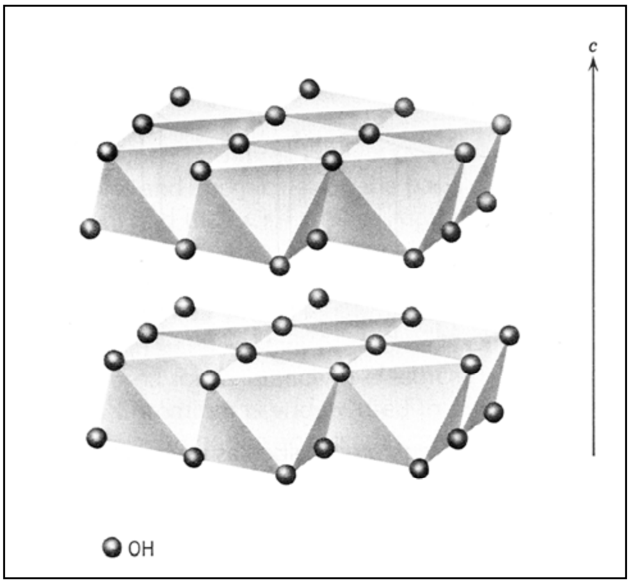

Figure 4.3: Brucite layers ($Mg(OH)_2$) resembling the layers of $Fe(OH)_2$ in GR. Here, Mg^{2+} is in the center of each octahedral. In GR, Fe(II) or Fe(III) are in the centres (from Klein & Hurlbut, 1993).

Although the anion incorporated is chiefly decided by accessibility, species competition plays a role. Most research has been done on GR sulphate (GR_{SO4}), carbonate (GR_{CO3}) and chloride (GR_{Cl}). Refait et al. (1997) established the following stability succession based on competition experiments: $CO_3^{2-} > SO_4^{2-} > Cl^-$.

The ion-exchange equilibrium constants for other LDHs, the hydrotalcite-like compounds, were established by Miyata (1983) and also gave $CO_3^{2-} > SO_4^{2-}$ indicating that this succession is general for LDH compounds. Although one GR may be said to be more "stable" than another, even the most stable are only metastable under ambient oxic conditions. The oxidation of GR, which is very fast, is fatal to the structure. Furthermore, pH below about 6 or very high pH as well as solutions With low concentrations of Fe^{2+} and/or anions has been reported to cause breakdown (Vins et al., 1987; Lewis 1997 and Larsen, Christiansen, Skovbjerg, work in progress in our laboratory). The

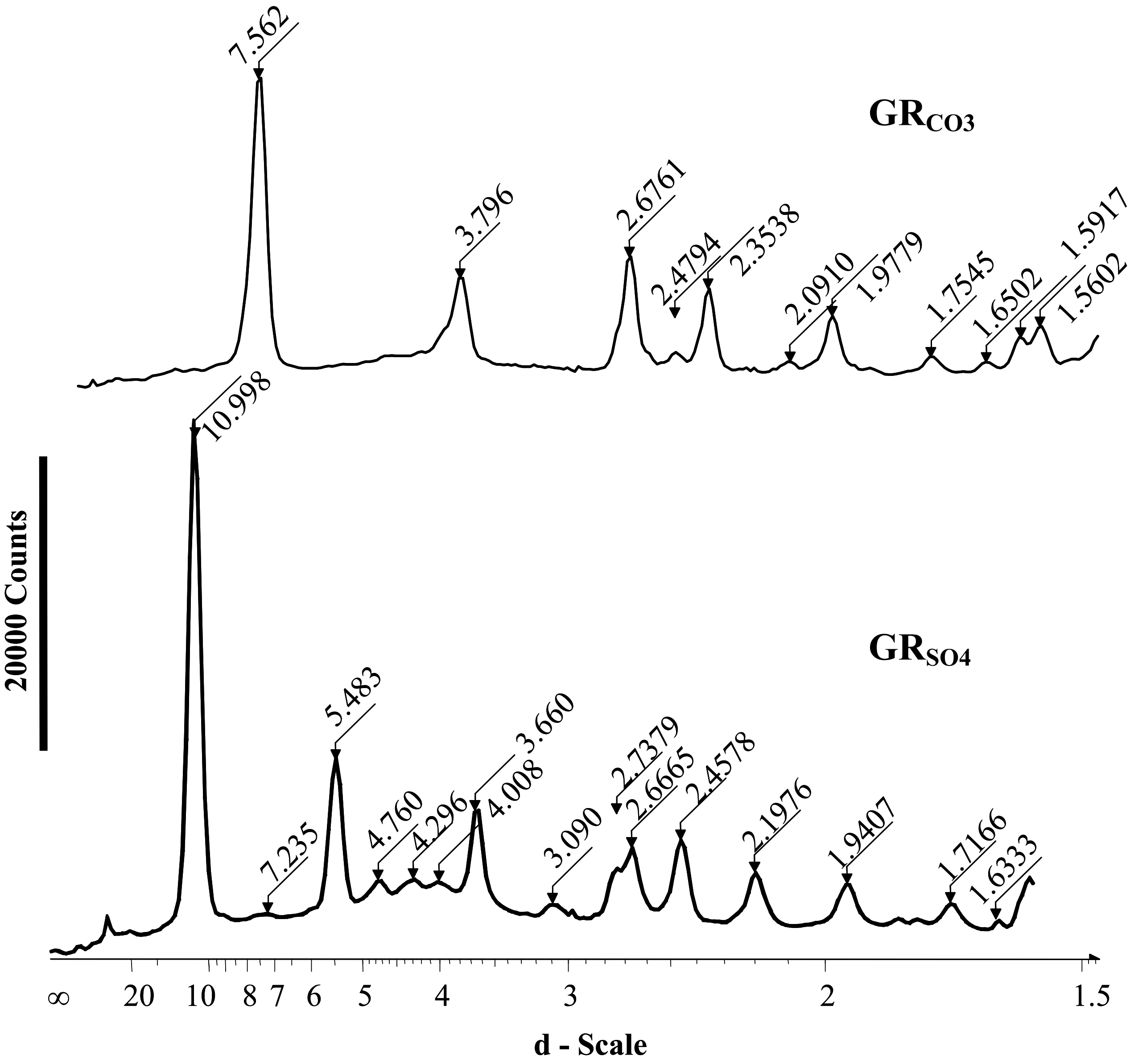

Figure 4.4: XRD traces of GR_{CO3} above and GR_{SO4} below. GR_{CO3} belongs to the GR1 type structures. It has a significantly smaller d-spacing than GR2 type structures to which GR_{SO4} belongs. The XRD trace of GR_{CO3} is modified from Larsen (2003).

Table 4.5: Various green rust forms that are stable in the absence of oxygen, as described in the literature. The stoichiometries are reported with various values in the literature. The Fe(II):Fe(III) ratio vary with sampling time, synthesis method and analysis method, as does the spacing of the hydroxide layers. The amount of water is also not very certain. The values in the formulae reported in this table are the, so far known, ideal values. Hydroxide GR (GR_{OH}) has not been included in this table because of unconvincing evidence of existence.

Anion	Type	Fe(II): Fe(III)[a]	Spacing[b] (Å)	Formula	Selected references
Cl^-	GR1	3	8.0(1) 7.93(2)	$Fe(II)_3Fe(III)(OH)_8Cl \cdot nH_2O$(3)	Bernal et al. (1959)(1); Vins et al. (1987)(2); Refait & Génin (1993)(3)
Br^-	GR1	3	7.64(4) 7.97(5) 8.06(6)	$Fe(II)_3Fe(III)(OH)_8Br \cdot nH_2O$[c]	Bernal et al. (1959)(4); Vins et al. (1987)(5); Lewis (1997)(6)
I^-	GR1	3	8.38(7) 8.29(8)	$Fe(II)_3Fe(III)(OH)_8I \cdot nH_2O$[c]	Lewis (1997)(7); Vins et al. (1987)(8)
CO_3^{2-}	GR1	2	7.5	$Fe(II)_4Fe(III)_2(OH)_{12}CO_3 \cdot 2H_2O$	Hansen, 1989; Drissi et al., 1995; Legrand et al., 2004b;
$C_2O_4^{2-}$	GR1	3	7.9	$Fe(II)_6Fe(III)_2(OH)_{16}C_2O_4 \cdot 3H_2O$	Refait et al. (1998)
SO_4^{2-}	GR2	2	10.9(9) 11.01(10) 11.03(11)	$Fe(II)_4Fe(III)_2(OH)_{12}SO_4 \cdot 8H_2O$(10)	Bernal et al. (1959)(9); Simon et al. (2003) (10) Hansen et al. (1994) (11)

a) Fe(II):Fe(III) ratio in the hydroxide layer
b) Distance from the bottom of one hydroxide layer to the bottom of the next.
c) Not reported, but likely formulae because of similarity with Cl^-

stability of GR also changes when the interlayer anion is changed. If the anion incorporated is reducible, then Fe(II) acts as electron donor, eventually causing a breakdown of the structure. For example, when nitrate is incorporated in the interlayers, it is reduced to ammonium while the GR

Table 4.6: Various green rusts that are metastable or unstable because the interlayer anion can oxidise the Fe(II) in the hydroxide layers.

Anion	Type	Selected References
NO_3^-	GR1	Hansen & Koch (1998)
SeO_4^{2-}	GR2	Refait et al. (2000)
SO_3^{2-}	GR1	Simon et al. (1997)
ClO_4^-	GR2	Lewis (1997)
$H_xPO_4^{(3-x)-}$	Sorbed in interlayers of GR_{SO4}	Hansen & Poulsen (1999)

transforms to magnetite (Hansen, 1998). Phosphate, as another example, may also be incorporated, but eventually GR becomes unstable and vivianite is formed (Hansen & Poulsen, 1999). Substitution of other cations for Fe(II) and Fe(III) is possible. The presence of Al, Mg, Co, Ni, Cu, Zn, Ca, Ga, Cr and Ln has been reported in other LDHs and Roy et al. (2001) and Tamura et al. (1985) showed that some of them are readily incorporated in GR.

Simon et al. (2003) recently evaluated the GR_{SO4} structure and suggested trigonal symmetry with the cell parameters: a = 0.5524 nm and c = 1.1011 nm. This structure was based on results from capillary tube X-ray diffraction (CT-XRD), but several peaks were omitted. Christiansen et al. (in progress) included these peaks in a Rietveld analysis and suggested they are caused by the incorporation of cations in the interlayers. By using various metal hydroxides (M^+OH^-) in the synthesis, they were able to prove incorporation of the monovalent cation (M^+). Depending on the size of the cation, peaks appeared or disappeared on CT-XRD traces and these results are now being used to improve the structural description of GR_{SO4}. The results reached at the point of printing this thesis appoints GR_{SO4} to space group P3m1, with cell parameters a = 9.53 Å and c = 21.98 Å. However, these results are still being refined so they are not used further in this thesis. The planned publication based on this thesis will incorporate the newest, hopefully final, information.

4.2.2 Synthesis of Green Rust

As well as being dependent on available ions, the structure and habit of GRs may also be influenced by the synthesis method. The GR compounds can be synthesised in various ways. It requires a solution of Fe^{2+}, Fe^{3+}, OH^- and a suitable anion. Provided pH is near neutral to slightly basic and the temperatures are moderate (room temperature), green rust forms. However, other iron phases, such as magnetite (Fe_3O_4), lepidocrocite (γ-FeOOH) or goethite (α-FeOOH) may also form. To ensure a chemically and structurally pure and reproducible green rust phase, specific synthesis methods have been developed. There are several. i) $Fe(OH)_2$ is prepared and oxidised in the presence of dissolved anions. pH is allowed to equilibrate and may be monitored together with Eh as an indication of when the material is predominantly GR (Bernal et al., 1959; Feitknecht and Keller, 1950). Figure 4.5 shows the evolution of pH and Eh through a full oxidation. ii) A Fe^{2+} solution is oxidised in the presence of dissolved anions. pH is kept static through titration with a base, often NaOH or Na_2CO_3 (Taylor et al., 1985; Schwertmann and Fechter, 1994; Koch and Hansen, 1997). Figure 4.6 shows the consumption of NaOH during a full oxidation of a $FeSO_4$ solution. These two are the most commonly used. Other GR synthesis methods are: iii) mixing Fe^{2+} and Fe^{3+} salts and neutralising with base (Hansen et al., 1994); iv) abiotic reductive dissolution of Fe(III)-hydroxide with Fe^{2+}

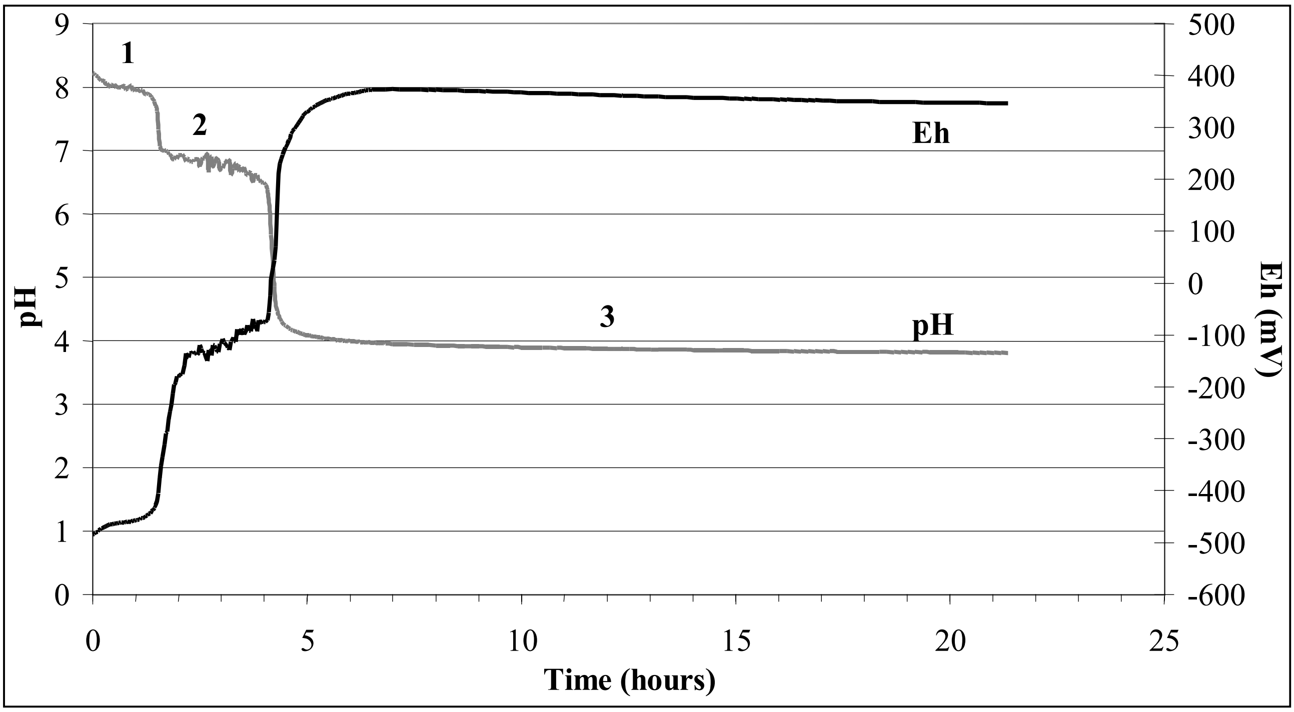

Figure 4.5: Eh and pH evolution of a $FeSO_4$ solution with NaOH during air oxidation. There are three plateaus representing each equilibrium: 1) $FeOH_2$ and GR_{SO4} are co-existing, 2) GR_{SO4} and α-FeOOH are co-existing, 3) α-FeOOH is the end product (from Christiansen, 2004).

(Tamura et al., 1984); v) bacterial reductive dissolution of Fe(III)-hydroxides (One-Nguema et al., 2002); vi) partial oxidation of $FeCO_3$ (Taylor, 1980); and vii) oxidation of native iron in the presence of anions (McGill et al., 1976). There has been no systematic investigation of the differences in crystal structure and chemical behaviour related to the synthesis method.

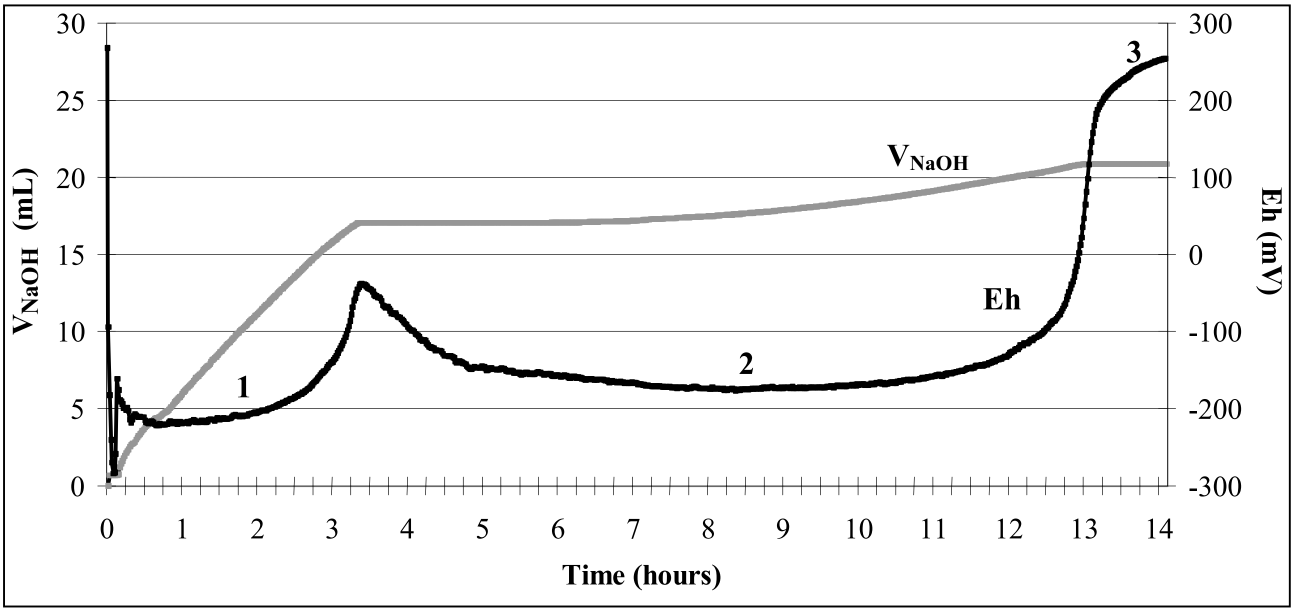

Figure 4.6: NaOH addition and Eh evolution at pH 7, maintained with a pH-stat during synthesis of GR and continued oxidation to a ferric end product. At plateau 1, a pure Fe(II) species, probably $Fe(OH)_2$, and GR_{SO4} co-exist. At plateau 2, GR_{SO4} and α-FeOOH co-exist. After 14 hours, one can see the beginning of plateau 3, where only α-FeOOH is stable.

4.2.3 Reactivity of Green Rust Compared to Other Fe(II)-Bearing Compounds

In redox reactions between a mineral and other phases, reduction potential and structure are important parameters. Several natural minerals have Fe(II) in the structure. Magnetite, pyrite, biotite, vermiculite and montmorillonite are some examples and Lee and Batchelor (2003) have compared the reductive capacities of GR_{SO4} and these five minerals for Cr(VI) and tetrachloroethylene (PCE). GR_{SO4} and magnetite were shown to have by far the greatest reduction capacities, defined as "…the amount of an oxidant that can be reduced when sufficient time is given so that the reaction proceeds to its maximum extent" (Lee and Batchelor, 2003). The authors showed that the reduction capacity was proportional to the Fe(II) content of the compound. However, reaction rates are also very important when assessing the probability that an Fe(II) containing compound will react with redox sensitive elements floating by.

A theoretical approach to evaluate the relative kinetics can be made. Because the amount of ferrous iron is crucial when determining the reduction potential, one can compare the relative composition of GR and magnetite, which is also rich in Fe(II), will be made. In GR_{SO4}, the Fe(II) to Fe(III) ratio is 2:1 whereas it is 1:2 in magnetite ($Fe(II)Fe(III)_2O_4$). For every 6 Fe atoms present, 4 Fe(II) are available for oxidation if they are bound in GR_{SO4} while only 2 Fe(II) are available for oxidation in magnetite, so quantitatively, GR_{SO4} is twice as effective. The bonding environment of Fe(II) also plays a role for the rate of reaction. The ferrous iron in magnetite is bound to O with strong ionic bonds, while the OH^- in the GR layers shares weaker ionic bonds with Fe(II) (Klein and Hurlbut, 1999). The bonds are weaker because the hydrogen shares an electron with O thereby weakening the link between Fe(II) and O. This makes the iron easier to oxidise.

Various other structural considerations advocate for GR being kinetically superior to magnetite as well. Magnetite, with its cubic mineral structure produces ball-like crystals with close to minimum surface area, so the amount of Fe(II) available for oxidation at the surface is relatively small. Because the magnetite crystal is isotropic, it has a similar appearance in all directions so no area is preferentially attacked by the oxidant. This means that the magnetite crystals probably remain stable for relatively extended periods and available Fe(II) on the surface is quickly used up. In contrast, GR produces platy crystals with a large surface area, so a lot of Fe(II) is available, from the beginning of a redox reaction. Furthermore, when the surface of a GR crystal is attacked, the conversion of Fe(II) to Fe(III) results in charge imbalance, which must be offset by adsorption of additional anions or the loss of H^+. Together with the loose bonding between the layers this helps to break down the structure and new layers of Fe(II) are quickly exposed. There is also the possibility that the reducible compound comes into contact with Fe(II) via the interlayers. Drits and Bookin (2001) reviewed the structure of various types of LDHs. They showed that a Na and SO_4-bearing LDH, comparable to GR_{SO4}, with a layer thickness of 11 Å, has an interlayer thickness of approximately 9 Å. Provided the interlayer molecules are easy to kick out, even relatively large compounds could get access via the interlayer to Fe(II). Considering both surface and simultaneous interlayer reduction, the reaction should be very fast. Green rust is in fact very active in redox reactions, as several studies in the literature have shown. The following section presents an overview of these.

4.2.4 Green Rust Reduction of Various Compounds and Elements

4.2.4.1 Nitrate and Nitrite

Some of the first compounds to be examined in reaction with GR were oxidised nitrogen compounds (Hansen et al., 1994; 1996). Nitrate and nitrite are important terrestrial fertilizers, but theyare very mobile in aquatic environments and may lead to serious eutrophication when leached. This problem is overcome when they are “denitrified”, meaning reduced, either by minerals in the soil or by bacteria. Hansen et al. (1994) showed that nitrite (NO_2^-) is reduced to ammonium (NH_4^+) when in contact with GR_{SO4}. The same is true for nitrate (NO_3^-), though this reaction is slower (Hansen et al., 1996). In the given experiment, nitrate was added as a sodium salt and reduction was interpreted to only take place at the mineral surface. By adding the nitrate ions as $Ba(NO_3)_2$ instead, sulfate was forced out of the interlayers to form insoluble barite ($BaSO_4$), thereby enhancing the ability of NO_3 to attack in the interlayer. The forced exchange into the interlayer caused the rate of reaction to increase by 40 times (Hansen & Koch, 1998). The rate of reaction between GR_{CO3} and nitrate were similar to those obtained with GR_{SO4} and in all the cases examined, magnetite was the end product (Hansen & Koch, 1997).

4.2.4.2 Chlorinated Organic Compounds

Another range of contaminants is the chlorinated organic compounds, which are carcinogenic, even in very low concentrations. Through reduction, these compounds can be dechlorinated to harmless hydrocarbons. A selection of compounds, i.e. CCl_4 (Erbs et al., 1999), tetrachloroethylene (PCE), trichloroethylene (TCE), *cis*-dichloroethylene (c-DCE) and vinyl chloride (VC) (Lee and Batchelor, 2003), were reductively dechlorinated by GR_{SO4}. In their comparison experiment, Lee and Batchelor (2003) found that GR_{SO4} had the greatest reductive capacity compared to pyrite, magnetite, biotite, vermiculite and montmorillonite, and interpreted their results to reflect the proportion of Fe(II).

4.2.4.3 Uranium

Radioactive waste, mainly from nuclear power plants, is currently deposited in what are hoped to be safe settings. Internationally, there is a great deal of effort to provide back-up strategies in the case of eventual leaks. Liners and casings are designed to contain reactive materials. Clay is one candidate; GR is another. The reduction of some radionuclides, such as uranium, can produce less mobile compounds and the risk to the environment is therefore decreased. Adding U(VI) to a suspension of GR_{SO4}, O'Loughlin et al. (2003) showed that it was readily reduced to U(IV) and that GR_{SO4} in return was partially transformed to magnetite. The U(IV) combined with oxygen to form UO_2 nanoparticles (1.7 nm +/- 0.6 nm) that associated with the remaining GR crystals. In a enclosed system, this solved the problem but the authors pointed out that the small size of the particles presents a new problem in the environment. The nanoparticles may become mobile alone or sorbed onto the colloidal GR (Kaplan et al., 1994; Kersting et al., 1999, as cited by O'Loughlin et al., 2003). However, concluding evidence for colloidal transport has been elusive (Marty et al., 1997, as cited by O'Loughlin et al., 2003). While the UO_2 nanoparticles were associated with GR in their experiments, the authors presented no experiments suggesting what phase, if any, the UO_2 particles would be associated with if GR was exhausted by the reaction. This question is important to answer in order to predict the effectiveness of GR as a barrier for uranium and other redox active actinides.

In another study on GR_{SO4} reduction of U(VI) by Dodge et al. (2002), the focus was the iron corrosion processes. Several other iron compounds were also examined, so GR was only a minor part of the study. It appears that the complexity of the GR system did not receive the attention needed and that reflects on the results presented on GR. For example, it is unclear at what point in the reaction GR existed. An XRD diagram where the caption states "GR with U", shows only magnetite and the authors also state in the text that, "synthesis of GR II in the presence of U resulted in its reduction to tetravalent form with the formation of magnetite" (Dodge et al., 2002), but there is no direct proof of the presence of GR at any point. Uranium was added as uranyl nitrate together with $FeSO_4$ and the solution was bubbled with oxygen to produce GR. This experimental set up poses a problem, because nitrate itself oxidises GR to magnetite (Hansen et al. 1996). For every mole of UO_2^{2+} added in these experiments, two moles of NO_3^- are also added. Equations 1, 2 and 3 below show the reactions.

Dissolution of uranyl nitrate hexahydrate

$$0.01\ \mathrm{M\ UO_2(NO_3)_2 \cdot 6H_2O} \Rightarrow 0.01\ \mathrm{M\ UO_2{}^{2+}} + 0.02\ \mathrm{M\ NO_3{}^{-}} + 0.06\ \mathrm{M\ H_2O} \qquad \text{Eq. 1}$$

Oxidation of GR_{SO4} by $UO_2{}^{2+}$

$$\mathrm{Fe(II)_4Fe(III)_2(OH)_{12}SO_4} + \mathrm{UO_2{}^{2+}} \Rightarrow \mathrm{2Fe_3O_4} + \mathrm{UO_{2(S)}} + \mathrm{SO_4{}^{2-}} + \mathrm{4H^+} + \mathrm{4H_2O} \qquad \text{Eq. 2}$$

(Based on O'Loughlin et al. 2003)

Oxidation of GR_{SO4} by $NO_3{}^-$

$$\mathrm{Fe(II)_4Fe(III)_2(OH)_{12}SO_4} + \tfrac{1}{4}\mathrm{NO_3{}^{-}} + \tfrac{3}{2}\mathrm{OH^-} \Leftrightarrow \mathrm{SO_4{}^{2-}} + \tfrac{1}{4}\mathrm{NH_4{}^{+}} + \mathrm{2Fe_3O_4} + 6\tfrac{1}{4}\mathrm{H_2O} \qquad \text{Eq. 3}$$

(Hansen, 2001)

According to these equations, U(VI) oxidises only twice as much GR_{SO4} as nitrate, provided the rates of reaction are comparable and GR_{SO4} in fact is the compound present. It is therefore difficult to determine what reactions are actually responsible for GR oxidation in the work by Dodge et al. (2002).

4.2.4.4 Technetium

^{99}Tc is a radioactive isotope that is produced in fission reactions. It has a half-life of up to 4.2×10^{-6} years and decays by electron capture or emission of β^--particles. In its most stable state, as $Tc(VII)O_4^-$, it is among the most mobile radionuclides, so reduction with subsequent immobilisation, because of lower solubility of the reduced species, is essential. GR_{SO4} and GR_{CO3} readily reduce Tc(VII) to largely insoluble Tc(IV), as shown by Pepper et al. (2003). Because technetium is often stored in solutions with $NaNO_3$ concentrations above 2 M, Pepper et al. (2003) performed experiments with GR suspended in both pure water and 3 M $NaNO_3$ solutions. In both cases, 99.8% of the added Tc(VII) was reduced after 1 hour. This proves that GR reduces Tc(VII) just as effectively even though nitrate is present as an alternative oxidiser. The samples were studied with X-ray absorption spectroscopy (XAS), a technique that determines element identity and provides information about bonding environments. The results indicated that Tc(IV) was present as a strongly adsorbed surface complex on GR. The remaining GR was oxidised by air and all samples transformed to poorly crystalline goethite. The Tc(IV) was not re-oxidised when exposed to oxygen and remained largely insoluble.

4.2.4.5 Selenium

Se is an important trace nutrient, but it is carcinogenic and teratogenic in high concentrations. Solubility and therefore bioavailability increases with higher oxidation state so reduction of high-valent Se is desired. The behaviour of selenium and reduction of Se(VI) to lower valence states by GR was first examined by Myneni et al. (1997). They used extended X-ray absorption fine structure spectroscopy (EXAFS), which yields several types of information including elemental identity and information about neighbouring atoms. The authors found that GR_{SO4} reduces Se(VI) to Se(IV) and Se(0) both during GR co- precipitation and when GR is already present initially. The end products were lepidocrocite and magnetite. The Se(IV) formed complexes with Fe polyhedra but the presence of an Fe-selenite ($Fe\text{-}SeO_3^{2-}$) phase was not determined. The Se(IV) was further reduced and clusters of amorphous Se(0) formed. After more than 60 hours, there were indications of Se(-II), which is the most stable valence state.

Refait et al. (2000) took a different approach by adding selenate (SeO_4^{2-}) to a suspension of $Fe(OH)_2$ which was then left in anoxic conditions. In order to examine the early stages of the transformation of selenate, they added so much that not all could be reduced by the Fe(II) in the system. The analytical techniques used to characterise the solid products were XRD, transmission Mössbauer spectroscopy (TMS), which is ideal for distinguishing Fe phases among other and X-ray Photoelectron Spectroscopy (XPS). XPS is a surface-sensitive spectroscopic method that provides information about surface composition and bonding environments. The results from the anoxic experiment showed that a part of the selenate was reduced to selenite by oxidation of ferrous to ferric iron. A GR phase then precipitated and SeO_4^{2-} was incorporated into the interlayers with the same stoichiometry as SO_4^{2-} in GR_{SO4}. After 6 days the GR was fully oxidised to a ferric phase, the identity of which was not presented. In a parallel experiment, a similar solution was simultaneously oxidised by air yielding lepidocrocite as an end product.

4.2.4.6 Arsenic

In contrast to the previously described species, As is more toxic and mobile in its lower oxidation state. Randall et al. (2001) therefore found it important to examine whether GR reduces As(V) to As(III) as it reduces other species of high oxidation states. Experiments were done in two batches, one with $Na_2HAsO_4 \cdot 7H_2O$ added before GR precipitation and one with the arsenic added to a mixture of GR_{SO4} after an hour of precipitation. In both cases, air was allowed to flow for at least 6 hours until all of the GR had oxidised to lepidocrocite, confirmed XRD. Samples were taken periodically and examined with EXAFS for changes in oxidation state and bonding environment. During the time As(V) was in contact with GR, which would have been maximum six hours, since GR simultaneously was oxidised by air, no reduction was observed. As pointed out by the authors, As(V) reduction may have been kinetically hindered. Solution samples showed low levels of dissolved As, and EXAFS indicated that As(V) was adsorbed to the surface of GR rather than being incorporated as interlayer anions. There were also strong indications that As(V) was preferentially adsorbed to GR in the partially oxidised suspensions that contained both GR and lepidocrocite.

Lin and Puls (2003) also studied the interaction between arsenic and GR (chloride and sulphate), as well as goethite and lepidocrocite, but under anaerobic conditions. They reacted 50 mg GR with 1.0 mM $NaAsO_2$ and Na_2HAsO_4 stock solutions and found that the adsorption of As(V) and As(III) was 74 and 12 mg /g GR; the oxidation of As(III) to less toxic As(V) by GR was 75%, while the reduction of As(V) to As(III) by GR was less than 5%. An experiment was performed where GR was left in a suspension at reducing conditions and pH 7, with high levels of As(III) and As(V). After three months the GR rust had oxidised As(III) and parasymplesite ($Fe(II)_3(AsO_4)_2 \cdot 8H_2O$), a compound consisting of the less toxic and less mobile As(V) species, had formed. This reaction resulted in the removal of approximately 95% of the As in solution, so the authors conclude that under reducing conditions where hydrogen sulphide is not present, GR may have great control on the mobility of As.

4.2.4.7 Silver, Gold, Copper and Mercury

The transition metals generally exhibit several possible oxidations states. The valence of silver, gold, copper and mercury determines their solubility and their biogeochemical behavior and has therefore been examined by O'Loughlin et al. (2003). EXAFS showed that Ag(I), Au(III), Cu(II) and Hg(II), added as $AgCH_3COO$, $AuCl_3$, $CuCl_2$ and $HgCl_2$, were all reduced to their zero-valent states in the presence of GR_{SO4}. Hg(0) is volatile, but silver, gold and copper were shown with TEM to form elemental, submicrometer-sized particles. This transformation resulted in the partial oxidation of GR to magnetite.

4.2.4.8 Chromium

The reduction of Cr(VI) by green rust is well-documented and has been examined with various questions in mind. The kinetics of the reaction is the most striking element; reaction rates are extremely fast (Willams & Scherer, 2001; Bond & Fendorf, 2003; Lee & Batchelor, 2003; Legrand et al. 2004a). The end product is a natural matter of concern because it governs the environmental fate of the chromium (Loyaux-Lawniczak et al., 1999; Loyaux-Lawniczak et al., 2000; Bond and Fendorf, 2003; Legrand et al., 2004a) and the mechanics of the reactions are equally important to understand, in order to predict reactions in a natural system. The results presented in the literature will be discussed together with the results from the present work. GR_{SO4} was chosen among the GR types for my research because of its ease of synthesis and because it is one of the more well examined types.

5 TECHNIQUES AND EXPERIMENTAL DETAILS

5.1 METHODS AND MATERIALS

5.1.1 Glove Box and Glove Bag

Green rust transforms to other compounds when exposed to oxygen, so anaerobic conditions were needed at all times when synthesising, storing, reacting and analysing the green rust. Much of the work was comfortably carried out in an O_2-free glove box, manufactured by Coy Laboratory Products Inc. (Figure 5.1). The glove box consists of flexible poly vinyl chloride (PVC) and has the approximate dimensions: 1 m × 1.5 m × 2 m or a volume of about 3 m^3. Hydro Norway supplies the gases which are 99.999% N_2 and a mix gas of 95% N_2 and 5% H_2. Some of the H_2 is removed through reaction with O_2, providing an inert atmosphere consisting of approximately 98% N_2 and 2% H_2 and with an oxygen concentration averaging less than about 0.5 ppm during standard running conditions Two fans are placed inside the glove box. Each of these is equipped with a layer

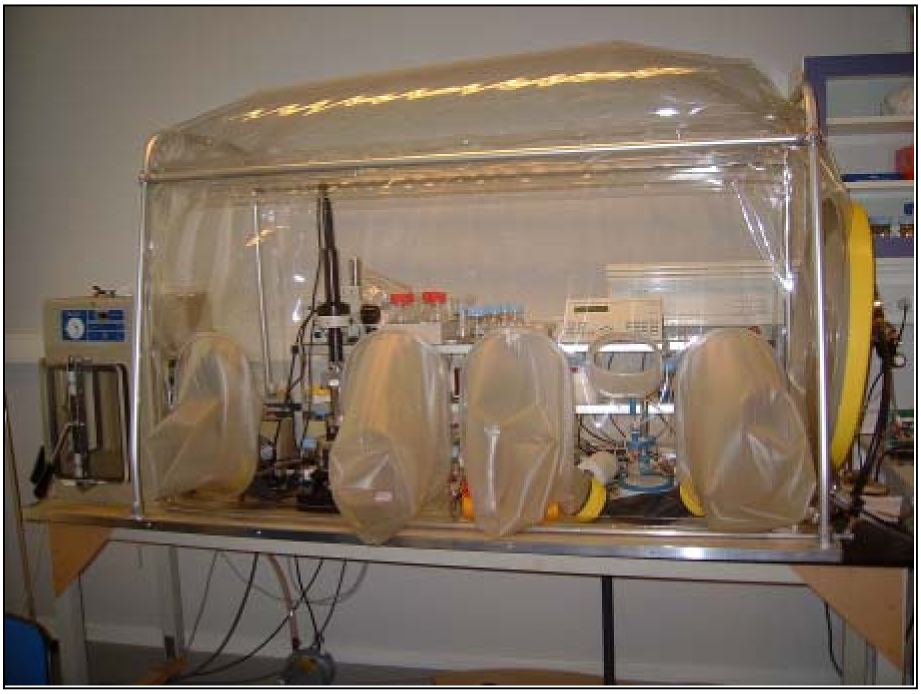

Figure 5.1: The glove box. A fast entry chamber is attached on the left side. Inside, at the left, is the atomic force microscope (AFM). At the right is the synthesis and sample preparation area with pH-stat, pH and Eh electrodes and equipment for preparing X-ray diffraction (XRD) samples.

of palladium-coated aluminium pellets that acts as "getters" for the oxygen. The palladium serves as a catalyst for the reaction between oxygen and hydrogen to form water. A second layer, consisting of porous aluminium oxide, absorbs the water from the air, thereby keeping the humidity at low levels. A fast entry chamber attached to the glove box makes it possible to move things in and out without adding large volumes of ambient air with oxygen, thus destroying the anaerobic condition. CO_2, which may cause formation of GR_{CO3} was removed by pellets of solid NaOH placed inside the box and open to the atmosphere. CO_2 partial pressure is below detection and no GR_{CO3} has been detected in any of the samples.

The TEM investigations were performed in a laboratory that did not have an anaerobic glove box, so a glove bag was used instead. It was manufactured by Instruments for Research and Industry®, had a volume of 0.6 m^3 and consisted of polyethylene. To ensure low-oxygen conditions, a vacuum pump sucked most of the air out before 99.999% N_2 was pumped back in. After inserting the equipment into the glove bag, the air-purging procedure was repeated at least three times and the equipment was left to equilibrate with the N_2-atmosphere overnight. The air was again replaced with N_2 before the GR bottles were opened. Despite taking this much care, the effect of a low partial pressure of oxygen was observed as a very slow change of colour of some spilled GR. A change that was just visible took more than half an hour, compared to seconds or minutes needed in air, so oxidation was assumed to have negligible affect on the sample preparation for TEM, which took about half an hour. The GR stock solutions were kept in sealed, blue cap flasks, which have been proven to prevent gas exchange for more than five years.

5.1.2 Synthesis of Green Rust

Green rust sulphate was prepared according to the constant pH-method described by Koch & Hansen (1997). The method was modified slightly to fit the conditions in our laboratory. $FeSO_4$ was added as melanterite ($FeSO_4 \cdot 7H_2O$), instead of a solution made from metallic iron and H_2SO_4. Nitrogen gas was used instead of argon gas and the actual synthesis was carried out in a glove box. The $FeSO_4 \cdot 7H_2O$ used for GR synthesis was supplied by AppliChem® and had a purity of minimum 99.5%. The water used in solutions and for cleaning was deionised on a MilliQ® resin column to a resistivity of 0.1 μS/cm. Glassware used for storage and reaction vessels was treated with 20% HCl to remove iron oxides from previous experiments. The Cl^- ions that probably adsorbed to the glass following this treatment, were removed by soaking with 1% HNO_3 to circumvent the formation of GR_{Cl} and the vessels were then rinsed three times with deionised water.

To avoid uncontrolled oxidation of Fe^{2+} during synthesis of GR, the water was deoxygenated prior to use by N_2 bubbling in a pyrex bottle containing 200 mL water and closed with a ceramic lid fitted with a silicone septum. The silicone behaves somewhat like a thick liquid, so that a small hole is sealed immediately again when the object in the hole is removed. A syringe needle was used to penetrate the lid and a soft plastic tube of diameter 1.9 mm was inserted. 99.999% N_2 gas was led through the tube and bubbled through the water for at least 1.5 hrs. A small syringe was used as gas-outlet and mixing was achieved with a magnetic Teflon-coated stirrer. When the tube and syringe were removed, the holes in the silicone septum closed again and the flask was immediately placed in the glove box.

The NaOH solution for the pH-stat was a standard titration solution, supplied by Merck® and diluted with N_2-bubbled demineralised water to a concentration of 1 M. The NaOH solutions were stored in plastic, not glass bottles, because silica glass corrodes in contact with strong base and silica affects the behaviour of green rust (Hendriksen & Hansen, 2004). Immediately before initiating the GR synthesis, the glass burette containing the NaOH was flushed to minimise the amount of dissolved silica.

GR_{SO4} was synthesised in the glove box using the experimental setup schematised in Figure 5.2. A solution of $FeSO_4$ was oxidised under controlled conditions to ensure the presence of both Fe^{2+} and Fe^{3+}. In order to simulate natural conditions, ambient air was bubbled through the solution. To avoid formation of GR_{CO3}, CO_2 was removed by leading the air through a 20% solution of NaOH solution. The air was then led inside the glove box, into the reaction vessel through a thin plastic tube. The reaction vessel contained 200 mL water in which 2.78 g melanterite ($FeSO_4{\cdot}7H_2O$) was dissolved. The actual synthesis of GR_{SO4} was accomplished by bubbling the CO_2-free air through the $FeSO_4$ solution, while adding 1M NaOH, usually 16 mL, with a pH-stat. The pH-stat, provided by Radiometer®, maintained pH close to 7 (± 0.1 pH unit). A peristaltic pump controlled the rate of incoming air. The air was usually pumped through the solution at such speed that the base addition rate remained below 0.09 mL/min and preferably about 0.04 mL/min. Oxidising with this rate produces crystals of a good quality (pers. comm., Hansen, 2002). It was not always possible to obtain the desired addition rate because of adjustment difficulties of the pH-stat. During synthesis the suspension was mixed with a magnetic stirrer. Temperature, Eh and pH were continuously monitored using the data-logging software HyperTerminal 6.3.

Radiometer® supplied the Eh electrode (3 M KCl, silver: silver chloride). The Eh electrode measures in volts (V) the electromotive force (emf) of the solution. The h in Eh indicates that the potential is related to the standard hydrogen electrode (SHE) and in this study, the emf values were converted to Eh values using a table by Nordstrom and Wilde (1998) that incorporated temperature effects. The electrode was regularly tested for integrity by measuring a standard ZoBell solution of known Eh. The error was in all cases less than 5 mV, which is acceptable. The thermometer was supplied by Radiometer®. Uncertainty in temperature measurements did not influence the conversion of the measured emf to Eh, because the same conversion factor was used over temperature ranges of 5° C, e.g. from 20-25°C, causing the effect of temperature uncertainty to be

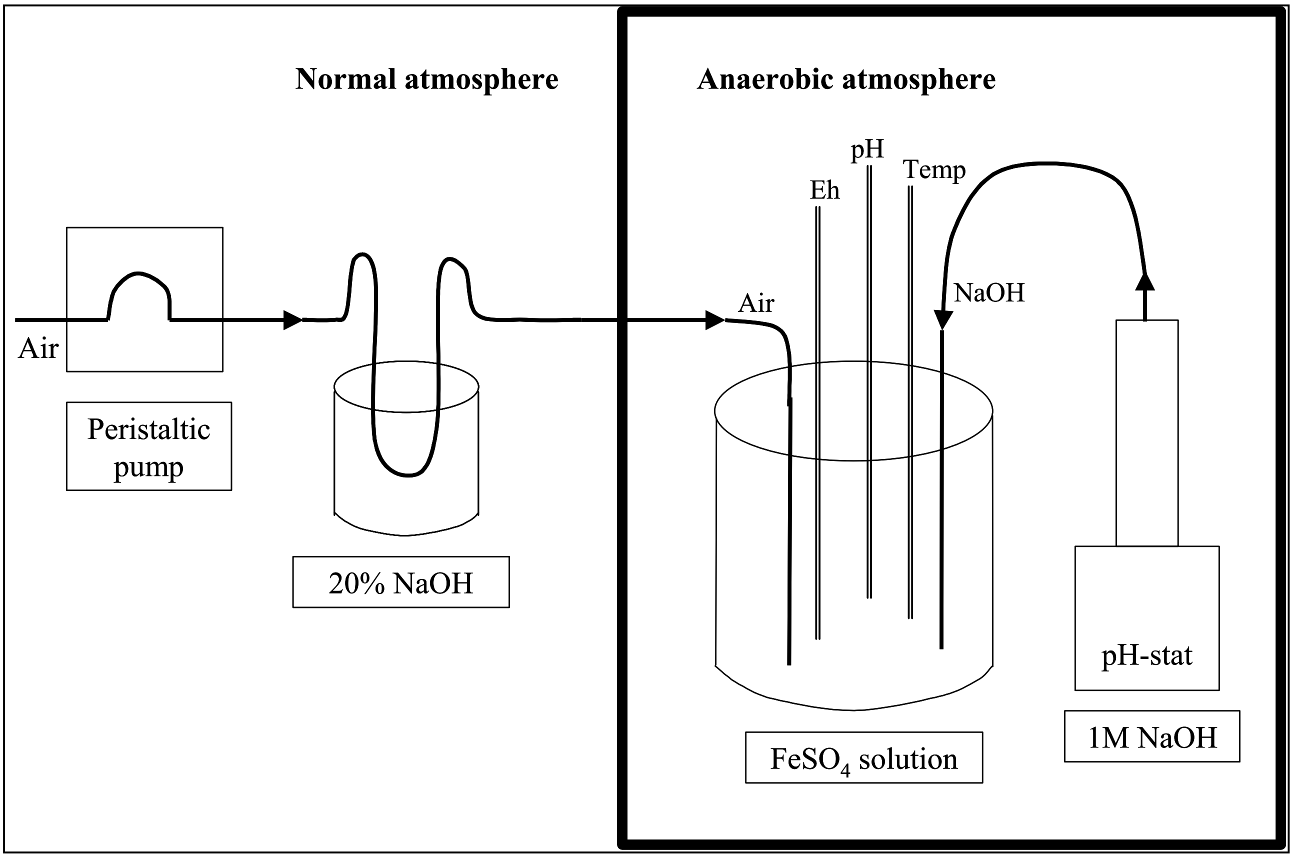

Figure 5.2: Experimental setup. GR synthesis takes place inside the glove box, denoted by the heavy border. Ambient air is pumped through a NaOH solution, to remove CO_2, and into the $FeSO_4$ solution. A pH-stat keeps pH constant and close to 7 through addition of NaOH. Eh, pH and temperature are continuously monitored.

negligible. The pH-meter was also supplied by Radiometer® and was calibrated with buffers of pH 4.00, 7.00 and 10.0. Electrode uncertainty was less than 0.1 pH unit. Adding this uncertainty to the pH fluctuations measured in the solution during suspension, the actual pH is 7+/-0.2. After synthesis was complete, the suspensions were transferred to sealed blue cap bottles and stored inside the glove box.

5.1.3 Reacting GR with Cr(VI)

Chromate was added to a suspension of relatively freshly prepared GR, less than 24 hours old and still suspended in the original supernatant to avoid disequilibria that could destabilise the structure. Cr(VI) was added as a K_2CrO_4 solution in various concentrations. The K_2CrO_4 powder used was 99.5% pure and supplied by Merck®. It was tested for adsorption of water by weighing, heating and reweighing, but there was no detectable mass change, so CrO_4^{2-} concentrations could be directly determined by mass added. The concentration of Cr(VI) was defined as a percentage of the amount of Fe(II) that is oxidised in GR: $Ox_{Cr(VI)/Fe(II)}$. When $Ox_{Cr(VI)/Fe(II)} < 100\%$, Fe(II) in GR is in excess and when $Ox_{Cr(VI)/Fe(II)} > 100\%$, not all Cr(VI) can be reduced by the GR present in suspension.

The amount of Fe(II) in GR_{SO4} was more tricky to determine. GR_{SO4} has a constant ratio of Fe(II)/Fe(III) ~ 2, so assuming GR_{SO4} is the only iron-containing solid present in the system, the amount of Fe(II) in GR can be determined from mass balance at any time during synthesis, based on the amount of Fe^{2+} left in solution. The following procedure was used: The mass of Fe-salt added to the reaction vessels was known; Fe^{2+} concentration in the supernatant was determined using spectrophotometry (Ferrozine method; Gibbs, 1976) and the balance of Fe total was assumed to be in the solid with Fe(II)/Fe(III) = 2. Determining the Fe^{2+} in the supernatant presented a problem. It was essential to conserve the solid to solution ratio, so that the suspension used to characterise the beginning material had the exact same properties as what would be reacted with Cr(VI). This means that the synthesised suspension had to be divided into two portions. This was done with a 5 mL automatic pipette while the solid material was kept in suspension with a magnetic stirrer. The uncertainty of this procedure was tested in three identical experiments. From the approximately 216 mL suspension, 50 mL was transferred to another bottle and the samples were freeze-dried separately. Although the supernatant was replaced twice with demineralised water to rinse out the salt before freeze-drying, white precipitate was observed in two of three samples. This means that the mass of GR included some uncertainty from a small amount of $NaSO_4$, but repeated rinsing risked to dissolve the GR and to preferentially wash out the interlayer sulphate. Uncertainty can be determined from expected mass in one of the bottles compared to the mass found there. If the assumption is correct that a GR suspension can be divided into aliquots without changing the solid/solution ratio, the mass ratio should equal the volume ratio of the two bottles. GRX2, in which no salt precipitation was observed, is used as an example for the uncertainty associated with dividing the GR batches into the experimental and characterising portions. The masses of GRX2 were 0.267 g in the 50 mL bottle, and 0.866 g in the 166 mL bottle.

Total mass: $0.267\text{ g} + 0.864\text{ g} = 1.133\text{ g}$

Total volume of suspension: $166\text{ mL} + 50.0\text{ mL} = 216\text{ mL}$

Expected proportion: $\dfrac{50\text{ mL}}{215\text{ mL}} = 0.233$

Found proportion: $\dfrac{0.267\text{ g}}{1.133\text{ g}} = 0.236$

% Difference: $\dfrac{0.236 - 0.233}{(0.236 + 0.233)/2} = \underline{\underline{2.2\%}}$

Table 5.1 gives the uncertainties based on each of three experiments. GRX1, which has the highest uncertainty of 7.8%, was also the one that appeared to have most salt precipitation. Still, the uncertainty is below 10% and for other two below 5%. Therefore, this method is regarded very acceptable in terms of maintaining the solid to solution proportion. This procedure makes possible the quantification of Fe(II) present in the solid in the experimental samples, without freeze-drying and rewetting the GR. The danger of changing its character is thereby avoided.

Four different concentrations were reacted: $Ox_{Cr(VI)/Fe(II)}$ = 9, 43, 82 and 131% . These values are in some cases averages of two sets of experiments. Some of the experiments were replicated for investigation with AFM and XRD in Denmark and TEM in Michigan, USA. GR concentration

Table 5.1: Three experiments were performed to determine whether a GR suspension can be divided with a pipette. The division was needed in order to characterize the material before reaction with Cr and the remaining material had to be of known volume.

Sample	Mass of material in 50 mL bottle	Mass of material in 215[a]/216[b] mL bottle	Expected proportion	Found proportion	% Difference
GRX1	0.269	0.800[a]	0.233	0.252	7.7%
GRX2	0.267	0.864[b]	0.231	0.236	2.2%
GRX3	0.266	0.918[b]	0.231	0.225	-2.8%

differs slightly between each synthesis, which reflects on $Ox_{Cr(VI)/Fe(II)}$. Exact concentrations for each experiment are listed in Table 5.2 and complete solution data are summarised in Appendix A. Variable reaction times, between 10 minutes and 10 days, were allowed in order to reach a stable end product. In the meantime, the suspensions were stored in blue cap bottles in the anaerobic glove box, except for those investigated with TEM, which were stored in blue cap bottles in ambient atmosphere.

5.2 TECHNIQUES AND SAMPLE PREPARATION

The green rust and other solids were characterised structurally and the supernatant was characterised chemically before and several times during reaction with Cr(VI). The green rust suspension of 200 mL + base (~ 15 mL) was split into two portions. About 3/4 was used for reaction with Cr(VI) and the rest was used to determine the Fe(II) content of green rust from aqueous Fe^{2+} analysis and to determine the purity of the synthesised GR by CT-XRD analysis. The solid and fluid phases were divided by driving the suspension through a 0.2 μm cellulose acetate filter, supplied by Sartorius®. Using a syringe, the suspension was sucked up via a plastic tube through the filter. The filter membrane with the solid attached was removed and left to dry inside the glove box, while the supernatant was transferred to test tubes with rubber caps. The test tubes were sufficiently airtight to allow negligible risk of oxidation during transport for immediate analysis.

Table 5.2: Concentration of Cr(VI) expressed as the amount of Fe(II) in GR that oxidises. When $Ox_{Cr(VI)/Fe(II)}$ is above 100%, there is excess Cr(VI) in solution. The Cr concentrations are different in the medium (*M*) and high (*H*) concentration suspensions because two different batches of GR suspensions and chromate solutions were used. The letters: L (low), M (medium), H (high) and VH (very high), referring to relative Cr(VI) concentration, or the average percentage will therefore often be used in this thesis instead of the exact values. T4 and T5 were investigated with TEM.

$Ox_{Cr(VI)/Fe(II)}$				
	Low (*L*)	**Medium (*M*)**	**High (*H*)**	**Very high (*VH*)**
S3			88%	
T1	9%			
T2		46%		
T3				131%
T4		40%		
T5			76%	

Cr^{6+} and Fe^{2+} were analysed using a Perkin-Elmer 55E spectrophotometer (SP). Cr^{6+} was complexed by diphenylcarbazide (APHA, AWWA and WPCF, 1975) and Fe^{2+} by ferrozine (Gibbs, 1976). Both complexes had a purple colour, the saturation of which is proportional to the concentration of the species. The detection limit for Cr^{6+} was 10 ppb and for Fe^{2+} less than 1 ppm. For both, the uncertainty was less than 10%. Total Cr and Fe were analysed with a Perkin-Elmer 5100 Atomic Absorption Spectrometer (AAS). This technique uses the absorption of light, emitted from the same element as one wants to measure the concentration of in the sample. So a specific lamp is used for each element and the concentration is proportional to the absorption. These are standard methods for these species. The detection limit for both Fe and Cr was 0.1 ppm and in a few cases, Cr was measured with a detection limit of 5 ppb. The uncertainty was no more than 10%.

5.2.1 X-Ray Diffraction (XRD)

XRD is one of the most important techniques for identifying a crystalline phase. Roentgen described X-rays in 1895 (Nuffield, 1966) and their approximate wavelength was estimated at about the order of 1 Å (Wiechert and Stokes, 1896, as cited by Nuffield, 1966). This fits the spacing of atoms so von Laue reasoned in 1919 that atoms in a crystal would diffract X-rays. He used a photographic plate to detect them and published the first diffraction photograph in 1912 (Nuffield, 1966).

When X-rays hit the electrons of an atom, they start vibrating and re-emit X-rays. If some of the energy is absorbed, X-rays of various wavelengths, depending on the properties of that actual atom, are emitted. However if no energy is absorbed, X-rays are re-emitted with the same frequency and wavelength, simulating reflection of the incoming X-ray. When many X-rays are emitted simultaneously, such as from a solid illuminated by a beam of X-rays, some interfere destructively while others that are in phase, interfere constructively. If enough X-rays are emitted in phase, such that the intensity of that set becomes very high, they can be detected as a peak of intensity. Such peaks are diffraction maxima and occur when the Bragg equation is fulfilled:

$$n\lambda = 2d \sin\theta, \qquad \text{Eq. 4}$$

where λ represents the wavelength of the X-ray, d, the spacing of the lattice planes, θ, the angle of reflection and n, the reflection order, which must be a whole number (Figure 5.3). This relationship was formulated by W. L. Bragg and is called the Bragg condition or Bragg law.

Unknown compounds may be identified, based on their diffraction peaks, because these reveal the atomic arrangement within the compound. To withdraw as much information as possible, the peak intensities are optimised. This is accomplished by ensuring that enough identical crystal lattice planes cause Bragg diffraction during recording. One way to ensure this is by having a large

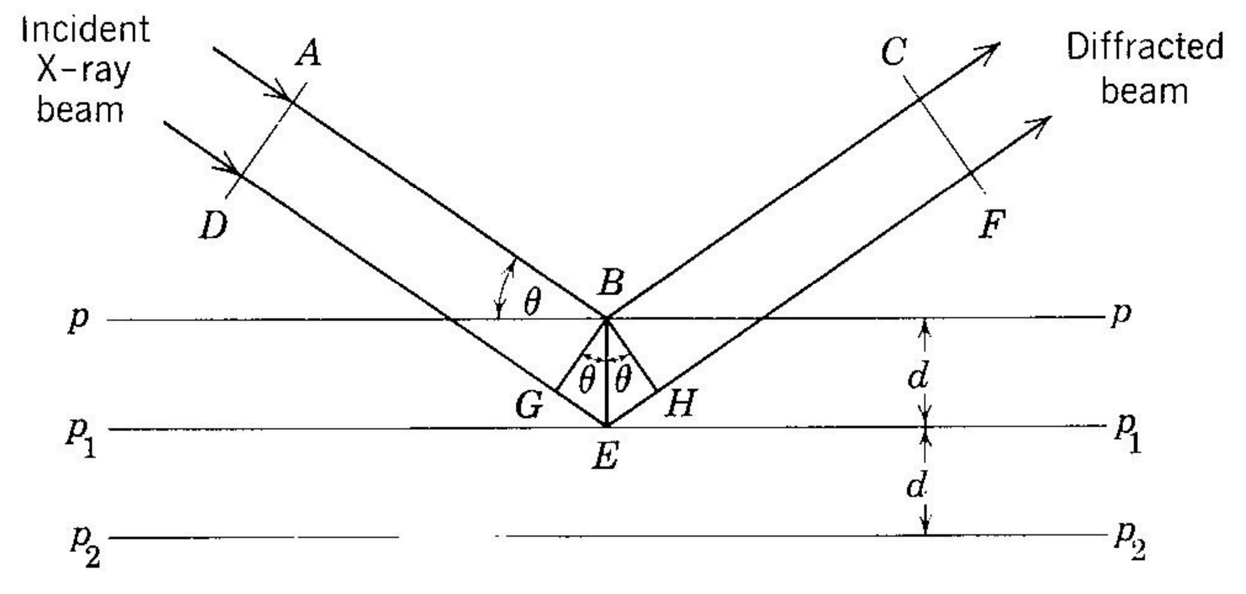

Figure 5.3: The principle of Bragg diffraction from crystal planes separated by the distance, *d*, and oriented with an angle θ to the incident beam of X-rays. An X-ray is only diffracted when $2\sin\theta = n\lambda/d$, where λ is the wavelength of the incident X–ray and *n* is a whole number (from Nuffield, 1966).

number of crystallites, as a powder, with all possible orientations. The powder diffraction method was used in this work. To further increase intensities, the crystallite powder is rotated during recording. The resulting X-ray paths from a powder sample are schematised in Figure 5.4. A cone, coaxial with the incoming beam and with a half-apex angle of 2θ, illustrates the diffraction from a single set of crystal planes that are oriented in all possible direction during data recording. With more diffracting lattice planes, the result is several coaxial cones. Detecting these X-rays on a plate yields a ring pattern as opposed to the spots obtained with diffraction from a stationary single crystal. Data are usually plotted as the integrated intensity in counts versus 2θ or the interplanar distance, the d-spacing, where d can be calculated from λ and θ (Figure 5.5) by Braggs law. The diffracted X-rays can be detected simply on photographic film or as with modern X-ray diffractometers, with a charge coupled device (CCD). A CCD consists of thousands or millions of electrically isolated pixels, which can accumulate charge in response to beam intensity. The charge is emptied into an amplifier and the pixels are then recharged. The digital signal is continuously sent to a computer that processes the data. The intensity of the spots and rings varies as a function of θ, crystal and symmetry class (Nuffield, 1966).

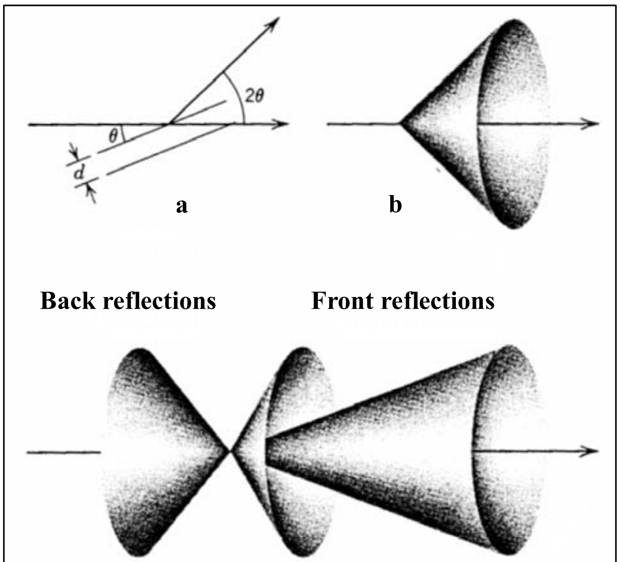

Figure 5.4: The principle of powder diffraction. a) Geometry of diffraction from a plane (see also Figure 5.3); b) the resulting diffraction cone when a plane is rotated and/or simultaneously present in many crystallites; c) different sets of diffracting crystal planes produce cones with different 2θ values, so if the detector is planar, the result is rings of various radii (from Nuffield, 1966).

5.2.1.1 Advantages, Disadvantages and Limitations

X-ray diffraction is a bulk method, giving the average interplanar distances and average intensities of diffraction from the crystal planes. XRD traces allow relatively easy identification of minerals by comparison with known patterns and it is usually possible to identify more than one mineral in a mixed sample. To be detectable, a compound generally must constitute at least 2 weight percent of the sample and be distributed in random orientation. In order to have enough differently oriented crystallites in the small area of bombardment, it is essential that the particles are very small, usually below 45 μm (Nuffield, 1966). Synthetic green rust crystals are on the order of 1 μm in size, so they fit very well within this limitation. Sometimes small size is not enough, however, because anisotropic crystals may orient with a preferred crystal face against the sample holder; so randomisation of orientation must be insured during sample preparation. XRD yields only structural information; so chemical analyses are often needed for interpretation because isostructural compounds produce similar patterns.

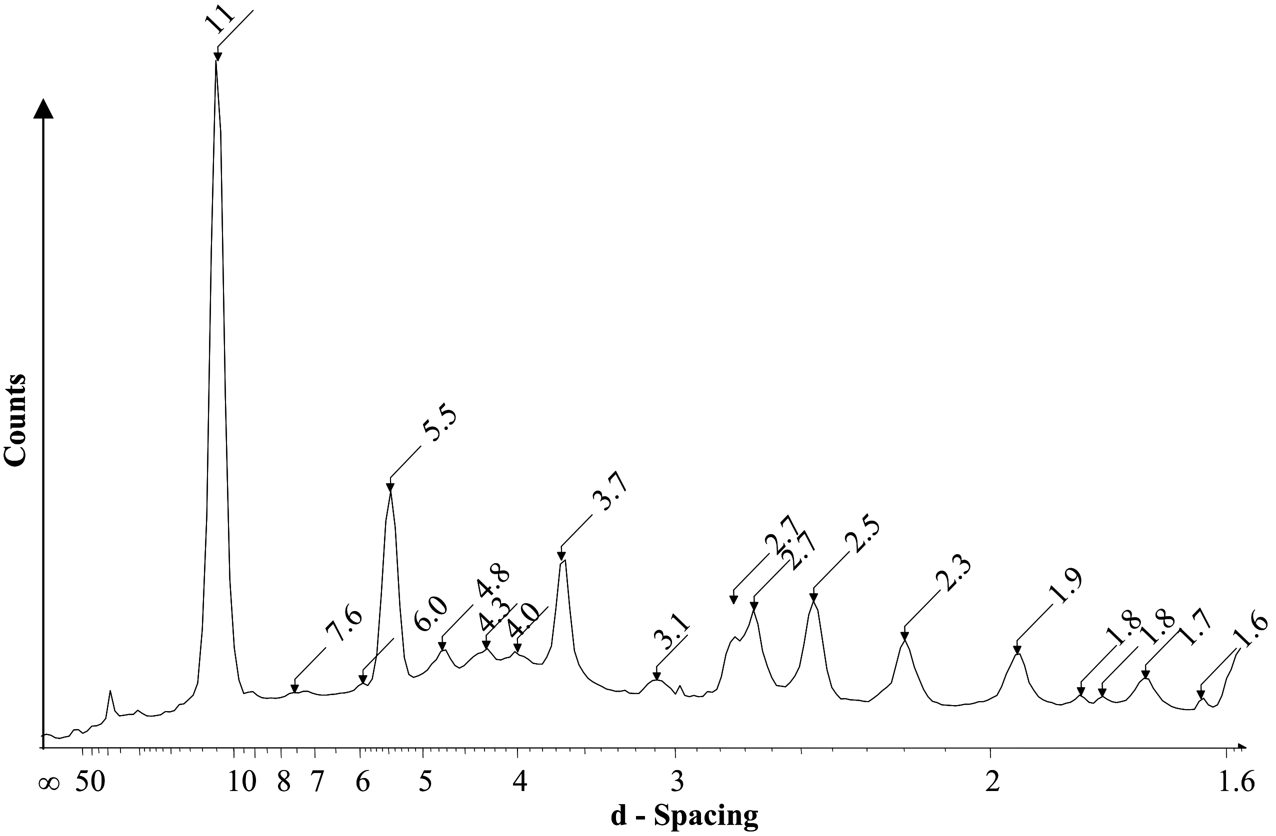

Figure 5.5: CT-XRD trace of GR_{SO4}. The three tallest peaks correspond well with published d-values (Hansen, 2001). The trace and d-values shown are typical for samples from this study. It was not the intention of this work to collect enough statistics to propose definitive d-values. That is done elsewhere (Christiansen et al., in progress).

5.2.1.2 Sample Preparation

During transport and measurements of samples containing GR, it was essential to exclude oxygen to prevent oxidation of the Fe(II). In the glove box, the solids were transferred to capillary tubes (CT), with a diameter of 0.4 mm and sealed with paraffin. No visible colour change was observed inside the CT's even after several days outside the glove box and in tests, XRD showed no development of a new phase. This lead to the conclusion that GR remained stable inside the capillary tubes long enough to be examined with XRD. To make sure that all possible orientations of the crystals were represented in the capillary tube, the dried aggregates from the filter paper were finely parted either by grinding in a piece of paper or with tweezers in a small plastic cup. After removing the capillary tubes from the glove box, they were placed for 15 minutes in an ultrasonic bath to increase the density of crystals for X-ray analysis. The ultrasonic treatment may have induced preferred orientation, leading to intensity increase of some peaks relative to others. Although peak intensity is of utmost importance when investigating the structure of a compound or when quantifying mixtures, peak intensity is less important when identifying a compound. The XRD patterns obtained in this work are only used to verify compounds, so the possible preferred orientation has no consequence for the interpretations in this thesis.

5.2.1.3 Instrumentation

The apparatus used for this work was a BrukerAXS four-circle diffractometer, equipped with a molybdenum source and a graphite filter. The generator was set at 40 kV and 37 mA. The sample, introduced in the sealed capillary tube, was mounted in the sample holder with wax. A distance of 12 cm was kept between the sample and the detector, which was placed at an angle of $2\theta = -13°$ relative to the radiation direction. The sample was rotated during measurements, which lasted 15 minutes and all measurements were performed at room temperature. The data were treated in the program GADDS for WinNT 3.330©. The recorded ring pattern was unwarped and calibrated against a quartz standard (Figure 5.7). To produce an XRD trace, integration of the intensities was performed (Figure 5.6). Unfortunately, the detector adds "hot spots" to the image, which show up as spikes on the XRD trace, so these are not included in the interpretation. The traces were compared to known mineral patterns, using the program EVA 3.0.0.8©, to identify the phases present.

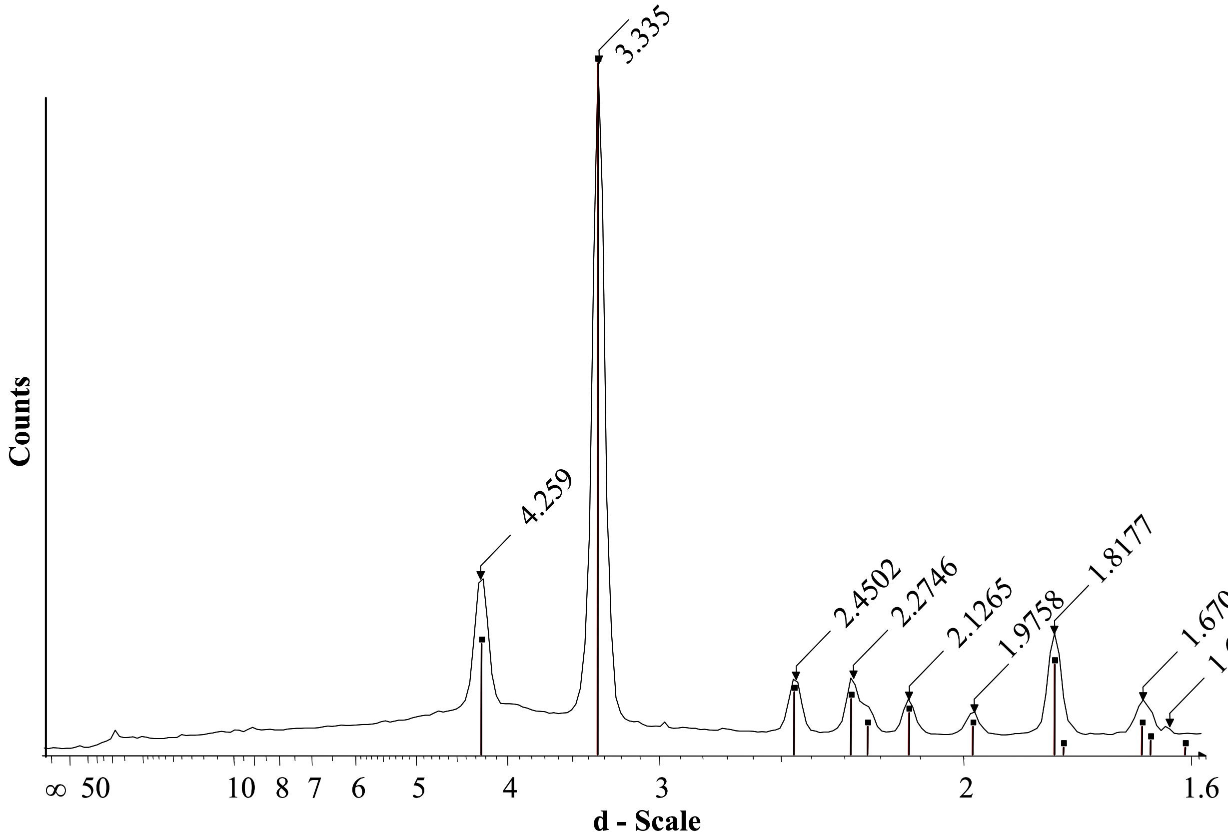

Figure 5.7: A typical CT-XRD trace of the quartz-filled capillary tube used for calibration of the data. The bars represent standard quartz peaks and the identical d-values show that the data are well calibrated.

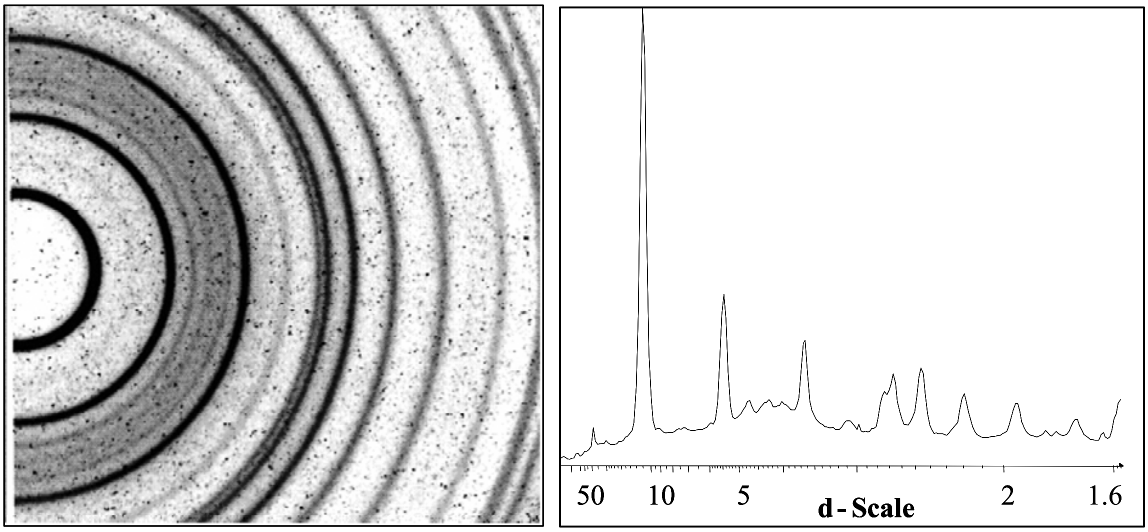

Figure 5.6: a) CT-XRD ring pattern of GR_{SO4}, where dark represents high intensity; b) an XRD-trace, which is the integrated intensity of a similar ring pattern as a function of *d* (Å), taken from a band along the radius of the circle. The black spots on the ring pattern are hotspots on the detector, which cause false peaks in the XRD trace such as that at about *d* = 50 Å. These must be removed if the pattern is to be interpreted in detail.

5.2.2 Atomic Force Microscope (AFM)

AFM is a highly surface sensitive technique from the family of scanning probe microscopes (SPMs), the first of which were invented by Binnig, Rohrer, Gerber and Weibel (Binnig et al., 1982). The first SPM was the scanning tunneling microscope (STM), which maps the electron density of a surface by measuring tunneling currents between a conducting probe and a conducting or semi-conducting sample. In the mid-eighties, Binnig, Quate and Gerber (1986) developed the atomic force microscope (AFM), which works equally well on insulators by feeling atomic forces acting between a tip and the sample surface. The AFM probe is usually a Si_3N_4 tip, mounted on a cantilever. For the experiments reported here, the tips had a spring constant of 0.06 to 0.58 N/m, approximately the same as a hair.

To record AFM images, the tip and sample are brought close enough that Van der Waals, electrostatic and possibly capillary and magnetic forces are felt between them (Eggleston, 1994). Attracting forces makes the tip bend toward the surface and repulsive forces bend it away. Theory assumes a tip so sharp, that only one or a few atoms are at the point (Figure 5.8). This allows resolution of very small force changes as the tip interacts with the surface. Figure 5.9 illustrates the AFM setup. In order to detect deflection of the cantilever, thus the relative magnitude of the surface forces, a laser beam is aimed at the back of the cantilever, which is covered with gold to increase reflectance. A mirror redirects the beam into a photosensitive diode and the position of the laser spot reveals the position of the tip relative to a reference level. The sample scans under the tip, which moves up and down as it senses nano-Newton force changes.

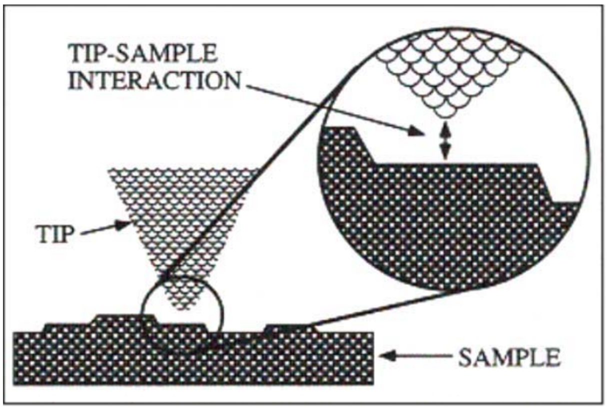

Figure 5.8: Principle of atomic force imaging: An extremely sharp tip is brought close enough to the sample that forces are felt between individual atoms on the surface of the tip and the sample (from Eggleston 1994).

The small sample movements in the *x*, *y* and *z* directions are controlled by a piezoelectric scanner. A computer feedback loop ensures that the tip does not crash into structures on the surface but still remains close to the surface. Images of variations of both height and force are constructed in the computer by assigning a colour to the *z*-dimension. Height changes are measured by keeping the tip-sample interaction force constant and force changes are measured directly from the diode signal in constant height mode. Often a researcher collects a height image as the surface is scanned in one direction and a deflection image as it is scanned in the other direction, simultaneously recording two images. Figure 5.10 shows images obtained using the two different imaging modes. Height images are the only ones that give true height differences, but deflection images aid the researcher's visualisation of the surface because these images looks like real photographs, where a light appears to shine from one side or the other.

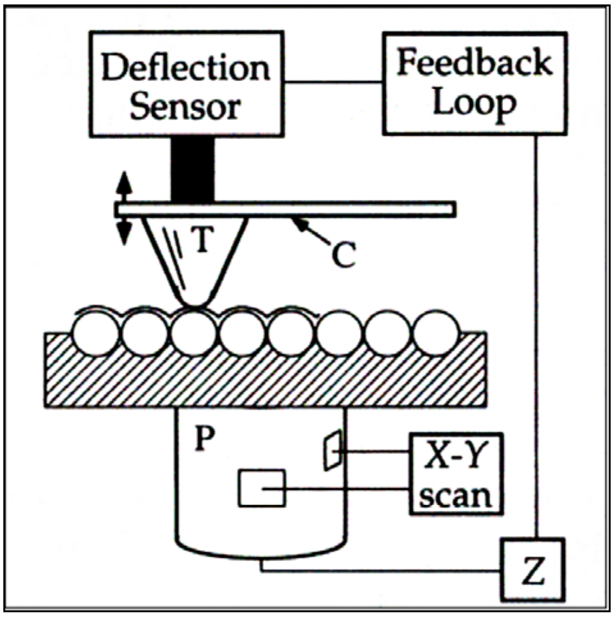

Figure 5.9: Illustration of an AFM system: The sample is mounted on a piezoelectric scanner (P). As the tip (T) is brought close to the sample, attractive and repulsive forces are felt, causing the cantilever (C) to deflect. The deflection sensor, often a system consisting of laser light aimed at the back of the cantilever and a photosensitive diode that detects the movements of the laser, sends information to a computer about these movements. Simultaneously with recording the image, a feedback loop is activated as the computer responds to the movements by sending orders to the scanner to reposition (from Eggleston, 1994).

5.2.2.1 Advantages and Disadvantages

AFM is an *in situ* imaging technique, where samples can be examined in air or fluid at ambient pressure and temperature, thereby allowing observation of reactions that resemble those in nature. AFM is ideal for mapping micro- and nano-topography of minerals, because it can resolve very small height differences. Deflections of fractions of an Ångström (10^{-10} m) allow imaging at the atomic scale. One limitation of AFM is the need for very flat samples. Structures larger sharper than the tip itself cannot be resolved so they cause artefacts. One such example is Figure 5.10, top left corner, where the tip in one place has been imaged by a large aggregate of particles instead of the tip imaging the surface. Because tip and sample are actually interacting, the morphology of the tip has an important influence on the image. A blunt tip results in loss of detail and multiple tips cause doubling or tripling of features (Figure 5.11). On an image the doublets have the same spacing as the two or more tips on the tip. Forces other than Van der Waals, electrostatic and magnetic forces, such as frictional and capillary forces, may also influence the tip-sample interaction and cause artefacts.

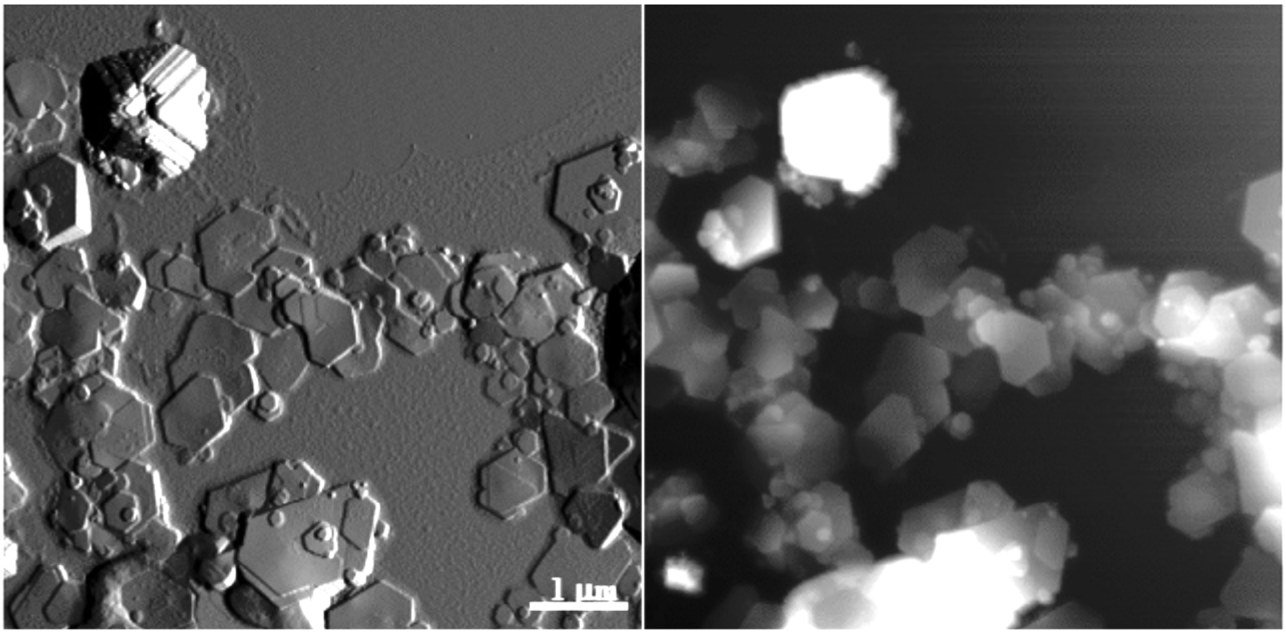

Figure 5.10: AFM deflection (left) and height (right) images of GR_{SO4}. The deflection is in this case recorded from left to right while the height image is recorded as the scanner moves back. A common artefact is seen in the upper left corner. The pyramid-shaped tip is imaged when it moves over a particle that is larger or sharper than the tip.

In addition to tip artefacts, the scanner may also add error to an image. Instead of keeping exactly the same x-y origin, the scanner may move hysterically, causing a tiny net slip while operating. The result is that the image appears distorted (Figure 5.12). Distortion, or “drift”, decreases when the electronics have been turned on for an hour or so before scanning. If needed, drift corrections can be made using a method developed by Henriksen and Stipp (2002). All possible artefacts are closely coupled with the tip, sample and scanning conditions as well as the properties of the surrounding media: humidity of the air, viscosity of the solution and so forth. After imaging various materials in various conditions innumerable times, however, experience reveals most artefacts.

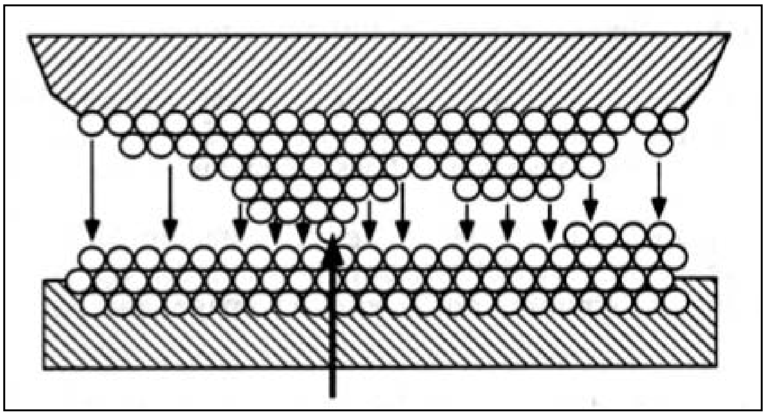

Figure 5.11: The basic principles of AFM imaging assume interaction between one atom at the surface of the tip and one atom at the surface of the sample. However, this is not the case in practice. At this high resolution, the tip seems more or less blunt and several atoms may interact. If two or more of these atoms interact closely with the surface, then the image is a function of both or all. This results in blurring of the image and sometimes evidence of double or multiple tips are seen as features that reappear in the image with equal spacing corresponding to the spacing between the two or more tiny tips (from Eggleston, 1994).

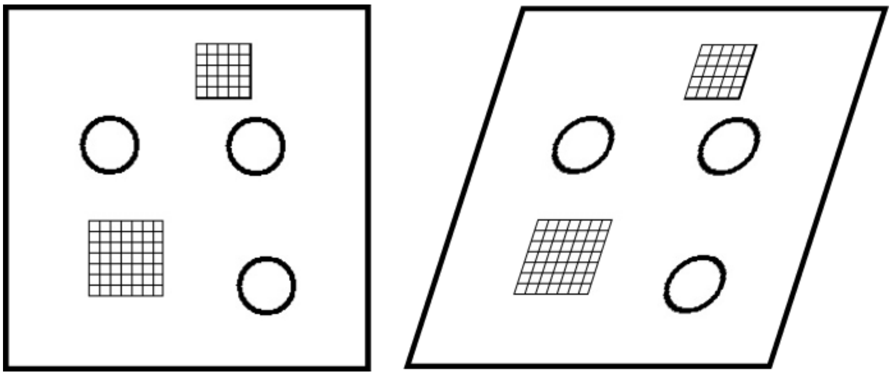

Figure 5.12: Hysteretic piezoelectric scanner movement causes distortion of AFM images during imaging. This is especially critical when imaging at the atomic scale where distances and angles are important. In this case, the rhomb needs to be restored to a square (Stipp and Henriksen, 2002)

5.2.2.2 Sample Preparation

Samples for AFM analysis were taken at the same time and from the same batches as samples for chemical analysis and XRD. Because green rust crystals are so small, a substrate was needed for them to be imaged with AFM. Muscovite has extremely good cleavage, leaving absolutely flat, clean surfaces so it served this purpose very well. A piece of muscovite was attached to a sample holder with double-sided tape. It was cleaved with tape immediately before a droplet of GR suspension was placed on it with a disposable pipette. After settling for up to one minute, the suspension was flushed with demineralised water to avoid crystallisation of salts and to dislodge loosely attached particles that would foul the tip. Excess water was quickly and carefully sucked away with a paper tissue and the samples were left to dry for at least 10 minutes or up to several hours before imaging.

Avoiding oxidation of GR was essential so during imaging, the entire microscope was fitted into the glove box (Figure 5.1). A light microscope was placed above the AFM, inside the chamber, to facilitate a good view of the tip and sample for selecting the area to be imaged and for the tip approach. All cables were led outside the glove box through gas-tight plugs in the plastic walls. The microscope was usually mounted on a flexible silicon jelly-pad to reduce vibrations when recording images smaller than 1 μm^2 and during all imaging, oxygen and humidity control fans and pumps were turned off to avoid image-distorting vibrations. While the fans were off, the oxygen level did not rise above the detection limit of 0.5 ppm O_2 over periods of up to 10 hours.

5.2.2.3 Instrumentation

The SPM was a Digital Instrument Multimode IIIa, operating in contact force mode. The tips were in most cases standard Si_3N_4 tips and in some cases sharpened Si_3N_4 tips. There were no obvious differences between images obtained with one or the other type of tip. The samples were attached to an E-scanner, which has a maximum scan area of 10 μm × 10 μm. For maximum-sized images, a scan speed of 2.4 Hz was usually chosen. The scan speed was increased as the image size was decreased. The software for imaging control and data treatment was Nanoscope version 4.23r6©.

5.2.3 Transmission Electron Microscopy (TEM)

TEM is a powerful tool that combines high-resolution images with chemical composition determined from X-ray spectroscopy and structural information gained from electron diffraction. The textbook written by Williams and Carter (1996) is the basis for this review on TEM and associated techniques. Transmission electron microscopes were designed based on the concept that electrons are particles that behave as waves and therefore can be focused. In 1932, Knoll and Ruska presented the first TEM images. When a high voltage electron beam is pointed at a sample, it interacts with the material and a variety of signals are produced, including scattered electrons and X-rays (Figure 5.13). Electrons can be scattered in two ways: elastic scattering, where the electron keeps its energy, or inelastic scattering, where the electron looses energy because it interacts directly with the nucleus of an atom. Elastic scattering is the major source of image contrast, whereas inelastic scattering reveals the chemical identity of the interacting atom. In TEM, it is usually the forward-scattered electrons that are detected, so in order to get a strong signal, the sample needs to be very thin. How thin depends on the average atomic number of the sample and the primary electron beam energy, but usually it is possible to produce good images when the sample thickness is less than 100 nm. Electrons are easily scattered, so a high vacuum ($\sim 10^{-7}$ Torr or $\sim 1.3\times10^{-10}$ atm) needs to exist in the analytical chamber between the electron gun, sample and the detector to minimise scattering caused by other media than the specimen.

The illumination system consists of an electron gun that emits electrons at a predefined voltage and known wavelength; electron lenses that focus and defocus the beams; apertures for selecting specific electrons; and a detector that collects the electrons after interaction with the specimen. The electron gun used for this work was a thermal field emission gun (FEG). An FEG consists of a cathode and two anodes. The cathode is usually a tungsten tip that forms a very fine needle. The

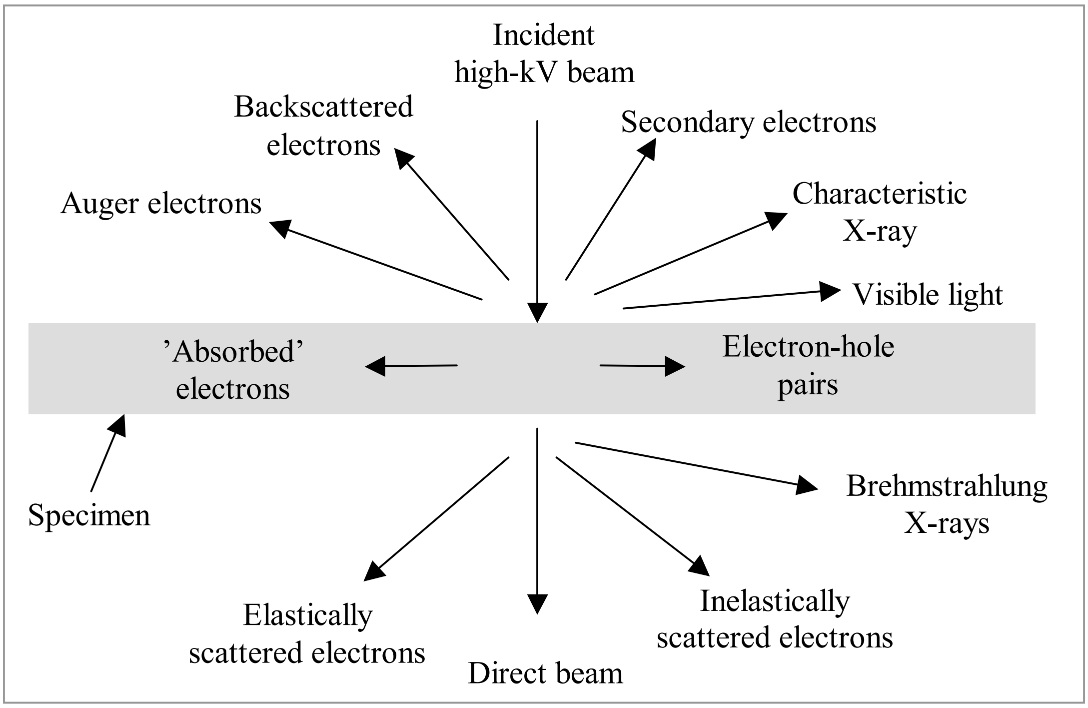

Figure 5.13: Some of the signals that are generated when an electron-beam interacts with a specimen (after Williams and Carter, 1996).

first anode provides the extraction voltage to pull electrons out of the tip, while the second anode accelerates them to 100 kV or more in the direction of the sample. Condenser lenses and apertures are placed in the microscope column to optimise the beam. Electrons can be focused in a magnetic condenser lens, which consists of two parts: i) a “polepiece” made of soft magnetic material, usually soft iron, in the middle of which a hole, called the bore, is drilled, and ii) copper coils inducing a magnetic field in the bore of the polepiece. Some lenses have two polepieces separated by a gap. These two may be part of the same piece of iron, or they may be two separate parts as schematised in Figure 5.14. Two or three condenser lenses are placed in the illumination system, before and after the sample. The specimen is introduced into the gap of the lower lens, termed the objective lens. Adjustable apertures, which are simply holes in electron-absorbing metal disks, are placed in the beam path to enable selection of a specific fraction of the electrons.

After the electrons have passed through the specimen, lenses and apertures, they reach the detector. The microscope used for this work was equipped with a CCD for detection. The CCD continuously transfers the digital signals to a computer so the image or diffraction pattern can be viewed on screens. The cycle is repeated very fast and in some CCD’s 30 frames are displayed per second, allowing for easy navigation across the specimen. However, such high frequency is associated with

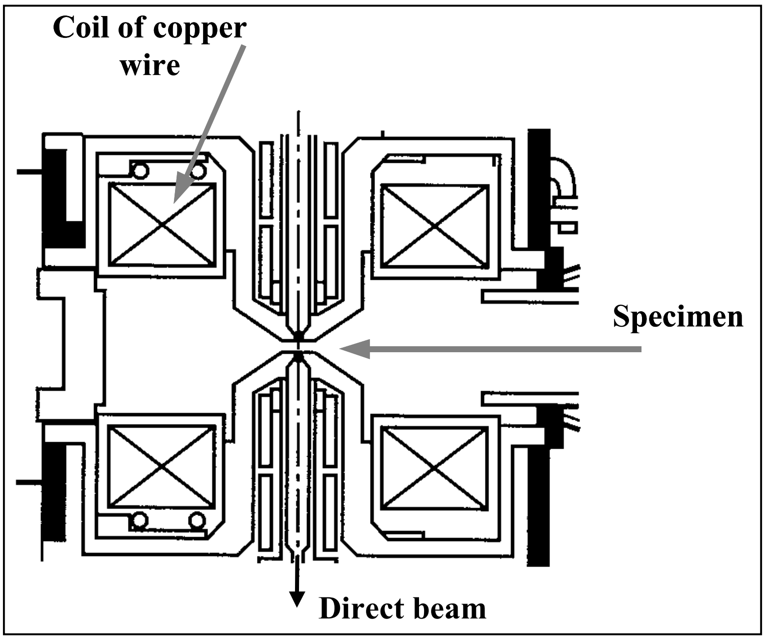

Figure 5.14: A split polepiece objective lens. Copper coils induce a magnetic field in the bore through which the electron beam passes. The specimen is placed between the upper and lower polepieces (after Williams and Carter, 1996).

intensity loss. The illumination system is not perfect and neither are the mathematical models interpreting the signals, so some information needs to be given higher priority than other, depending on which information is wanted. The various techniques associated with TEM give different information about the specimen properties. Each technique uses a different probe; different fractions of the signals generated; and different mathematical models are applied to interpret the results. For this work the following imaging techniques were used: bright field TEM (BF-TEM), high-angle annular dark-field scanning TEM (HAADF-STEM) and high resolution TEM (HR-TEM). To obtain structural information, selected area electron diffraction (SAED) was performed and to deduce chemical information, X-ray energy dispersive spectroscopy (XEDS) was applied.

5.2.3.1 Conventional TEM and Associated Techniques

BF-TEM is a conventional TEM (CTEM) imaging technique, where the images are formed mainly from diffraction contrast. The direct beam is selected for detection by aligning an objective aperture in the direct beam path causing high-intensity areas to appear bright, hence the name. The opposite method is dark-field TEM (DF-TEM) imaging, where the scattered diffraction spot of interest is selected using an objective aperture, which removes all other diffraction contrast in the image. In BF-TEM imaging, the specimen is illuminated with a beam of parallel electrons, the size of which is controlled by an aperture. The magnification range used for this work was 2,500 to 100,000 times, giving imaged area dimensions ranging from about 7 μm to 150 nm across.

In HAADF-STEM imaging, contrast is a function of atomic number (Z), specimen thickness and atomic density. Thus, for well-prepared TEM specimens, the images are maps showing relative chemical differences. In this technique, a very fine probe (~ 0.2 - 1.0 nm depending on the user’s demand for beam current) is formed and scanned across the specimen, with the beam remaining parallel to the optic axis. The electrons that are used to form an image are mainly incoherent, inelastically scattered electrons at high angle (50-80 mrad. at the inner angle of the detector). These are detected with a ring-shaped detector, an annular dark-field (ADF) detector. This can be a fluorescence plate, which changes scattered electrons to light that is then transformed to an electrical signal. The image magnification used in this study was 10,000 to 300,000 times, giving approximate imaged area dimensions from about 8 μm to 250 nm across.

With HR-TEM, it is possible to obtain crystallographic information of the specimen. The HR-TEM image allows observation of atomic arrays if the area is crystalline enough, whereas in amorphous areas no lattice fringe is observed. In order to observe the lattice fringe in crystalline areas, the specimen needs to be tilted in relation to the beam. High-resolution images obtained during TEM analysis for this work are used to infer relative differences of crystallinity between the various compounds in the suspensions. The magnification for this task was typically 300,000 to 500,000 times giving approximate imaged area dimensions from about 50 nm to 30 nm across.

SAED is a reflection of atomic spacing in the sample. It is a Fourier transformed image in reciprocal space, formed at the back focal plane in the microscope column. The focal plane is where all parallel beams are focused, so a set of well-defined spots on the SAED image indicates that the material contains many parallel crystal planes that diffract the beams, i.e. a high degree of crystallinity (Figure 5.15). All diffraction spots that appear in SAED patterns satisfy the Bragg condition. The image resembles a single crystal X-ray diffraction pattern, but the important difference is that X-ray diffraction is mainly kinematical, whereas the electron diffraction is primarily dynamical. Kinematical theory considers only single scattering events, whereas in dynamical theory, multiple scattering is considered. Upon re-scattering, the electrons may

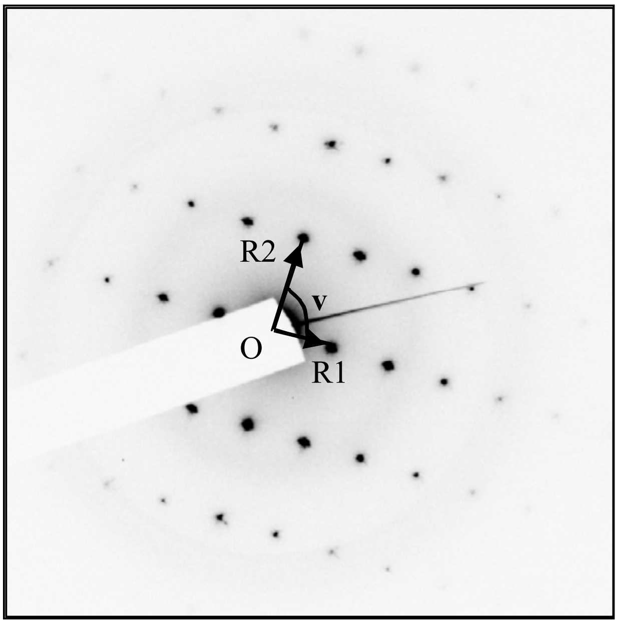

Figure 5.15 SAED pattern. Very well-defined spots are produced from highly crystalline particles, in this case magnetite. The length of the vectors OR1 and OR2, as well as the angle (v) between them, are used when comparing the pattern to patterns of known compounds in order to identify the phase.

recombine with the direct beam. Thus, the intensity of the diffraction spots in an SAED is not proportional to the crystal parameters as it is in an XRD pattern. Instead the spot intensity varies strongly as the thickness varies, because thicker areas within the width of the beam cause more re-scattering events than thinner areas.

In SAED, instead of forming an image from the direct or possibly diffracted electron beam, all scattered electrons are represented by their scattering angle. In the case of a poorly crystalline material, the diffraction maxima are broadened and in amorphous materials, only a diffuse halo is seen. Well-defined spots and ring patterns revealed in SAED can be quantitatively analysed and comparison with known crystal parameters allows structural identification of the compound. In the case of this work, the crystallographic parameters of potential minerals were compared to mineral powder diffraction files (MPDF). Several parameters, including the crystal system, the lattice parameter and the *d*-values are required to determine the phase. The calculation process is as follows (Figure 5.15): i) Calculate the camera constant in the dimension of the actual SAED; (ii) Measure the distance between the intersection of the direct beam (O) and two most adjacent diffraction spots (R1 and R2) as well as the angle (v) between the vectors *OR1* and *OR2*; and (iii) use these parameters in the diffraction analysis database to find matches with known compounds. The relative difference between the ideal value for the potential mineral and the measured value is the error, which should be less than 5% for the results to be reliable; less than 3% is ideal.

XEDS is a spectrometric technique that gives information about the chemical composition of the specimen. The XEDS system detects characteristic X-rays emitted after close interaction between an electron and an atom. The characteristic X-rays, most useful for XEDS, are emitted when a high-energy electron penetrates the outer electron shell and ejects an inner-shell electron. To decrease the overall energy of the atom, the hole fills itself with an outer-shell electron of higher energy than needed to occupy that space and the surplus energy is emitted as an X-ray (Figure 5.16). The energy of this X-ray is characteristic for the element because the distance, and thus the energy difference between the two shells for each atom, are unique. The X-ray is named after the shell that initially looses its electron and the shell from which the hole-filling electron comes. The first letter denotes the shell (K, L, M…), the subscripted Greek letter denotes from how many shells away the electron came ($1 = \alpha$, $2 = \beta$, $3 = \gamma$…) and if there is a number next to the Greek letter it denotes the subshell. Thus, if a K-shell hole is filled with an L-shell electron, a K_α X-ray is produced. If a K-shell hole is filled with an M-shell electron, a K_β X-ray is produced. A $K_{\alpha2}$ X-ray results from the loss of the second K electron. K_α produces the strongest peak in an XEDS spectrum and K_β has about 10-15 % of the K_α intensity, because the probability of ejecting a second electron is lower.

Figure 5.17 shows a typical XEDS spectrum from a selected spot on GR_{SO4}. The XEDS system used in this study is an EDAX detector with EDAX genesis software. It is able to analyse the elements with $Z > 5$. Semi-quantitative analysis can be performed using the genesis software, basically including the term of the integrated peak intensity in the XEDS profile. The analysis is only "semi-quantitative" because it is carried out without a standard sample. In general, the error of the analysis is about ±10 wt%, but practically it is within ±5 wt% in most cases. To obtain reliable results, total counts must be above 3000; more total counts are required for better statistical certainty. It is routine to obtain such an XEDS spectrum. In addition, XEDS elemental maps can be

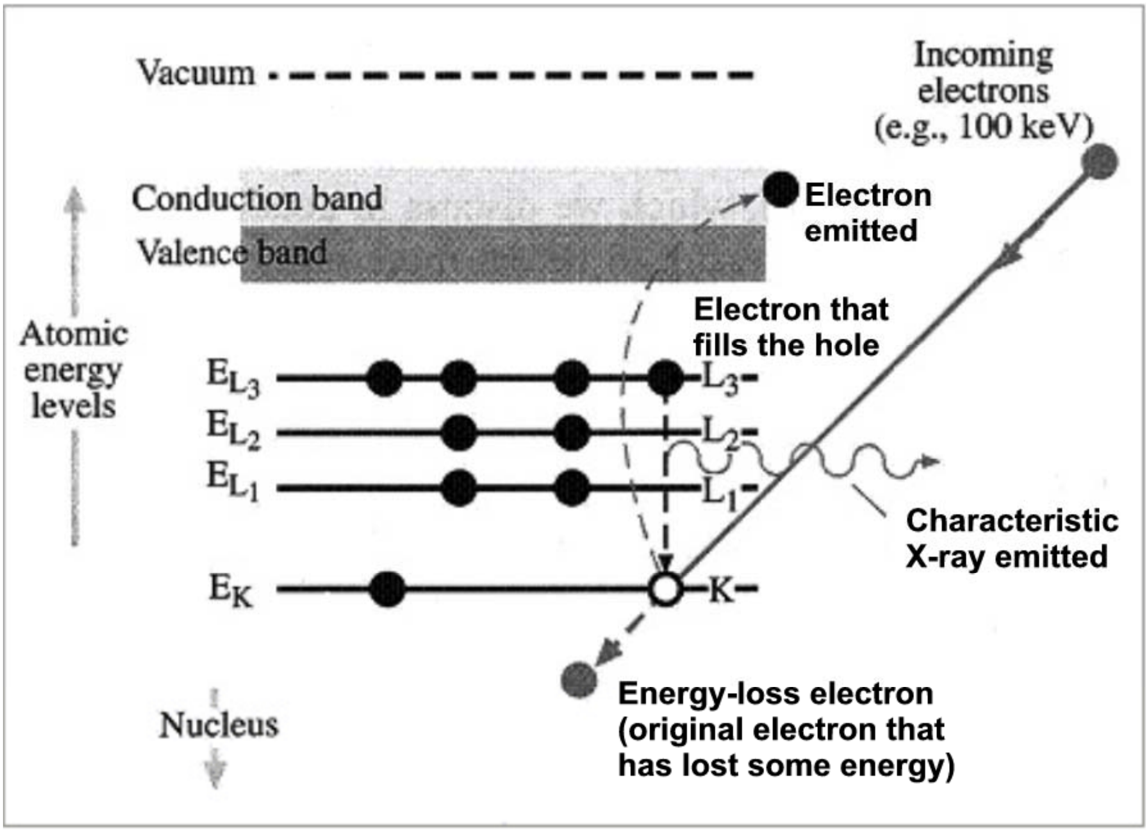

Figure 5.16: Characteristic X-rays are emitted when an inner-shell electron is ejected and a higher-energy electron from another shell drops to fill the hole. The energy of the X-ray emitted is exactly equal to the energy difference between the two shells and is therefore one of the "characteristic" wavelengths of the element. The produced X-ray is in this case a $K_{\alpha3}$ (after Williams and Carter, 1996).

produced in STEM mode using a 0.5 nm probe. The microscope used in this study, has Emispec ESvision STEM mapping control software, featuring drift correction elemental mapping, which allows easy elemental mapping at scales of a few nanometers. The acquisition time for each pixel needs to be set as longer than 1 sec with reasonable count rate. A specific X-ray peak, e.g. $FeK_{\alpha1}$, is then selected to create an elemental map. The value of each pixel is assigned as the integrated peak intensity.

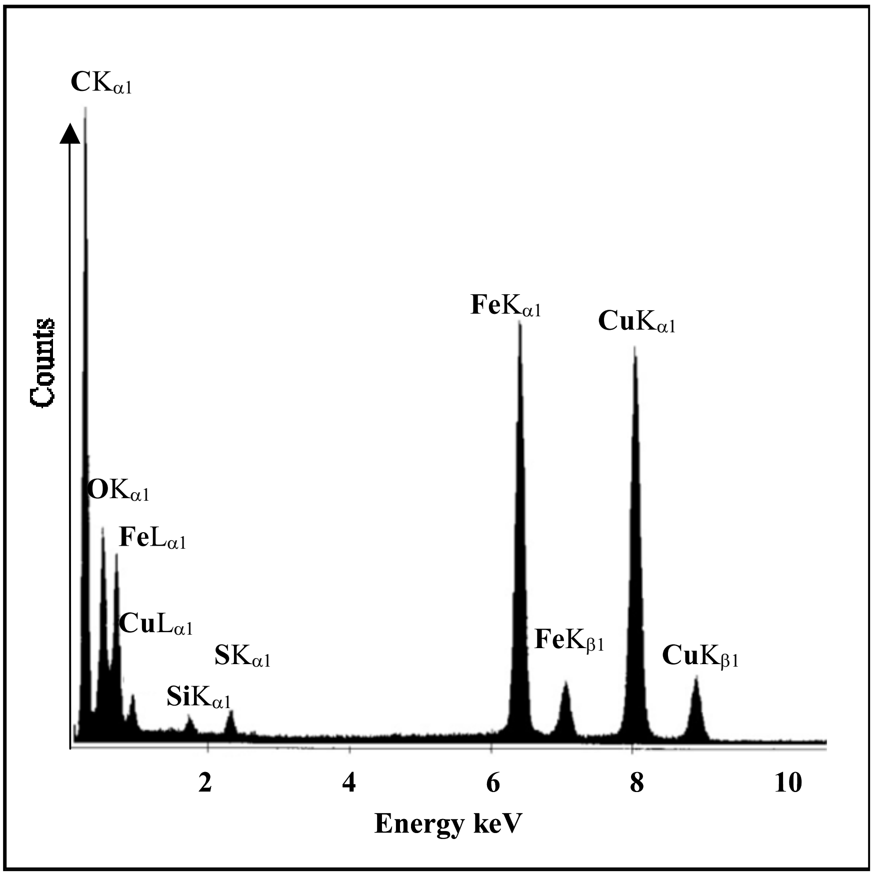

Figure 5.17: An XEDS spectrum from pure GR_{SO4}, containing Fe, O, S and a trace of Si. The carbon peak is derived from supporting holey carbon mesh and the copper peak comes from the copper grid used to fix the particles. Fe and Cu are both represented by three lines e.g. $K_{\alpha1}$, $K_{\beta1}$ and $L_{\alpha1}$.

5.2.3.2 Advantages and Disadvantages

With a TEM one can obtain images of microstructures, diffraction patterns and spectra of characteristic X-ray energies, revealing the chemical composition of the sample. All the analyses can be performed at the exact same location in the nanometer-scale range, making TEM a very powerful tool. On the other hand, the specimen volumes that can be analysed are very limited. Therefore, other complementary analytical techniques, capable of performing analyses at larger scale, are frequently required. As with all imaging techniques, with TEM, one must be careful of artefacts. In TEM, these can be caused by electron irradiation. The powerful electron beam sometimes destroys crystal structure. To avoid misinterpretation of the data, one has to quickly examine the susceptibility of the specimen to radiation damage by observing SAED or HR-TEM images during time-series exposures to the electron beam before recording actual data. Typical examples of radiation effects are amorphisation of minerals by electron irradiation and holes created by the STEM probe.

The need for very thin samples can be a serious problem, especially in the case of HR-TEM. GR crystals are usually well below 50 nm thick and are therefore ideal, as they are, for TEM analysis. Still, when materials are thicker than one atomic layer, there is chemical and structural variation in all directions, meaning that the electrons passing through the specimen are scattered as a function of interaction with elements all through the thickness of the sample. The sum of this scattering is what is detected, allowing for no depth resolution. Also the structure, parallel to the incident beam direction, is hard to determine. One way to solve that particular problem is to tilt to another zone axis and record a second SAED. Another constraint is the need for high vacuum, which in the case of GR causes dehydration, which may modify the structure. Vacuum is, however, also an advantage because it prevents Fe(II) oxidation in GR.

5.2.3.3 Sample Preparation

The microscope was located in the Electron Microbeam Analysis Laboratory (EMAL) at the University of Michigan, USA, so samples for TEM investigations were prepared from a separate batch of synthesised GR. During transportation from the glove box in Copenhagen, Denmark to the glove bag in Ann Arbor, Michigan, the GR suspensions were kept in airtight Pyrex bottles with Teflon-lined blue cap lids. For extra security for anaerobic conditions inside the bottles, a paraffin layer of about 5 mm was deposited all around the top of the bottles. Leakage of oxygen into the bottles would have changed the blue-green colour to olive-green or yellow. No colour change of the GR was observed; instead the suspension remained dark bluish-green, giving confidence in a good seal.

Once inside the nitrogen-filled glove bag, the seals were broken, chromate was added and the samples were prepared for TEM. Cupper grids with holey carbon mesh were used as substrate for the solids. A droplet of GR suspension was placed on the substrate and flushed with demineralised water after 5 seconds. After drying for 15-30 minutes, the samples were placed in small plastic containers that were sealed with parafilm and removed from the glove bag. The microscope was in a different building so approximately 5 minutes passed before the samples were under vacuum. The samples were quickly transferred in air from the plastic container to the sample holder and introduced into the vacuum of the TEM, usually within one minute. This short period of exposure to air did not result in any evidence for oxidation of the dry GR crystals; morphology and structure observed after 1 minute of air exposure were the same as that observed with AFM and XRD without air exposure.

5.2.3.4 Instrumentation

All TEM data were produced using a FEG-JEOL 2010F with FasTEM system. A CsGatan Multi-scan camera, TV camera and Gatan Imaging Filter (GIF) were installed in the system. Data acquisition was carried out using Gatan Digital Micrograph version 3.6.4. The microscope was operated at an acceleration voltage of 200 kV, produced from a zirconated tungsten (100) thermal field emission tip. Vacuum was maintained at approximately 1.5×10^{-7} torr. The spatial resolution was 0.10 nm of lattice resolution and 0.25 nm for point-to-point resolution in CTEM mode and 0.17 nm for lattice resolution in STEM mode. In HAADF-STEM the probe size was 0.5 nm. The XEDS system had an EDAX r-TEM detector with EDAX Genesis software. The detector was a horizontal, ultra-thin window, Si-Li X-ray detector, which could detect all elements with $Z > 5$. The XEDS spectra were produced by rastering the beam in STEM mode with a 10×10 nm, 15×15 nm or 30×30 nm beam. Exposure time was in all cases longer than 90 seconds. All SAED patterns were obtained with a camera length of 30 cm. The DOS-based software used for diffraction pattern analysis was named DA and copyrighted by K. Tsuda, at the Research Institute for Scientific Measurements (RISM), Tohoku University, Japan.

5.3 UNCERTAINTIES AND REPRODUCIBILITY

Apart from the uncertainties of the instruments, which are assessed under each technique, human-induced uncertainties may contribute to the data confidence level and therefore the reasonable extension of the interpretations.

5.3.1 Uncertainty Related to the Experimental Set Up

The procedures used when reacting Cr(VI) with GR_{SO4}, induce some amount of error in quantification. i) The concentration of Cr(VI) is reported in relation to the amount of Fe(II) incorporated in GR because that is the reducing agent under examination. The $FeSO_4{\cdot}7H_2O$ powder, which had been open to the atmosphere several months, may have water adsorbed in addition to the crystalline water. This decreases the relative amount of Fe(II), thereby disturbing the mass balance for $Fe(II)_{GR}$. The Fe content of the melanterite was not determined for this project, but before this paper is prepared as a manuscript for submission to ES&T, this uncertainty will be determined. However, there are indications in the experiment, that the uncertainty is low. The synthesis method used in this study resembles a titration because when GR_{SO4} forms, pH drops and OH^- is added to keep pH at 7. In an experiment, which is presented later, the initial amount of Fe^{2+}, added as $FeSO_4{\cdot}7H_2O$ by weight, was oxidised fully to a ferric end product. Base was added at a constant rate but when the point was reached where GR_{SO4} was no longer formed, the base addition stopped. At this point, 0.01707 mol NaOH had been added to the assumed 0.0100 mol Fe^{2+} initially present. This gives a ratio $R_{Fe(II)/OH} = 0.586$, which is very similar to the $R_{Fe(II)/OH} = 0.585$ usually used in the "non-static pH" method (Hansen, 2001). This indicates that the chemical composition of the melanterite was very close to the expected.

ii) Dividing the suspension with a pipette induces an uncertainty of 2.2% to 7.8% in the examined cases. Because the bottles with lesser salt precipitations after freeze-drying had uncertainties below 3%, the general uncertainty arising from that procedure is considered less than 5%. If the uncertainty was higher, the amount of $Fe(II)_{GR}$ present in the reaction suspension would not be as expected and that would probably lead to unexpected amounts of Cr(VI) reduction when $Ox_{Cr(VI)/Fe(II)}$ is close to 100%. iii) The relatively high concentration of Fe^{2+} remaining in the supernatant after synthesis of GR, may have contributed to reduction of Cr(VI) directly in solution, thereby decreasing the effective concentration of Cr(VI) available for reduction by Fe(II) in GR. This issue is discussed later in this thesis and will be resolved before submission of a manuscript.

However, the effect from dissolved Fe^{2+} is considered unimportant for the interpretations made in this study. iv) XEDS showed that the GR_{SO4} crystals were associated with silica that must have dissolved from the glassware. Silica, of measured Si/Si+Fe counts percentages of in average 2.3% but up to 3.9%, could potentially passivate the GR surface thereby decreasing the concentration of accessible Fe(II) at the solid-solution interface.

5.3.2 Reproducibility of Observations

When examining the solid phases, both with AFM and TEM a large number of randomly chosen sites on the sample were examined. This was to ensure that interpretation was based on typical or average behaviour rather than a possible anomaly. A number of factors could have introduced variations in morphology and chemical behaviour between the various batches. i) The TEM samples were exposed to air for at least half a minute and in some cases as much as 10 minutes. ii) The glove bag used for preparing TEM samples was not completely oxygen tight, so samples analysed by TEM may have a very slight component of GR oxidation by oxygen, in contrast to AFM samples. However, there was consistency between observations with AFM and TEM; what was observed with one technique, was usually also observed with the other, indicating that that the possible oxidation during sample preparation for TEM did not alter the particles significantly. It also indicates that the samples were representative of the suspensions. iii) Flushing AFM and TEM samples with deionised water to release loosely attached particles may have caused GR structure instability by washing out some of the interlayer anions. Because the particles were left to dry immediately after flushing, any transformations of the GR crystals would probably have been small. iv) The observed trace amounts of silica may have influenced the result. The reduction of Cr(VI) was extremely fast in this study, so the effect from silica on rates of reaction is considered negligible, but whether it has a minor effect on the end product or mechanism is difficult to determine without comparing with experiments of silica-free GR in reaction with Cr(VI).

6 GREEN RUST SYNTHESIS

6.1 SYNTHESIS OF GR$_{SO4}$

The formation of GR in nature remains a topic of hot debate and examination of its properties in laboratory studies continues. Some parameters have been well-examined, but because of GR's instability in ambient conditions, it is difficult to gain an overview of the transformation from a reduced Fe(II) compound through GR to a fully oxidised product. Monitoring the chemical behaviour of the system during GR synthesis aids the understanding of natural GR formation. Knowledge about the behaviour of the pure GR system during addition of O_2 is also the basis for understanding the interaction between GR and other redox sensitive compounds. For this work, GR$_{SO4}$ was synthesised at a constant pH of 7 through addition of hydroxide ions, while Eh was allowed to change.

Eh is the electrode potential. The Nernst equation relates the potential of the system to the transfer of electrons between compounds and the ratio of the redox species. For the generalized reaction:

$$j\ \mathrm{red}^{\mathrm{x}} = i\ \mathrm{ox}^{\mathrm{x+n}} + ne^{-} \qquad \text{Eq. 5}$$

$$Eh = Eh^{\circ} + \frac{2.3RT}{nF}\log\frac{[\mathrm{ox}^{\mathrm{x+n}}]^{i}}{[\mathrm{red}^{\mathrm{x}}]^{j}}\ , \qquad \text{Eq. 6}$$

where *j* and *i* are the stoichiometric coefficients of the oxidised and reduced species, *n*, the number of electrons in the where Eh° is the standard potential, related to the standard Gibbs free energy change ($\Delta G_r°$) through:

$$Eh^{\circ} = \frac{-\Delta G_r^{\circ}}{nF}\ . \qquad \text{Eq. 7}$$

R represents the gas constant, *T*, the temperature in °Kelvin, written reaction and *F*, the Faraday constant. $[\mathrm{ox}^{\mathrm{x+n}}]^{i}$ and $[\mathrm{red}^{\mathrm{x}}]^{j}$ denotes the product sum of the activity products of the oxidised and reduced compounds (Krauskopf and Bird, 1995).

The validity of a measured Eh depends on the system. If there is only one redox couple, such as Fe^{2+}/Fe^{3+}, then Eh gives the relative concentration of those two in solution. Thus, if Eh increases, then some Fe^{2+} is removed from solution relative to Fe^{3+} and if Eh decreases, it means that the concentration of Fe^{3+} increases relative to Fe^{2+}. Stipp (1990) showed that in an Fe(II)-Fe(III)-SO_4-H_2O system of pH range 1-4, Eh can confidently be calculated from the activity products of Fe^{2+} and Fe^{3+}. However, during GR synthesis in the glove box where there is a partial pressure of H_2 (P_{H_2}) of about 2%, the following reaction co-exists (Stumm & Morgan, 1996):

$$H_2 = 2H^+ + 2e^- \qquad E° = 0.00\ V \qquad \text{Eq. 8}$$

This reaction contributes to the electromotive force of the solution. This is supported by the observation that Eh of the initial $FeSO_4$ solution was lower if there was a higher hydrogen pressure, and higher if the opposite was true. The effect was not investigated further because the hydrogen pressure remained relatively constant throughout each GR synthesis, meaning that the contribution of the H_2 potential was constant, and the Eh values were only used as relative values, not exact values.

The Eh and OH^- addition curves resulting from full oxidation of Fe^{2+} indicate the nature of the chemical reactions of the system (Figure 6.1). In the initial $FeSO_4$ solution, pH is below 4 so OH^- is added to reach pH 7 within the first minute. Eh is initially positive, but as the base is added it drops and becomes negative. This indicates that Fe^{3+} was present but as pH becomes less acidic and approaches neutral, Fe^{3+} has a strong tendency to hydrolyse, forming $Fe(OH)^{2+}$, $Fe(OH)_2^+$ and $Fe(OH)_3^0$ whereby the amount of free Fe^{3+} species in the solution decreases. Fe^{2+} does not hydrolyse until pH is well above neutral so in this synthesis system, pH changes mostly affects the concentration of Fe^{3+}. When base is added, the colour of the solution shifts from colourless to transparent bluish-green. The colour that is produced with the “non-static pH” method, where NaOH and $FeSO_4$ is mixed before oxidation, is more bluish (Christiansen et al., in progress). In that method, $FeOH_{2(s)}$ is formed as a precursor for GR_{SO4}. $FeOH_{2(s)}$ is white, but the substitution of some Fe^{3+} produces the blue colour. The colour change observed with the “constant pH” method, probably indicates the formation of GR itself, directly. Schwertmann and Fechter (1994) argue that the precursor for GR in the “constant pH” method is ferrihydrite. This theory was supported in their work by the complete transformation of freshly precipitated ferrihydrite to GR by drop-wise addition of a $FeCl_2$ solution (Schwertmann and Fechter, 1994). In this current work, the suspension

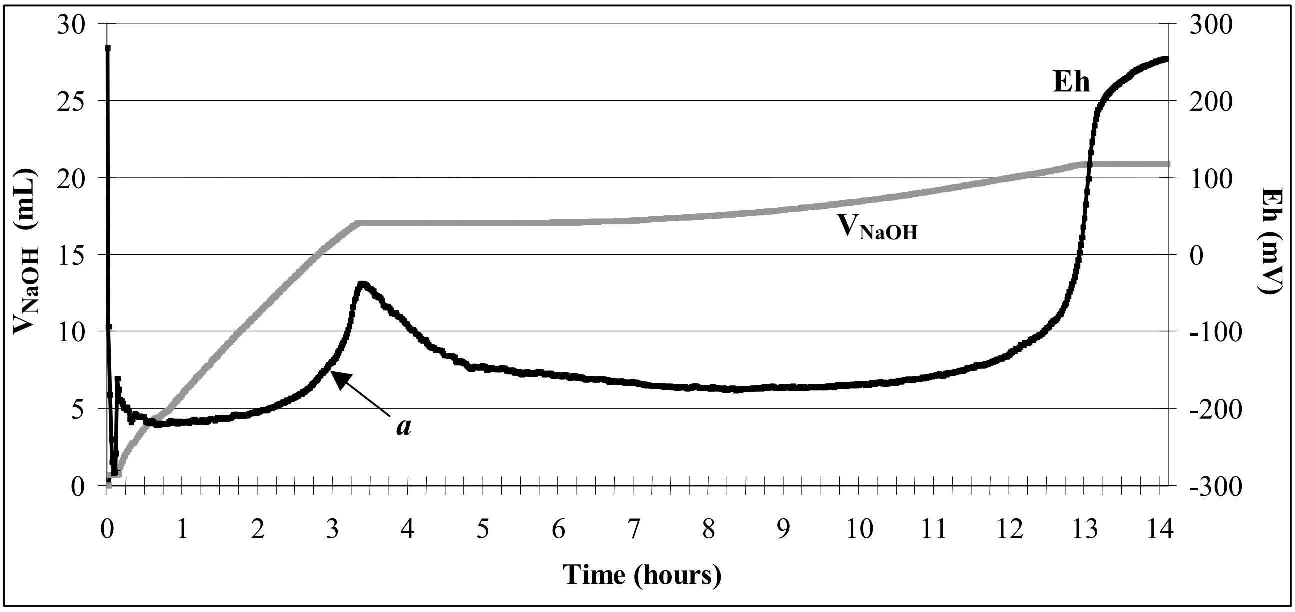

Figure 6.1: During synthesis of GR_{SO4} at pH 7, Eh evolution and the volume of NaOH added are recorded to monitor the conditions in the suspension. In this synthesis, the rate of base addition from start to about 3 hours was 0.8 mL/min. All Fe(II) was oxidised to Fe(III) after 14 hours. To make GR for reaction experiments, oxidation is usually stopped at about point *a* on the Eh curve.

does not adopt the yellow/orange colour of ferrihydrite before precipitation of GR, but that may be because the solid concentration is too low. If there is a precursor compound produced in the "constant-pH" method, it is never high enough to be detected with XRD, so its presence and possible identity remains unknown at this point.

Eh decreases during the first 15 minutes in Figure 6.1 and stabilises at about Eh = –200 mV where the rate of NaOH addition also becomes constant, indicating steady production of GR. After approximately 2.5 hours, the Eh curve begins a steep rise indicating an increase in the Fe(III)/Fe(II) ratio. Oxidation continues to produce Fe(III) so the rise in Eh can be interpreted as a relative depletion of Fe(II) which has been precipitated as GR. After an additional hour, a local Eh maximum is reached and Eh begins to drop. This indicates a shift back towards domination of Fe(II) in solution, which may be caused by dissolution of GR. About 5 minutes before the apex, base addition stops caused by a slight pH rise (Figure 6.2). pH rises because less hydroxyls are suddenly used or because some are released back to solution, indicating the end of GR formation and initiation of GR dissolution. The subsequent pH drop indicates that OH^- is quickly being removed again, however. Assuming that formation of GR_{SO4} has ended, a new phase, demanding hydroxyl must be forming. Goethite (α-FeOOH) is the end product of the air oxidation of the suspension, so its formation already is likely.

After five to six hours, the surplus of hydroxyls has been consumed and pH starts to drop, so base is again added, but at a lower constant rate. The colour of the suspension gradually turns more light green towards yellow and XRD shows increasing amounts of goethite (data not shown). After 12 to 13 hours, the suspension is yellow-orange and Eh rises dramatically. This can be explained by the exhaustion of Fe^{2+}. After 13 hours, oxidation has ended. No GR can be seen in XRD patterns. A full oxidation of $FeSO_4$ solutions under the described conditions yields goethite (α-FeOOH) when performed in our laboratory, but Koch and Hansen (1997), whose method is the base for the synthesis in this study, obtain lepidocrocite (γ-FeOOH). The reasons for this difference have not been investigated and will not be discussed further here. They are, however discussed in the

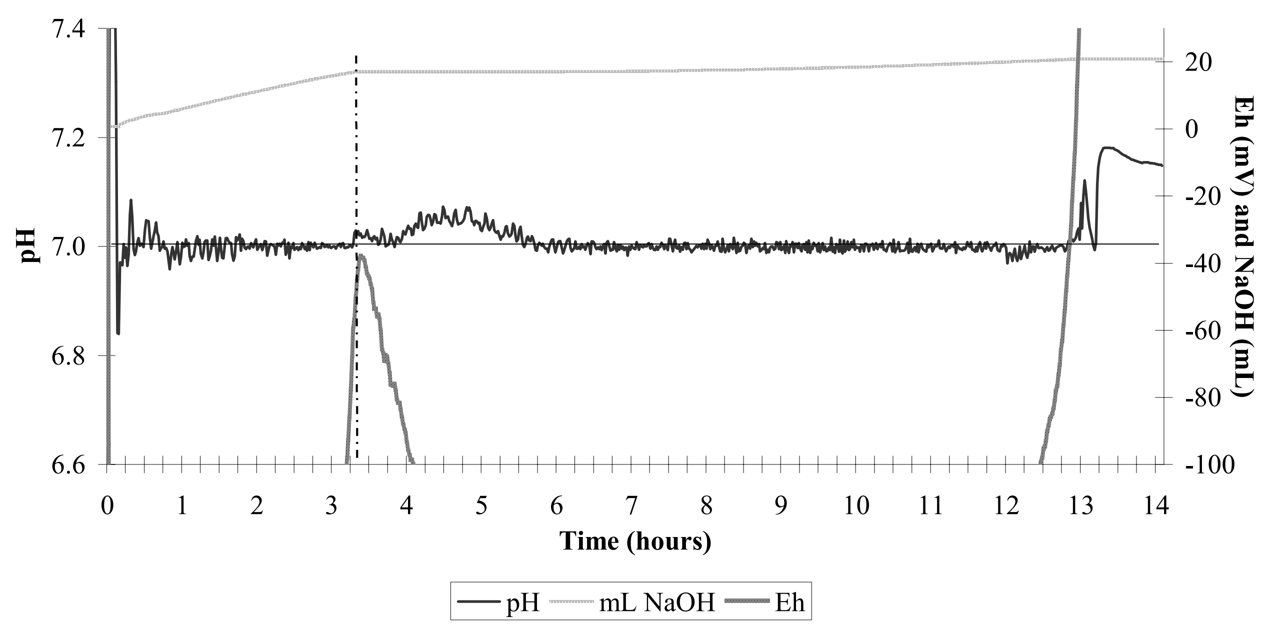

Figure 6.2: pH curve from the same experiment as shown in Figure 6.1. The local maximum of Eh is seen at about 3.5 hours. The pH curve shows a little rise whereafter it falls back again at about 3.75 hours. This behaviour is probably caused by the release of hydroxyls from initial GR dissolution. The larger "bubble" from about 4 to 5.5 hours is caused by a too high base addition dose at about 3.5 hours. The pH-stat uses a calculation procedure that averages over several minutes or more to minimise fluctuations around the set point. However, that also reduces the reaction time resulting in occasional addition more base than can be consumed by the reaction.

Masters thesis of Bo Christiansen (2004). The batches that were used for reaction with chromium were oxidised to approximately the point *a* on the Eh curve before the air inlet was removed.

After synthesis, the GR batches were all analysed with XRD (Figure 5.5), most were examined with AFM (Figure 6.3) and some with TEM (Figure 6.4). The purity and quality of the batches were closely related to oxidation rate, provided the synthesis was terminated in the stable area of GR formation. It was impossible to determine the oxidation rate from the rate of air input because the reaction vessels were not closed so some O_2 may have escaped before oxidising Fe^{2+}. Instead, the base addition rate was used to calculate the oxidation rate. In the above example, 0.08 mL base/min were added. The batches that were used for TEM analysis were oxidised much faster at a base addition rate of 0.12 mL/min. The high input of oxygen resulted in zoning of some of the GR crystals and was probably also the cause of formation of magnetite (Fe_3O_4), observed with TEM (Figure 6.4 and Figure 6.5). The zones of the GR's did not vary significantly in elemental composition, for example Fe and S, and AFM analyses, performed a month later, revealed no morphological differences between these GR samples that were synthesised rapidly compared to the first batches. Most likely, the zoning was the result of beginning oxidation, which caused structural changes. The magnetite crystals were not detected until illuminated by the TEM. With routine examination by CT-XRD the crystals were too small and/or proportionally too few to be detected so the batches were accepted. However, after witnessing the magnetite crystals with TEM, CT-XRD analyses were performed again after a bit more than a month on the same suspensions that had been stored in paraffin sealed blue cap bottles. At that time, the magnetite crystals had grown in size and perhaps proportion and were detected as very small peaks in the GR XRD trace (Figure 6.6). The magnetite could have formed in solution during ageing of the suspension or very small magnetite crystals, undetectable by XRD, could have formed during synthesis.

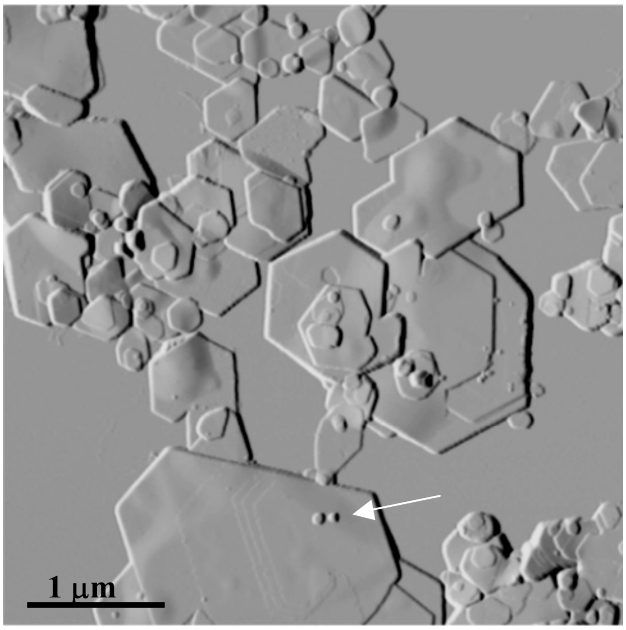

Figure 6.3: AFM deflection image of GR_{SO4}. The crystals are about 10-35 nm thick. The smallest crystals, about 100 to 250 nm in diameter, may be magnetite (white arrow).

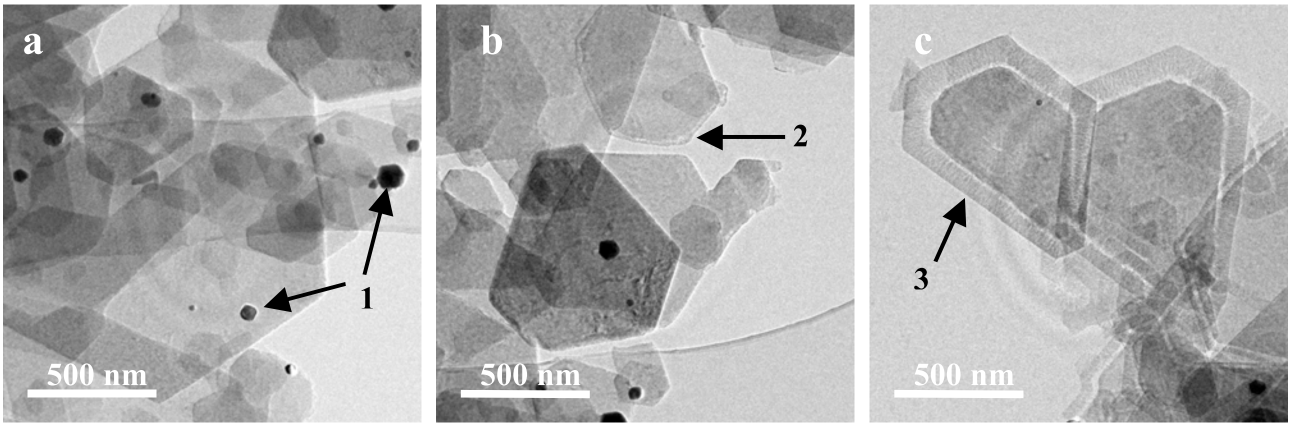

Figure 6.4: TEM images of GR_{SO4} before reaction with chromate. The GR crystals have clear hexagonal outlines. The suspensions used for TEM analyses contained magnetite (arrows 1) and some showed oxidations edges (arrows 2 and 3). The structural and chemical differences between the rims on the edges and the rest of the GR crystals were to small to be detected by SAED or XEDS. Probably, too fast aerial oxidation during synthesis caused the formation of magnetite. The rims are an evidence for slight oxidation by air, which apparently begins at the edges of the GR crystals. The oxidation features and the presence of magnetite have minor, if any, influence on the reduction of Cr(VI).

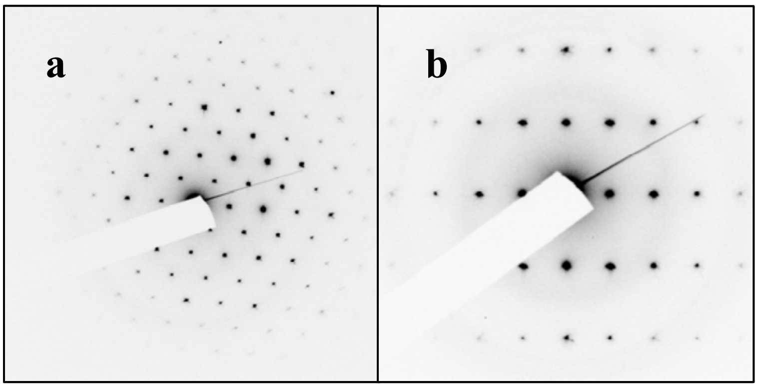

Figure 6.5: SAED patterns of two crystals of magnetite, similar to the small black crystals in Figure 6.4 denoted by the arrows 1. Crystals with two different orientations were observed in the samples and the combined images reveal the cubic crystal structure. The images are shown in negative for ease of printing.

The goal of these experiments with GR_{SO4} was to provide information that allows us to understand the natural systems, so these are imitated when possible. The natural formation of GR is better simulated with the constant pH method because large and fast fluctuations of pH are unlikely in most natural settings. The very steady oxidation rate, with which GR is synthesised in the laboratory, is also unexpected in nature, but may not be too far from the truth. Groundwater fluxes are probably responsible for most of the oxygen input and in most environments, the water is homogenous and flows rather slowly, whereby the oxidation level should remain relatively stable. Furthermore, pH in water flowing at steady rate is usually buffered against large fluctuations by its reaction with the host porous media. Local equilibria may contribute to the speeding up or slowing down of the chemical processes. Increasing bacterial growth resulting in more reducing conditions, or falling ground water level causing more oxidising conditions are some examples. The purity of the synthesis environment in the laboratory is probably the source of most of the difference from a natural system. Silica, which is present in most natural environments, effectively decreases the rate

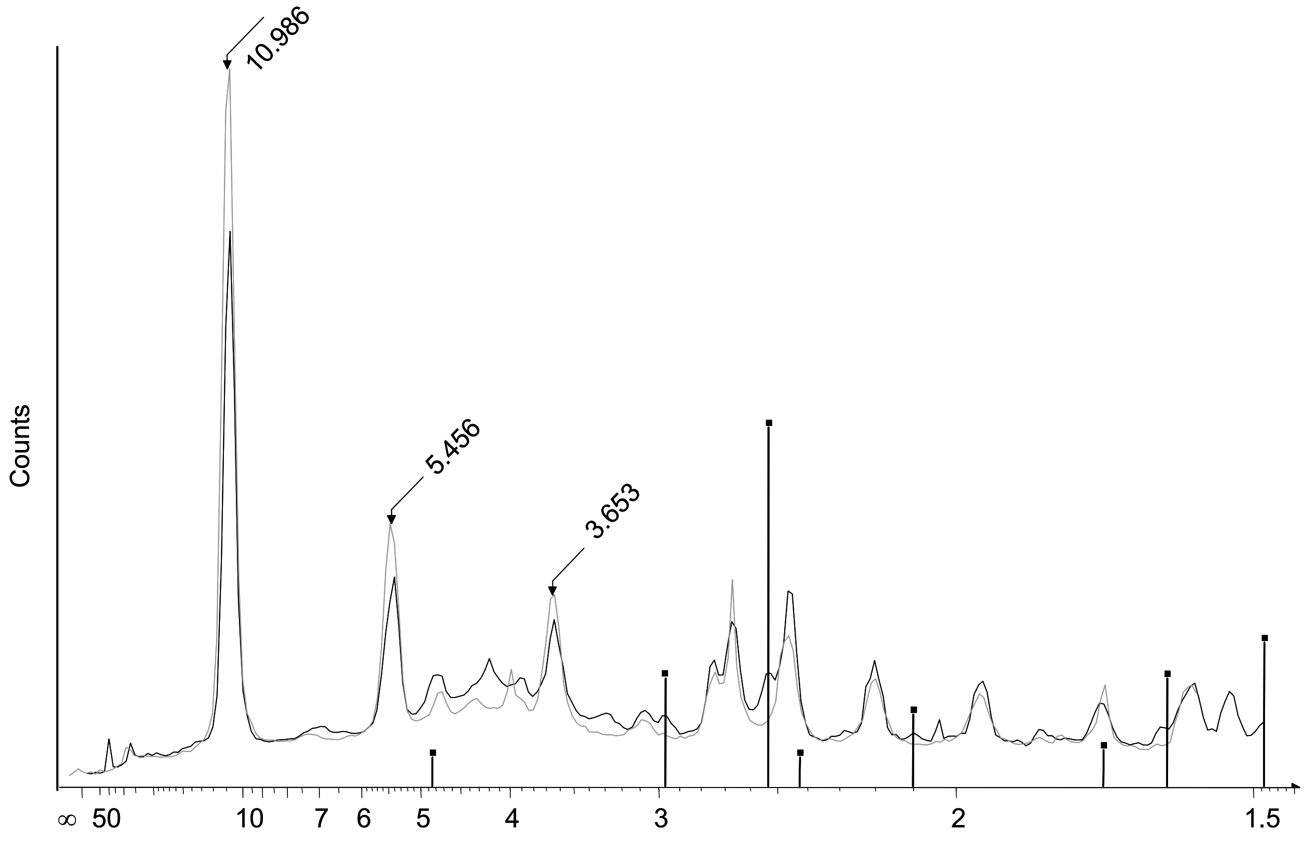

Figure 6.6: XRD traces of a GR_{SO4} batch that was used for TEM investigations. The grey trace was recorded shortly after synthesis and the black trace is a sample from the same suspension, but sampled 48 days later. The bars indicate position and intensity of the peaks of synthetic magnetite. Shortly after synthesis, magnetite was not visible with XRD, only TEM, but after some time, they had grown large and/or numerous enough to be detectable.

of GR oxidation (Hendriksen and Hansen, 2004). The presence of organic matter similarly decreases the rate of GR oxidation as indicated by a small experiment presented later.

6.2 TREATMENT OF GREEN RUST BEFORE REACTION WITH CHROMATE

In all aspects of discussing results obtained from experimental work, the quality of the initial materials must be evaluated. Performing experiments with natural GR is impossible because of severe sampling difficulties, but valuable information can be obtained from simplified systems that can be precisely controlled, such as exist in a reaction vessel in a laboratory. By studying responses to a number of changed parameters, one can gain information about the system, even if these conditions are not representative of natural systems. Determining end products, mechanics controlling the reaction and especially rates of reaction often requires the object of examination to be isolated. In the case of experiments to investigate the behaviour of GR in systems with other compounds, researchers have often chosen to remove all ions, including Fe^{2+}, SO_4^{2-}, CO_3^{2-} or Cl^-, from solution by rinsing the GR with demineralised water. It makes sense, but has the unfortunate side effect that GR is destabilised. Consistent with equilibrium laws, GR starts dissolving and some proportion of the interlayer ions leave the crystals. According to Lewis (1997), GR is unstable in dilute solutions and decomposes to iron oxides or oxyhydroxides even in the absence of other oxidising species. Similar evidence was also observed during my own experiments. A batch of GR_{SO4} was rinsed and left standing in demineralised water in a closed bottle. After a few hours, a continuous flow of small gas bubbles was observed. The reaction was not allowed to proceed, but in a similar incident in our laboratory, GR_{SO4} was left overnight in demineralised water and had transformed to magnetite the next morning (Larsen, 2003). The gas was probably H_2 resulting from deprotonation of water molecules by Fe^{2+} from dissolving GR_{SO4}.

$$2H^+ + 2Fe^{2+} = H_2 + 2Fe^{3+} \qquad \text{Eq. 9}$$

Such bubbles have never been observed in a batch of GR_{SO4} left in its original supernatant. Thus, to avoid instability of GR_{SO4} used for this work, the synthesised material was consequently not rinsed.

When quantifying a reaction, such as determining rate of reaction constants, it is essential to minimise the number of unknowns. The most common parameters to fix are mass, pH and temperature. While there is no obvious problem with a constant temperature, the methods to ensure comparable masses or to keep pH constant may introduce uncertainties. The mass of GR used in reaction experiments is an important variable because it directly controls reactivity through total number of moles of Fe(II) available for reaction and through reactive surface in contact with solution. To determine mass accurately, some researchers freeze-dry the samples to weigh them. Lewis (1997) tested the stability of GR upon freeze-drying. He found that the basal spacing as measured with XRD decreased. GR2 type structures, e.g. GR_{SO4}, experienced a large decrease from about 11 Å to about 8 Å, but a similar increase was observed upon subsequent re-exposure to water. This confirms that structural water is lost when GR is freeze-dried, with resulting decrease of molar mass. This is important to note, when the amount of Fe(II) in re-suspended GR is assessed from the weight of the freeze-dried material.

The pH of the system is another important variable and it is often held in rates of reaction experiments. The stabilisation can be accomplished with a pH-stat but some researchers use organic buffers. Although the behaviour of organic components vary widely, and some buffers may have negligible effect, others might influence the system considerably. The response of GR to one type of organic molecules in the system was tested in a simple experiment (Hansson and Skovbjerg, unpublished). Polysaccharides are common in nature as a result of degradation of organic materials. 20 mM sugar ($C_6H_{12}O_6 \cdot H_2O$) was added to a green rust suspension. After three days, Cr(VI) was added with $Ox_{Cr(VI)/Fe(II)}$ = 82% and the removal of Cr(VI) from solution was monitored. In the experiments presented later where no organics are present, such a chromium concentration would be removed from solution within 5 minutes. With sugar present, 35% remained after 5 minutes and after 30 minutes, 8% was still left in solution. This indicate a much slower rate than in a system without organic material. The presence of organic molecules in the system has an effect, but even though they are present in natural environments, organic components have been excluded in this study in order to understand processes in a controlled system. Adding components too approach a real system is for future studies.

7 GREEN RUST SULPHATE INTERACTION WITH CHROMATE

7.1 RATES OF REACTIONS

Thermodynamical relationships tell us whether a reaction is likely to proceed, but not if it will. It may be kinetically hindered, so rates of reaction are useful for predictions of behaviour in geochemical systems. When a rate of reaction is determined experimentally, it may be applied to a natural system such as contaminated groundwater. Soluble compounds are likely to flow with the water unless they are retarded by surface complexation on minerals and organic compounds or reduced to less soluble phases. Knowing rates of reaction makes it possible to evaluate whether there is enough time for a reaction to take place when a contamination plume migrates and it may be possible to use the information to evaluate the time span over which contamination will influence the environment. Although it was not the purpose of these experiments to precisely determine reaction rates, some general observations can be made from the results, which are interesting when compared to previously published work.

7.1.1 General observations

There are two main contributing factors to the rate of Cr(VI) reduction: the Fe(II) in the green rust and the Fe(II) dissolved in solution.In these experiments, where the supernatant is not removed, in order to keep the solid phase stable and at equilibrium, there is potential for reduction capacity in the supernatant. Dissolved $Fe^{2+}_{(aq)}$, up to 400 ppm, could potentially reduce all Cr(VI) for the lowest concentration experiments and about 30% in the medium concentration (Appendix A). However, this did not happen and previous research has found the same. Williams and Scherer (2001) compared their obtained reduction rate by GR_{CO3} to the reduction rate by aqueous Fe^{2+} alone (Buerge and Hug, 1997) and determined that reduction by GR_{CO3} was about 10 times faster. In the low Cr(VI) experiments described here, changes in GR morphology were visible by AFM, proving the Fe(II) in the solid was reactive. Based on the results of Williams and Scherer (2001) and these AFM observations, the role of dissolved Fe^{2+} reduction was assumed negligible for the purpose of this project. An experiments to quantify the effect of dissolved Fe^{2+} is planned during the preparation of this work for publication.

In experiments with Cr(VI) concentrations ranging from low (*L*) to very high (*VH*), supernatants were sampled during reaction for aqueous Cr(VI) concentration. For all solutions except *VH*, which contains a concentration of Cr(VI) well above the reduction capacity of the GR_{SO4} present, no chromium could be detected in solution after only 5 minutes, proving a very fast reaction. A sample from suspension *VH* was collected on a filter 24 hours after addition of Cr(IV) and dissolved to determine the Cr(VI) and Cr(III) concentrations in the solid. The solid contained 0.11% Cr(VI) and 17.24% Cr(III) by mass so only about 0.6% of the Cr was Cr(VI). This portion may have been adsorbed to the surface because of the relatively high concentration of about 90 ppm Cr(VI) in solution (Appendix B). This is consistent with XPS results from Loyaux-Lawniczak et al. (1999), showing that in a reaction with $Ox_{Cr(VI)/Fe(II)}$ = 100%, more than 95% Cr in the end product was present as Cr(III).

7.1.2 Published Rates of Reaction

Several researchers have investigated the rates of reaction between chromate and various GR forms. The focus has primarily been on GR_{CO3}, though a single publication compares the experimental rates of reaction of GR_{CO3}, GR_{Cl} and GR_{SO4}.

Williams and Scherer (2000, 2001) investigated the reduction of Cr(VI) by GR_{CO3}. They found that the rate of reaction was proportional to green rust surface area. At low Cr(VI) concentrations, the reaction followed a first-order rate expression, consistent with green rust surface area being in excess, but at high concentrations, the reaction shifted to a second order rate expression. This suggests that available Fe(II) is limited either because of a finite number of sites or because a precipitate has blocked the sites. A pseudo-first-order model was chosen to describe the overall reaction:

$$\frac{\mathrm{d}}{\mathrm{d}t}[\mathrm{Cr(VI)}] = -k_{obs}[\mathrm{Cr(VI)}_{\mathrm{soln}}], \qquad \text{Eq. 10}$$

where $[\mathrm{Cr(VI)}_{\mathrm{soln}}]$ is the concentration of dissolved Cr(VI) and k_{obs} is the first-order rate coefficient. At pH 7, k_{obs} was $3.3 \times 10^{-3} \pm 0.7 \times 10^{-3}$ s^{-1}. Before reaction, the carbonate GR was rinsed, freeze-dried and resuspended in demineralised water, all of which may have destabilised the GR structure, reduced interlayer exchangeability and/or caused formation of magnetite. Varying pH had little influence on the reaction rate, resulting in an approximate 5-fold decrease with a pH increase from pH 5 to 9.

Bond and Fendorf (2003) investigated and compared the reaction rates of several GR compounds and found that reactions between GR and Cr(VI) could be expressed with respect to both variables, i.e. GR type and Cr(VI), using pseudo-first order rate expressions. The overall second order rate expression with the solution density of GR, {GR}, expressed in g/L was:

$$\frac{\mathrm{d}}{\mathrm{d}t}[\mathrm{Cr(VI)}] = -k[\mathrm{Cr(VI)}]\{\mathrm{GR}\}, \qquad \text{Eq. 11}$$

where k represents a rate constant based on modelled pseudo-first order rate coefficients (k_{obs}). For the chloride, carbonate and sulfate forms of GR, k was: 5.28×10^{-2}, 3.34×10^{-2} and 1.95×10^{-2} $\mathrm{Lg^{-1}s^{-1}}$, respectively, for {GR} ranging from 0.125 to 0.5 g/L. Bond and Fendorf (2003) found that only about half of the Cr(VI) in a suspension with $\mathrm{Ox_{Cr(VI)/Fe(II)}}$ = 91% was removed from solution after 25 minutes, compared to less than five minutes needed to reduce about the same concentration in the present work. So, their model does not fit the data obtained in this work. The reason for this may be the experimental set up, which affects the rate of reaction. The GR samples used by Bond and Fendorf (2003) were rinsed with demineralised anoxic water and dried before re-suspended in demineralised water, a treatment, which could destabilise the structure by flushing out interlayer anions. The water for re-suspension contained 5 mM MOPS buffer, which is an organic compound with the formula: $C_7H_{15}NO_4S$. The simple experiment with sugar in the system decreased the reaction rate significantly between Cr(VI) and $\mathrm{GR_{SO4}}$. Although this organic buffer, which is an amino acid, has a different structure and composition, it is possible that it could also have influenced the reactivity of GR. An experiment to test this hypothesis was not presented. However, in one of their experiments, the authors used the same concentration of Cr(VI) to $\mathrm{GR_{CO3}}$ as Williams and Scherer (2001) and in spite of the organic buffer, the reduction rates of $\mathrm{GR_{CO3}}$ corresponded reasonably well. Thus one can conclude that the difference between the rates presented in those studies and this work is a result of rinsing, drying and resuspending the powder.

Bond and Fendorf (2003) wanted to compare the reduction rates between $\mathrm{GR_{Cl}}$, $\mathrm{GR_{CO3}}$ and $\mathrm{GR_{SO4}}$, but the way they added GR gives misleading results. The authors argue that in natural settings, systems equilibrate to mass, so to a solution of a given concentration of Cr(VI), they add the same mass, e.g. 0.25 g $\mathrm{GR_{Cl}}$, 0.25 g $\mathrm{GR_{CO3}}$ or 0.25 g $\mathrm{GR_{SO4}}$, all filtered and dried in a glove box.

Table 7.1: Bond and Fendorf (2003) compared the reaction rates between Cr(VI) and three types of GR based on their weight. However, that procedure does not give comparable results because the various types of GR contain a different amount of reactive Fe(II) per mass unit. This table illustrates the equivalent masses, normalised to 0.25 g GR_{CO3}, if they were based on Fe(II) content. Apparently, much more GR_{SO4}, which supposedly had the slowest reduction rate, should have been added for the amounts to be comparable.

	Assumed formula (References in Table 4.5)	Molar mass (g/mol)	Actual mass used (Bond and Fendorf, 2003) (g)	Moles of reactive Fe(II) in 0.25 g GR (μmol)	Mass based on reactive Fe(II)* (g)
GR_{Cl}	$Fe^{II}_3Fe^{III}(OH)_8Cl \cdot 2H_2O$	430.93	0.25	580	0.23
GR_{CO3}	$Fe^{II}_4Fe^{III}_2(OH)_{12}CO_3 \cdot 2H_2O$	635.23	0.25	394	0.25
GR_{SO4}	$Fe^{II}_4Fe^{III}_2(OH)_{12}SO_4 \cdot 8H_2O$	779.4	0.25	321	0.30

***Mass based on reactive Fe(II) is normalised to GR_{CO3} by comparing the amount of Fe(II) per g GR. The calculation is shown with GR_{Cl} as example: 1 g GR_{Cl} / 430.93 $gmol^{-1}$ GR_{Cl} * 3 mol Fe(II)/mol GR_{Cl} = 6.7 mmol Fe(II). GR_{CO3}(Fe(II)) = 6.3 mmol, GR_{SO4}(Fe(II)) = 5.1 mmol, GR_{CO3}-normalised: GR_{Cl}(FeII): (6.3-6.7)/6.3*0.25 g +0.25 g = 0.23 g.**

However, a system equilibrates to available Fe and the redox level of the system, rather than the arbitrary mass of an Fe-bearing mineral. Thus, they should have added the different GR types in quantities containing the same amount of active Fe(II). Table 7.1 gives GR_{CO3}-normalised quantities of the three GR types with values that would give the same amount of Fe(II). The percent difference between the moles of Fe(II) present in the 0.25 g of GR_{Cl} and GR_{SO4}, for example, is (580-321)/((580+321)/2) ×100% = 57%, which must have an influence on the observed reaction rates.

Legrand et al. (2004a) investigated the rate of reduction of aqueous chromate by GR_{CO3} in experiments with pH of 9.3 to 9.6, consistent with values measured in zero-valent iron PRBs. Neither of the models suggested by Williams and Scherer (2001) or Bond and Fendorf (2003) fits their data so they discard them! Instead they suggest that the redox reaction is heterogeneous with a concomitant precipitation of Cr(III) monolayers on the surface of the reacting GR, but provide no evidence for such a layer other than the fit of the data to their model. They assume uniform and homogenous layers and construct a model where successive monolayers of Cr(III) precipitate and chromate concentration simultaneously decreases:

$$\frac{d(\mathrm{Cr(VI)})}{dt} = -\sum_{1}^{j} k_i^{\{S\}}[\mathrm{Cr(VI)}](\{n_{i-1}\} - \{n_i\}), \qquad \text{Eq. 12}$$

where $k_i^{\{S\}}$ ($s^{-1}Lm^{-2}$) represents the rate coefficient of formation of a Cr(III) monolayer, *i*, and $\{n_i\}$ (mol/L) represents the molar concentration of Cr(III) precipitated in monolayer *i*. They derived the following rate coefficients for 1, 2 and 3 monolayers: $k_1^{\{S\}} = 5 - 8\times10^{-4}$, $k_2^{\{S\}} = 0.5 - 3\times10^{-5}$ and $k_3^{\{S\}} = 1.7\times10^{-6}$. The observed rate of reaction decreases as successive monolayers build. In fact, the rate decreases so much that about 16 hours is needed to reduce 111 μmol of Cr(VI) in the presence of 500 μmol of Fe in GR_{CO3} i.e. $Ox_{Cr(VI)/Fe(II)}$ = 100%. Neither Williams and Scherer (2001) nor Bond and Fendorf (2003) present data showing the concentration of Cr(VI) after 40 to 50 minutes reaction time and they do not state at what time Cr(VI) concentration is below detection. A comparison of their data with the extensive reduction time obtained by Legrand et al. (2004a) is therefore not possible. Compared to the data from this work, where a high concentration, $Ox_{Cr(VI)/Fe(II)}$ = 91%, is reduced within 5 minutes by GR_{SO4}, 16 hours is a very long time. However, Legrand et al. (2004a) used GR_{CO3} whereas this study used GR_{SO4}, so our data are not comparable directly.

Legrand et al. (2004) explain their relatively long reduction time with the accumulation of Cr surface layers, but other mechanisms would also lead to extended reaction times. The presence of magnetite is one. Legrand et al. (2004a) have not presented any analytical results, for example transmission Mössbauer spectroscopy (TMS) or high-resolution microscopy data, that prove or disprove the presence of magnetite. XRD revealed no magnetite but, as was the case in the present work, the crystals could have been too small to diffract the X-rays. Several conditions in the experimental set-up favour formation of magnetite. i) The Fe^{2+} concentration of their solution is at all times low, with an initial concentration of 0.01 M Fe^{2+} compared to 0.05 M Fe^{2+} used in GR_{SO4} synthesis for the present work. They stop the synthesis when a sharp increase in Eh occurs and an analysis of the supernatant does not give any detection of iron species. The depletion of Fe^{2+} in solution may cause the GR to destabilise (Lewis, 1997), which then releases Fe(II) and Fe(III) to solution. Because these species are not detected, it is possible that another equilibrium system is controlling the concentration of Fe^{2+}, indicating formation of another Fe(II), Fe(III)-solid, e.g. magnetite. iii) The synthesis oxidation rate is fast. Only 25 ± 2 min was needed to reach the Eh increase. A fast synthesis rate was probably the cause of magnetite formation in the present work. It is known that the Cr(VI) reduction by magnetite is relatively slow. White and Peterson (1996) showed that more than 25 hours was needed to reduce 0.15 mM Cr(VI) in the presence of 60 g/L magnetite. The magnetite used for their experiments had an Fe(III)/Fe(II) ratio of 2.05, so for the initial Cr(VI) concentration, $Ox_{Cr(VI)-Fe(II)}$ was about 0.2%. The presence of a large amount of magnetite in the suspension of Legrand et al. (2004a) could have slowed the reduction of Cr(VI).

Legrand et al. (2004a) present Fourier Transform Infrared Spectroscopy (FTIR) on the pure GR and intermediate solid products. FTIR uses transmitted light to reveal chemical bonding environments. The specimen absorbs light of specific wavelengths according to its bonding and the wavelengths that pass the specimen are recorded as a spectrum. The technique can be used on pellets of dried sample. The FTIR spectra presented by Legrand et al. (2004a) are not clearly explained; i.e. none of the bands are named and spectra of wavenumbers below 490 are not shown for reasons unmentioned. One cannot determine from the text or the figure whether the presence of magnetite can be excluded. According to Ishikawa et al. (1998), magnetite is difficult to distinguish with FTIR when mixed with α-, β- or γ-FeOOH, which is expected in an oxidised sample of GR. Comprehending FTIR is not within the scope of this thesis. However, if these phases are difficult to distinguish, it is probably also difficult to distinguish magnetite from GR.

7.1.3 Conclusions About Rates of Reaction

Table 7.2summarises the published results on Cr(VI) reduction rate by GR and reveals some inconsistency, especially regarding GR_{CO3}. Comparing the three models presented on Cr(VI) reduction by GR_{CO3}, the Legrand et al. (2004a) fits the experimental data most closely, but the proposed mechanism is not supported with evidence. The models proposed by Williams and Scherer (2001) and Bond and Fendorf (2003) do not approximate the experimental data as well. It is clear on Figure 7.1, reproduced from Williams and Scherer (2001) and Figure 7.2, reproduced from Bond and Fendorf (2003), that when the initial Cr(VI) concentration is high, $Ox_{Cr(VI)/Fe(II)}$ = 91% and 73%, the models predict lower Cr(VI) concentrations than are actually measured after only 15 minutes. The discrepancy between the models and the experimental data increases with reaction time. In contrast, the model proposed by Legrand et al. (2004a) fits the data very well from the initial very high concentration, $Ox_{Cr(VI)/Fe(II)}$ = 100%, until the concentration of Cr(VI) is below detection after more than 16 hours (Figure 7.3).

Table 7.2: Reduction rates obtained in the literature and rate of reaction data from this work. At low Cr(VI) concentrations, the rates are comparable, but at high concentrations ($Ox_{Cr(VI)/Fe(II)}$ = 100%), the values reported are inconsistent.

Reduction rate	GR_{SO4}		GR_{CO3}		GR_{Cl}	
Ratios Authors	$Ox_{Cr(VI)/Fe(II)}$ ~ 40%	$Ox_{Cr(VI)/Fe(II)}$ ~ 80%	$Ox_{Cr(VI)/Fe(II)}$ ~ 50%	$Ox_{Cr(VI)/Fe(II)}$ ~ 100%	$Ox_{Cr(VI)/Fe(II)}$ ~ 50%	$Ox_{Cr(VI)/Fe(II)}$ ~ 100
This work	< 5 min	< 5 min				
Williams and Scherer (2001)			> 20 min	>> 25 min		
Bond and Fendorf (2003)	~ 20 min	>> 25 min	10 – 25 min	>> 25 min	15 - 25 min	>> 25 min
Legrand et al. (2004)			~ 20 min	~1000 min		

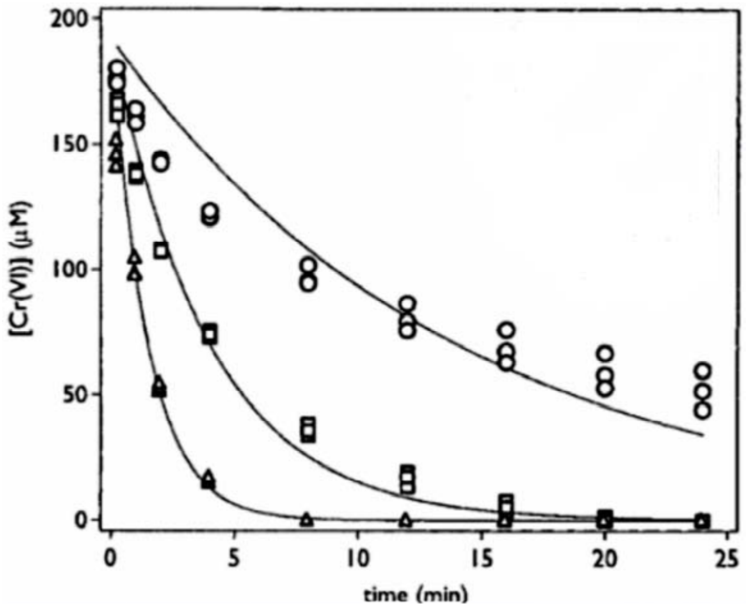

Figure 7.1: Reduction of Cr(VI) with GR_{CO3} during 25 minutes, obtained by Williams and Scherer (2001). Surface area {GR} was used as a measure for the concentration of GR. Average specific surface area of dried and evacuated material was 47 ± 7 m^2/g. The symbols represent: (○) 5.9, (□) 11.8, (Δ) 23.5 m^2/L, while the solid lines represent a first-order rate of reaction model. The authors used an initial Cr(VI) concentration of 192 μM corresponding to $Ox_{Cr(VI)/Fe(II)}$ about 73% (○), 37% (□) and 18% (Δ) for GR_{CO3}. The model approximates the data reasonably well with low C(VI) concentrations, but fails at high concentration (from Williams and Scherer, 2001).

Bond and Fendorf (2003) have presented the only model of Cr(VI) reduction by GR_{SO4}, but this model does not fit the reduction rates obtained in preliminary rate of reaction experiments in this work because the reduction rates proposed are much too slow. It should be noted that Bond and Fendorf (2003) tried to fit the same model to Cr(VI) reduction by GR_{SO4}, GR_{CO3} and GR_{Cl}. However, it is unlikely that the same reaction mechanism applies to GR types of such different interlayer anions. In fact, reduction of a high concentration of Cr(VI) by GR_{SO4} within 5 minutes in this work, compared to the initially fast, then progressively slower reduction rate of up to 16 hours obtained by Legrand et al. (2004) for GR_{CO3}, is clear evidence that some difference exist in the two systems. It may be that two different mechanisms are controlling the reactions. Thus, different models are needed to describe the rates of reaction for each GR type.

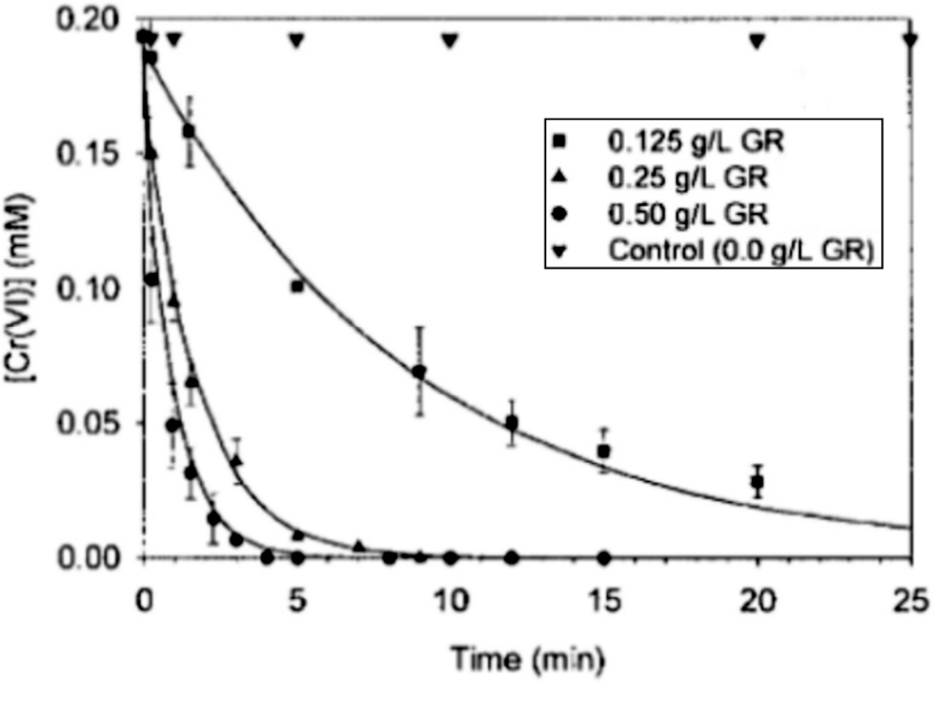

Figure 7.2: Cr(VI) reduction with GR_{CO3} at various suspension densities during 25 minutes as obtained by Bond and Fendorf (2003). Solid lines and symbols represent first-order rate of reaction models and actual data, respectively. Initial Cr(VI) concentration was 192 μM, so assuming stoichiometric GR_{CO3}, 0.125, 0.25 and 0.5 g/L GR corresponds to $Ox_{Cr(VI)/Fe(II)}$ = 73, 37 and 18% for GR_{CO3} The model fits the data when $Ox_{Cr(VI)/Fe(II)} \leq 37\%$, but predicts too high rates when Cr(VI) concentration is high (from Bond and Fendorf, 2003).

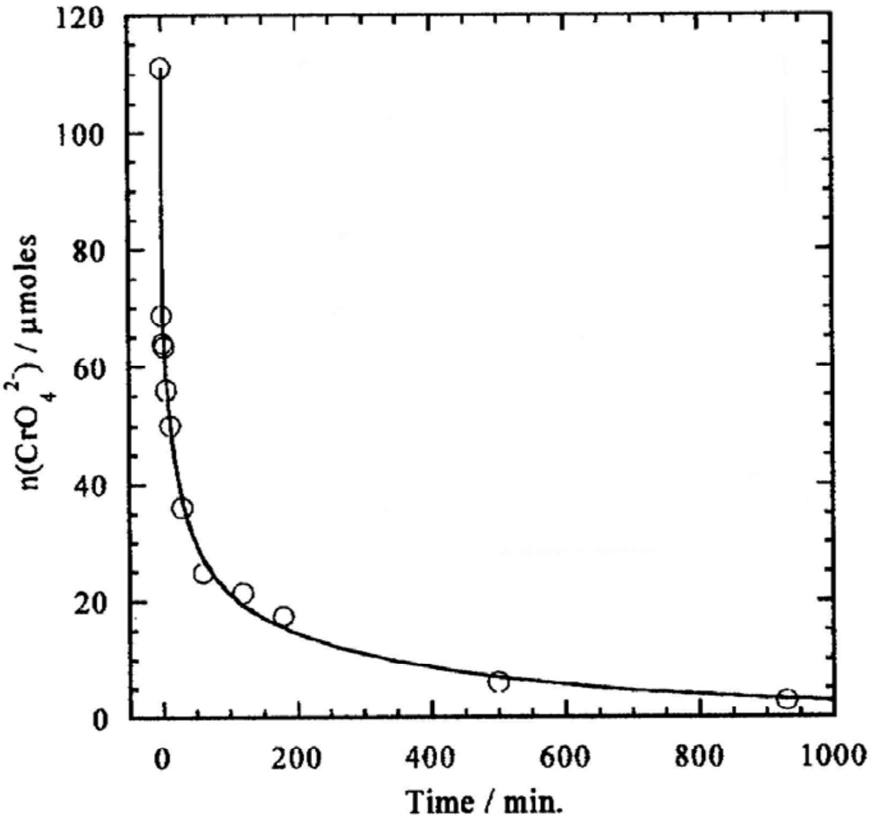

Figure 7.3: Reduction rate of Cr(VI) with GR_{CO3} during 16.6 hours obtained by Legrand et al. (2004a). The symbols represent data from an experiment with 500 µm Fe in GR_{CO3} and 111 µm Cr(VI), corresponding to $Ox_{Cr(VI)/Fe(II)}$ = 100%. The solid line represents the rate of reaction model. The model fits the data very well from the initial high concentration until Cr(VI) is below detection level. (modified from Legrand et al., 2004).

7.2 END PRODUCT

Characterisation of the end product of the reaction between GR and chromate is important. The end product gives information about the oxidation/transformation mechanisms and tells about the stability of the Cr as geochemical conditions in a natural system evolve. Trivalent chromium resulting from reduction of chromate is sparingly soluble, so it is most likely associated with the solid end product. Therefore it is essential to determine whether Cr(III) is incorporated into the structure of the end product and whether this phase is stable in natural environments. The question of end product has already been addressed in a number of publications, but the results presented in them are only partly supported by the results obtained in this work.

7.2.1 End Product Obtained in This Work

One of the objectives of this study was to observe the undisturbed evolution of the suspensions over time. This was accomplished by extracting solid material from aging samples at time intervals of up to 10 days after addition of chromate to GR_{SO4}. Two sets of suspensions, that were different because of different synthesis conditions, were exposed to chromate: 1) One set consisted of pure GR_{SO4}, where the solid material was characterised with XRD and AFM and the supernatant was analysed for chromium concentration. These were oxidised slowly (0.8 mL/min base added to balance Fe(II) oxidation); 2) another set consisted of GR_{SO4} and magnetite and the solid material was investigated with XRD, TEM and AFM. Chromium was added in similar concentrations but the evolution of the aqueous concentrations could not be determined for that set of experiments. Different, but consistent, results were obtained with the two sets.

7.2.1.1 Zoning of GR and Formation of an Amorphous Solid

The transformation of GR_{SO4} from a ferrous-ferric compound to a ferric compound, as a result of oxidation by Cr(VI), begins with the partitioning of the crystal into reaction zones. On BF-TEM and HAADF-STEM images of solids from high concentration suspension (*H*) from t = 10 minutes ($H_{10\,min}$), the GR is still hexagonal and all crystals appear similar (Figure 7.4). In a traverse from edge to centre, there is a dark area, “the edge”, a narrow light area, “the rim” and a large, homogenous, medium grey area, “the core”. BF-TEM images (Figure 7.4a) show Bragg diffraction contrast. However, SAED performed on crystals from the medium Cr concentration suspension, $M_{10\,min}$, that appeared similar to the crystals from suspension $H_{10\,min}$ (Figure 7.5), revealed no structural difference between the areas so it is interpreted that the lattice is only slightly disturbed at the edges and rims relative to the cores. The HAADF-STEM image (Figure 7.4b) shows that the areas differ in atomic mass, thickness and/or atomic density. From AFM images, it is evident that the three areas have different thicknesses (Figure 7.6). From the outside in, there is a tall edge, then a depression and innermost is a core slightly thinner than the edge. This corresponds very well to the dark, light and medium grey colours on the HAADF-STEM image. The Cr/Cr+Fe content of the

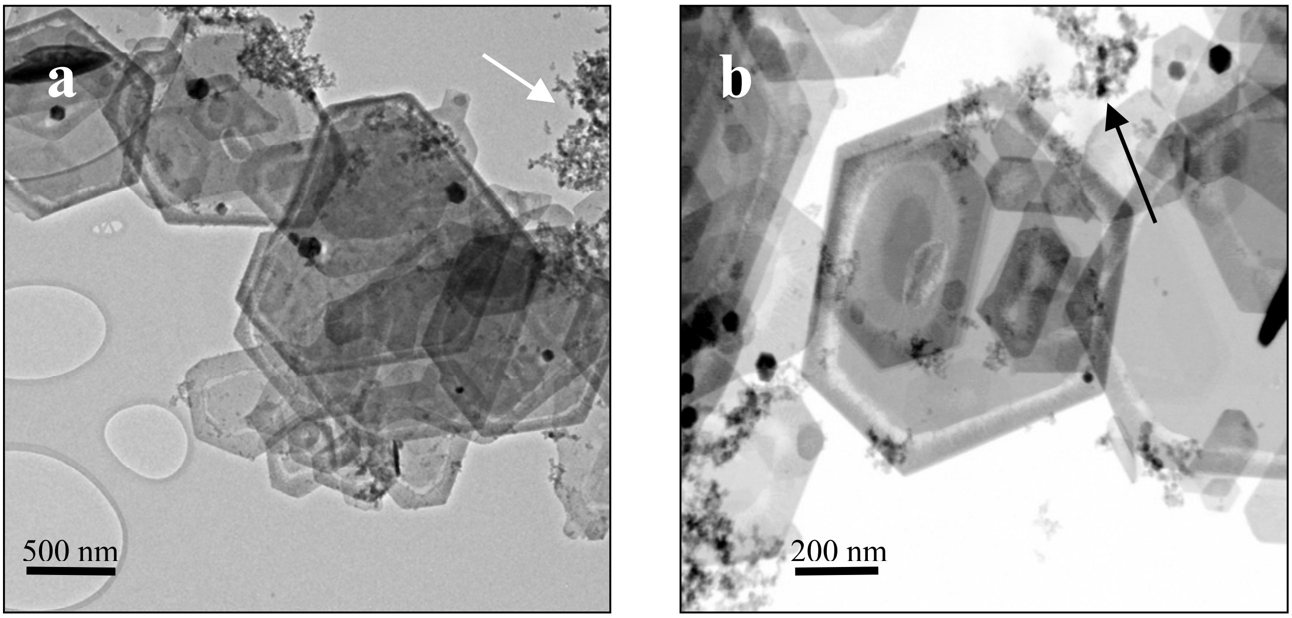

Figure 7.4: Images of GR_{SO4} that has reacted with high Cr concentration where $Ox_{Cr(VI)/Fe(II)}$ = 88% for 10 minutes. Oxidation edges are seen on the crystals and a very fine-grained amorphous solid (black and white arrows) has precipitated. a) BF-TEM, b) HAADF-STEM with reversed grey-scale.

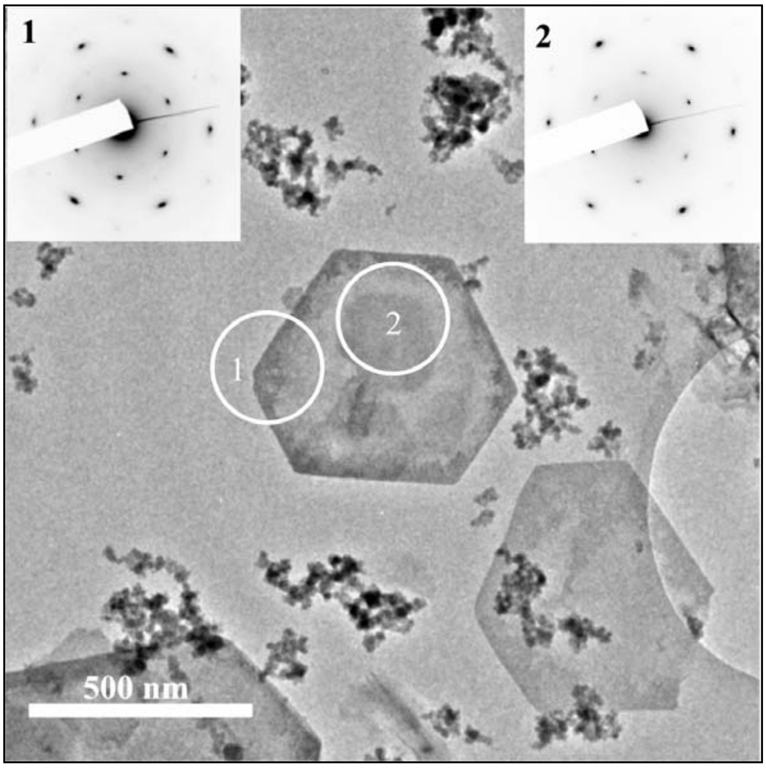

Figure 7.5: GR_{SO4} after reaction in suspension *H* for 10 minutes. SAED patterns (insets) were obtained for both area 1, at an oxidation edge and area 2, at the core. There is no significant difference in the two patterns, meaning the crystal structures are similar.

edges were on average ~ 9% with a spread from 7.7 to 10.2% for samples from suspension $H_{10\,min}$. The measurements in the rim and core usually had total counts too low for the exact percentages to be trusted, but the Cr/Cr+Fe in the rims appeared consistently higher than in the edges, whereas the cores gave similar percentages as in the edges. Thus, one can conclude that the three areas of early-reacted GR differ in structure, thickness and Cr content.

Simultaneously with the zoning of the GR crystals, a very fine-grained Cr-Fe solid precipitates. It appears as an increased broad background on XRD patterns. In TEM, it looks non-crystalline, sort of mushy (Figure 7.7) and it produces a diffuse halo in SAED, which means it is amorphous. With semi-quantitative XEDS analysis, the average Cr/Cr+Fe ratio of this material was found to be ~25% with a spread from 24.4 to 26.2% in suspension $M_{10\,min}$. One measurement gave ~37%, in suspension $H_{10\,min}$, so there was substantially more Cr in the amorphous solid in both samples than associated with the GR crystals. There is an even distribution of Cr and Fe in the amorphous solid as can be seen with XEDS mapping (Figure 7.8).

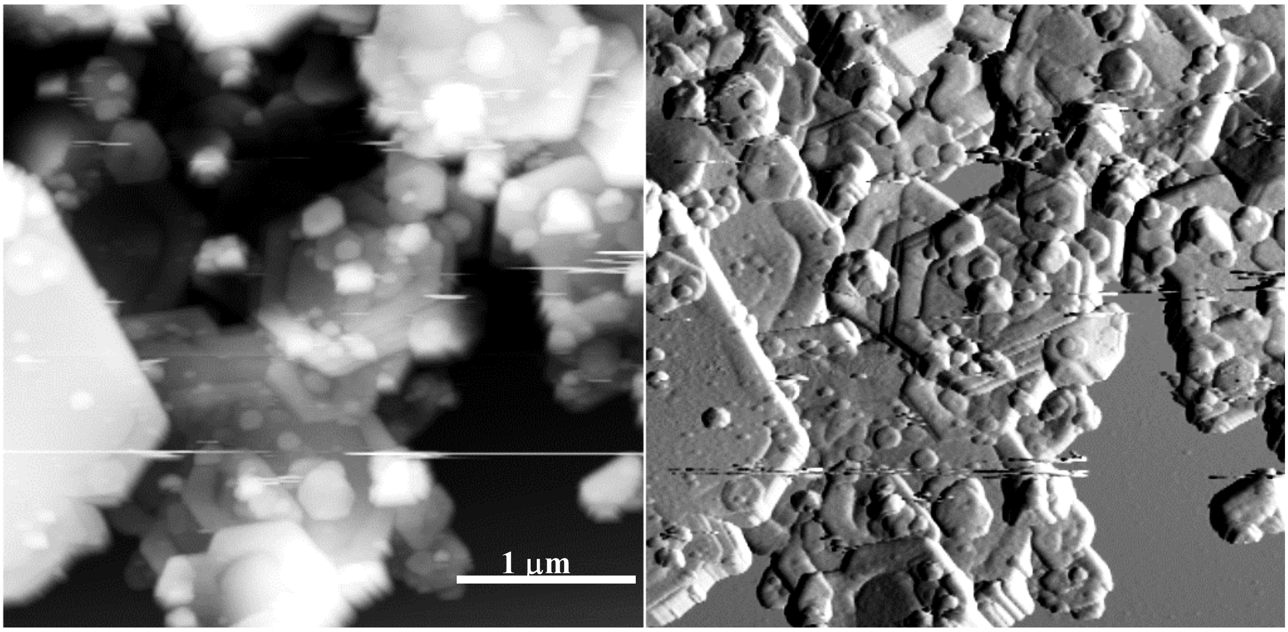

Figure 7.6: AFM height (left) and deflection (right) images of GR_{SO4} that has reacted with Cr(VI). After only 10 minutes in a suspension *H*, grooves have formed along the borders, leaving thick edges and slightly thinner cores. The area of the groove was destabilised and dissolved. The streaks on the images are artefacts from loose material dragged by the tip.

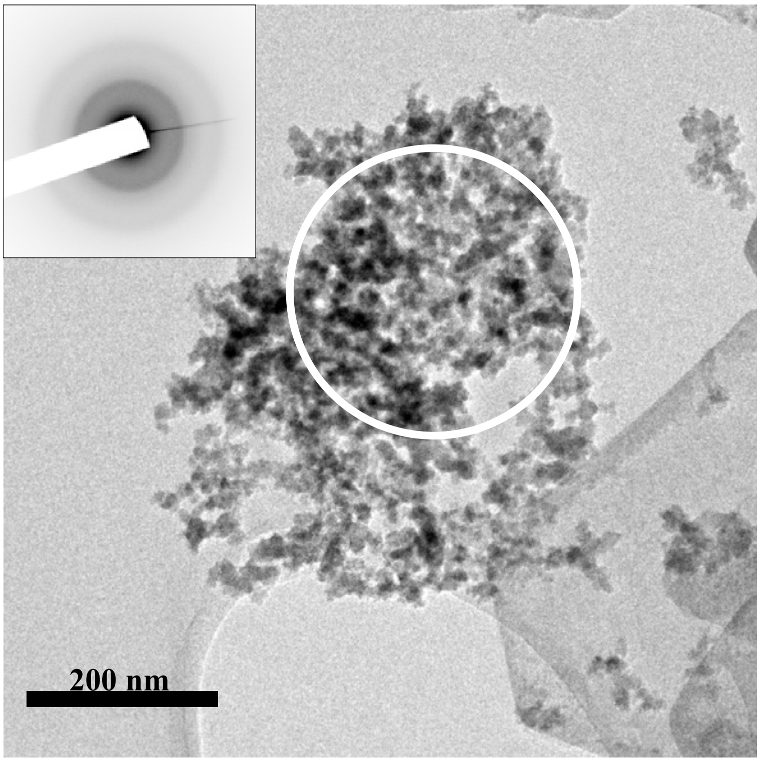

Figure 7.7: BF-TEM image of the amorphous Cr-Fe solid. The inset is an SAED diffraction pattern obtained within the white circle. The diffuse halo shows that the solid is amorphous with 2 “lines”. Another similar area, analysed with very low electron dose, produced the same pattern, so it was not the electron beam that caused amorphisation of the compound.

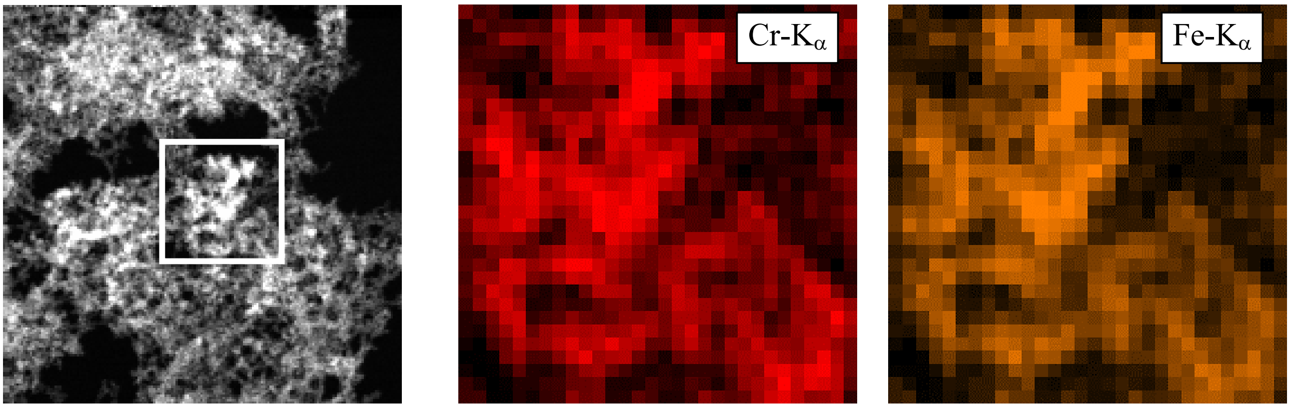

Figure 7.8: XEDS map of amorphous particles. The compound is homogenous with respect to Cr and Fe distribution, suggesting that the Cr and Fe co-precipitated. The box sizes are about 60 nm^2.

7.2.1.2 Transformation from GR_{SO4} to goethite

When the initial GR suspension is left to equilibrate after addition of Cr(VI), a new phase evolves. This phase is unquestionably identified as goethite by XRD (Figure 7.9, grey trace). The goethite structure evolves gradually as shown on XRD patterns from suspension *H* (Figure 7.10). After five days, all GR_{SO4} peaks have disappeared and goethite is the only major crystalline phase detectable with XRD. In TEM, the crystals have dramatically changed their appearance after 20 hours (Figure 7.11). Crystals grow in from the edges of "GR morphs": A GR morph is defined as a particle of different structure and chemical composition than GR_{SO4}, but with the outer morphology of the GR_{SO4} crystal remaining intact. Because the end product was shown to be goethite, a search to define which particles are goethite and which might still be GR_{SO4} in suspensions of lower

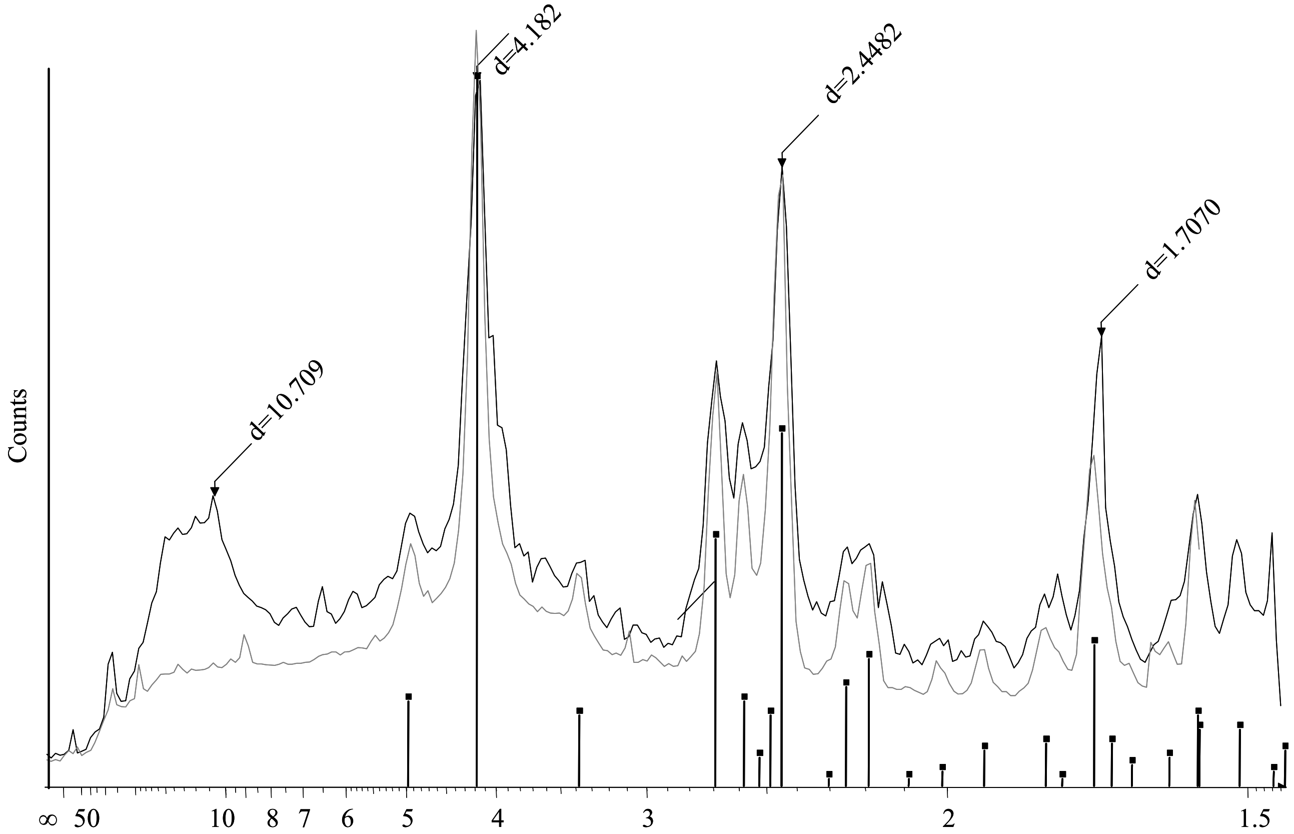

Figure 7.9: CT-XRD traces of Cr-goethite (black) and goethite (grey) obtained from the aerial oxidation of GR_{SO4}. The black bars indicate the peaks of synthetic goethite. The traces are identical except for the broad bump d = 10-30 Å. The phase responsible for this broad peak has not been identified, but it is possibly a relic from GR_{SO4}.

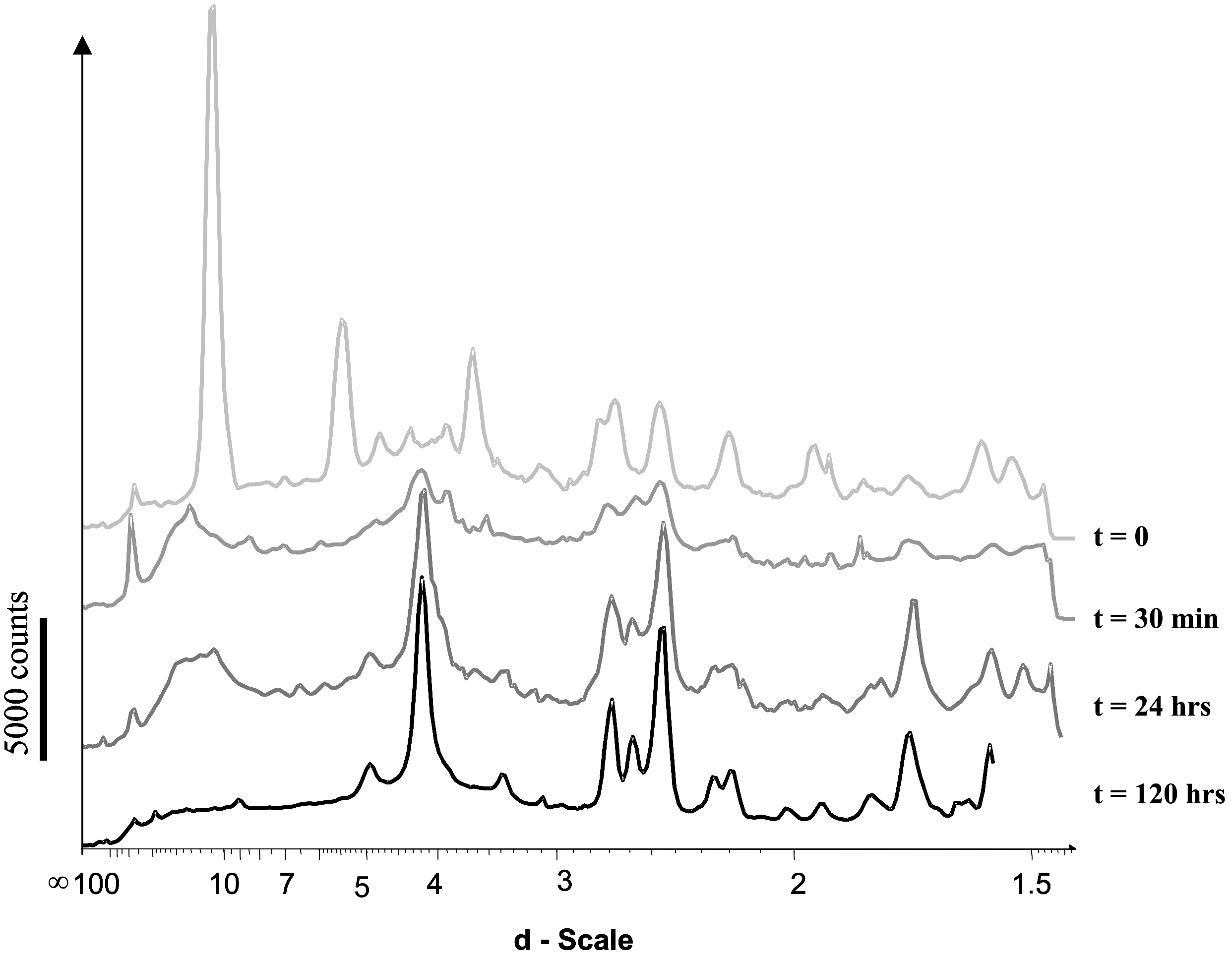

Figure 7.10: XRD traces showing the evolution of GR_{SO4} and chromate suspensions from pure GR (top) to almost pure goethite (bottom). From 1 to 5 days, the peaks narrow, indicating an increase in grain-size and/or crystallinity as a result of aging. The broad peak at about d =11 to 20 has diminished into the background after 5 days.

Cr(VI) concentration seems logical. SAED can distinguish between solid phases. However, the GR structure along the *c*-crystallographic axis is almost exactly the same as the goethite structure along the *a*-axis. The SAED pattern for both is hexagonal and they have the same dimensions, meaning an SAED pattern from GR_{SO4} matches goethite just as well. The crystallographic similarities between the phases may mean that if the water molecules and interlayer ions are removed from an oxidised GR_{SO4} structure, it collapses to produce a goethite structure. produce a goethite structure. As a consequence, goethite may very well transform topotactically from GR_{SO4} without leaving traces in the SAED patterns.

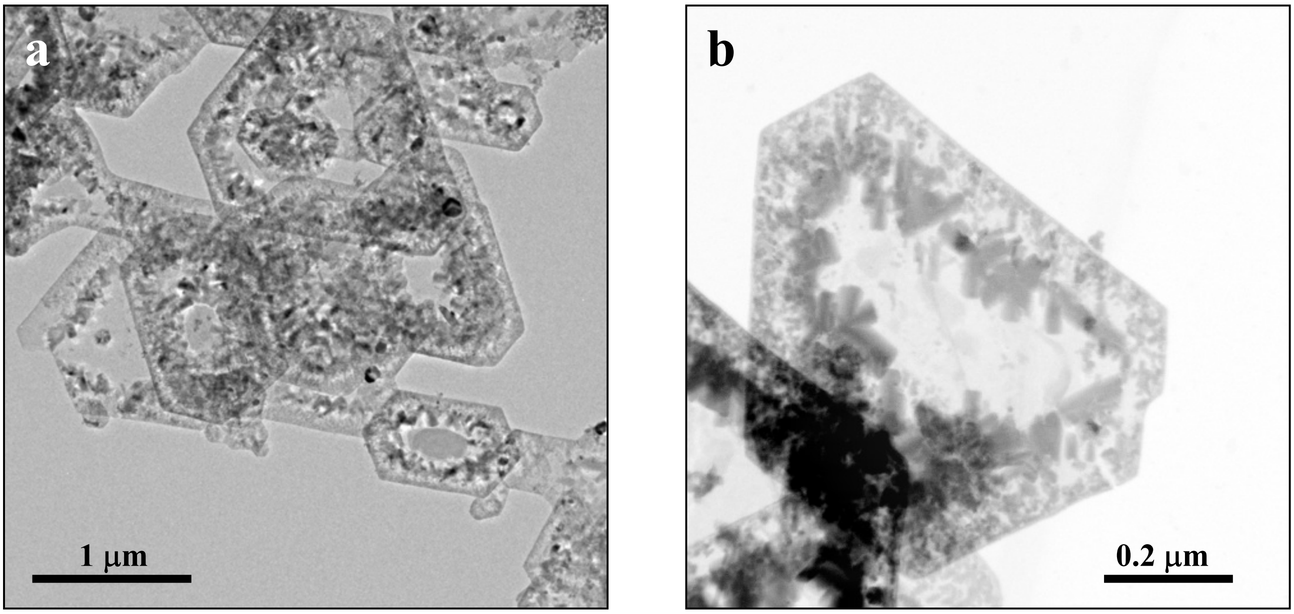

Figure 7.11: GR_{SO4} from suspension *H* after: a) 20 hours and b) 6 days. The cores of the crystals are very thin and goethite crystals grow from the edges toward the core. a) BF-TEM, b) HAADF-STEM with reverse grey-scale.

The crystals growing inside the GR morphs produce SAED patterns that match both goethite and GR_{SO4}. However, because the crystals observed in the morphs are elongated and formed as a result of oxidation of GR_{SO4}, the patterns of that material are interpreted to represent goethite. The SAED patterns of this material have an additional set of spots compared to the SAED patterns observed before Cr was added (Figure 7.12). The new spots are situated exactly midway between the original spots. This feature, which is termed double-spacing, is well-known in low-energy electron diffraction (LEED), SAED and AFM and reveals the presence of a superstructure. This means that the unit cell is doubled. On a surface, it can result from relaxation in the top two or three layers of a solid (Henriksen et al., 2002). In bulk material, it arises when another element is incorporated in an ordered pattern. SAED averages over the whole thickness of the analysis area, so in the present case, it could very well be Cr(III) substituting for Fe(III). Cr/(Cr+Fe) ratios were determined by XEDS to range from 5 to 9% depending on initial Cr(VI) concentration. Bracewellite, α-CrOOH, is isostructural with goethite and because Fe(III) and Cr(III) have similar ionic characters and about the same ionic radius (0.615 Å and 0.645 Å when their coordination number is 6; Shannon, 1976), solid solution is expected between these two compounds. Thus, no significant rearrangement of the atomic structure is needed to accommodate Cr(III) in the α-FeOOH crystal lattice. Schwertmann et al. (1989) proposed Cr/Fe solid solution, proved the incorporation of Cr(III) and synthesised goethite with up to 10 mol% Cr. Consequently, the crystals growing in GR morphs are interpreted to be Cr-substituted goethite.

When zooming in with HR-TEM on the GR_{SO4} transforming to GR morphs, there are areas where every other atomic row appears raised above the next (Figure 7.13). This gives rise to double-spacing, which is observed in the goethite crystals growing into the core areas, but also in the edges of the GR morphs. As was true for SAED, HR-TEM averages over the entire thickness of the analysed area, so even though the images appear to show atomic rows of a surface, the superstructure results from the whole of the analysed volume. The insets are Fast Fourier Transforms (FFT) of the HR-TEM images. FFT uses a mathematical model to represent repeating patterns, such as atomic spacing, as intensity spots. The spots represent distances between repeating planes, drawn in reciprocal space with infinity at the centre of the FFT. Two spots describing a line through the centre of the FFT tells that several atomic rows lie perpendicular to that direction. Pure GR has a homogeneous pseudo-hexagonal atomic structure (Figure 7.13a), but 20 hours after addition of Cr(VI), double-spacing is observed in images from the edge of the GR crystals (Figure 7.13b). However, the pattern varies locally. This inhomogeneity over the analysed area of the edges, relatively early after addition of Cr(V), is probably why double spacing was not observed with SAED.

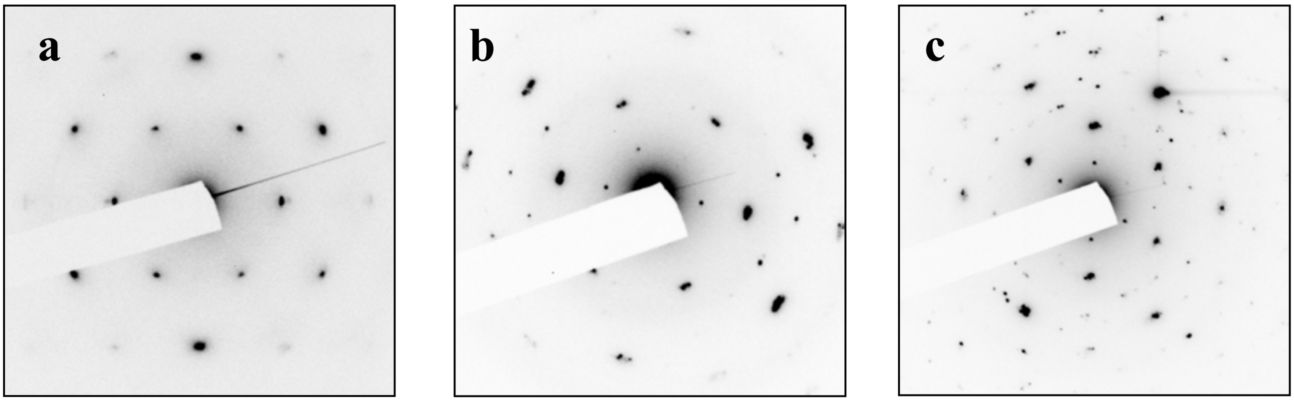

Figure 7.12: Double spacing in SAED patterns revealing a superstructure. a) SAED from pure GR_{SO4} for reference; b) SAED from the edge of a GR morph from suspension $M_{5\ days}$ has extra spots compared to pure GR_{SO4}. It reveals a doubling of the unit cell, probably caused by the incorporation of Cr(III); c) goethite crystals inside a GR morph from suspension $H_{6\ days}$ where double spacing can also be seen. In both cases there are composite spots, which result from the superposition of crystals with slightly different crystallographic orientation.

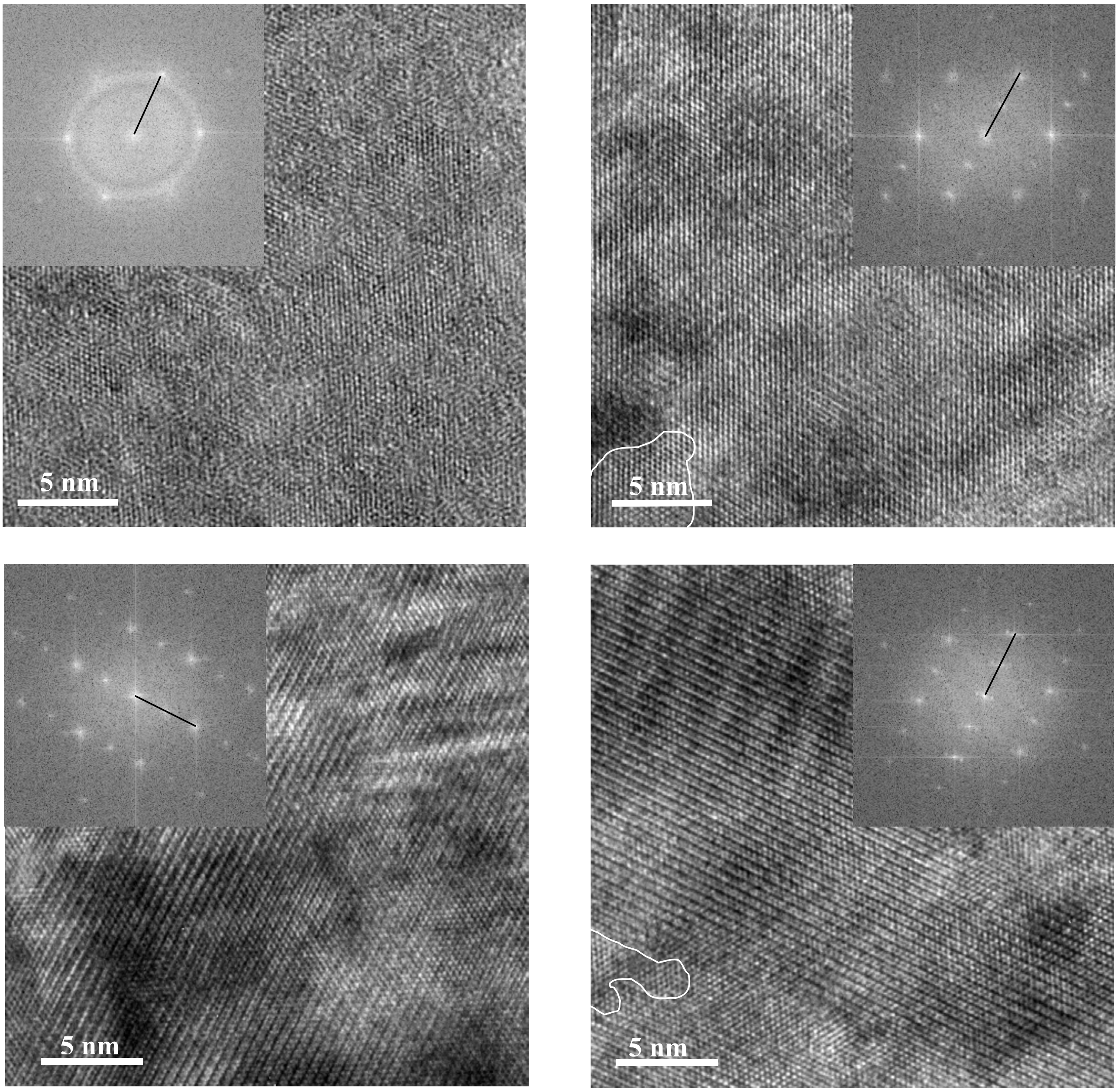

Figure 7.13 HRTEM images of GR and GR morphs: a) pure GR, b) edge of GR morph from suspension $H_{20\ hrs}$, c) crystal growing inside GR morph from suspension $H_{20\ hrs}$ and d) crystals growing inside GR morph from suspension $M_{10\ days}$. Double spacing is observed as interchanging light and dark atomic rows. The double spacing becomes more pronounced as the equilibration time increases, meaning the structure is maturing. The double spacing is probably caused by the even distribution of Cr(III) in the structure GR and goethite structures. In some of the images there are areas without double spacing (within white lines). In this size reproduction of the images it may appear that there are several areas, however, when the images are enlarged, weak double spacing appear in those areas.

The crystals in GR morphs from the same suspension showed much clearer double-spacing, (Figure 7.13c), suggesting a more homogenous distribution of Cr. The spots resulting from the superstructure are initially weaker than the rest, but as the crystals age and the double-spacing becomes even more pronounced, the spot intensity levels out so that after 10 days, they all have the same intensity (Figure 7.13d). This may indicate an even distribution of Cr in the goethite structure. In other words, at this point the system is close to or at equilibrium.

The cores behave differently than the edges of the GR morphs. Total XEDS counts are very low at the GR cores from suspensions $H_{t > 20\ hrs}$ indicating that only a small amount of material is present and AFM images from a similar suspension revealed morphologies that resemble broken GR edges (Figure 7.14). This is interpreted as partial dissolution of the core. On most TEM and AFM images there is no major topography in the center of the crystals indicating that the core material dissolves in layers as opposed to patches or holes. However, on a single TEM image obtained, there were two areas of different material thickness, (Figure 7.15), but each domain appeared to have the same thickness throughout, supporting evidence for layer-by-layer removal of the GR core. HR-TEM images of the cores show only a hint of double-spacing (data not shown), so Cr substitution is sparse.

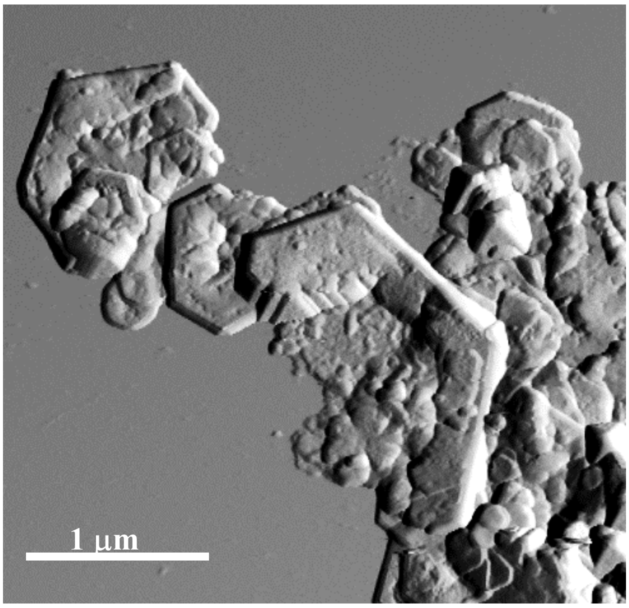

Figure 7.14: AFM deflection image of a broken GR_{SO4} crystal from a suspension of high chromium concentration and relatively low equilibration time ($H_{25\ hrs}$). Its morphology suggests a dissolved core, leaving a destabilised edge that eventually broke. A tip artefact is visible on the top inner side of the edge.

The amount of amorphous Fe-Cr solid decreases as the suspension equilibrates. TEM images from the suspension of high Cr concentration show some patches of the amorphous material after 10 days, but from the suspension $M_{5\ days}$ no amorphous material was observed. Apparently it had dissolved for the production of Cr-goethite.

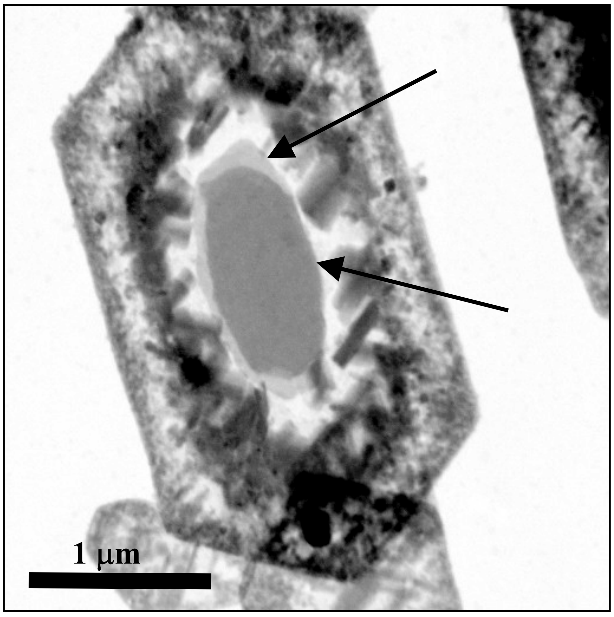

Figure 7.15: HAADF-STEM image with reversed grey-scale of a GR morph from suspension $H_{20\ hrs}$. Goethite crystals are growing from the edges towards the core that is dissolving. The dissolution seems generally to happen layer-by-layer but in this particular example, there are two levels of dissolution. However, it is clear that the core does not dissolve in irregular patches.

7.2.1.3 Summary of Chemical Composition of the Solids

The solids from each sample event were examined for chemical composition with XEDS. The goethite crystals and edges of GR morphs from suspension *M* had Cr/Cr + Fe ratios of about 5%, whereas those from suspension *H* had Cr/Cr + Fe ratios of about 9%. This is about the same as after 10 minutes. Thus no Cr was released to solution, indicating that Cr is trapped.

The sulphur content of the GR crystals was also measured as a function of reaction progress. It changed when chromate was added. The S/S+Fe concentration averaged from XEDS measurements of four pure GR crystals was 6.5%, with a spread from 4.2% to 10%. However, in the edges of reacted crystals from *M*, the average S/S+Fe percentage was only 1.4% with a spread from 1.1% to 1.9%, based on 5 crystal edge measurements. In edges of reacted crystals from *H*, the average S/S+Fe percentage was 3.1% with a spread from 2.8% to 3.5% based on 3 crystal edge measurements. This can be explained by CrO_4^{2-} substitution of SO_4^{2-} as it enters the interlayer. The S content of crystals from *H* is slightly higher, the opposite of what one would expect. The reason for this is unclear, but one hypothesis is that a high concentration of chromate blocks the interlayer faster, thereby limiting sulphate exchange.

XEDS measurements of silica content were performed. The Si/Si+Fe counts percentage was 2.3% with a spread from 1.1% to 3.9%, averaged over 20 measurements on pure and reacted GR crystals. This silica has most likely come from dissolution of the glass reaction and storage vessels. Hendriksen and Hansen (2004) investigated the influence of Si on nitrate reduction by GR_{Cl}. They concluded that the ratio of "adsorbed silicic acid (mole) / $Fe(II)_{GR}$ (mole)" needs to be no more than 1% before it affects reaction rates. They proposed that silica blocks reactive surface sites on GR_{Cl} and the same may be true in the case of Cr(VI) reduction by GR_{SO4}. Thus, GR_{SO4} reduction of Cr(VI) may be even faster in a pure system than the results from the present work show.

The concentration of Fe in solution, mostly as ferrous Fe, progressively increases during equilibration when $Ox_{Cr(VI)/Fe(II)} < 82\%$. This indicates that no new Fe(II)-bearing compound, such as magnetite, is forming. When $Ox_{Cr(VI)/Fe(II)} = 131\%$, i.e. when there is more Cr(VI) present in solution than can be reduced by the GR_{SO4}, no Fe(II) can be detected in solution. In this suspension, the concentration of Cr(VI) remaining in solution decreases slowly (Appendix B) indicating a slower rate of reaction when initial Cr(VI) concentration is high, or post-reduction adsorption on the ferric end product.

7.2.1.4 Other Solid Phases

Another type of goethite crystals was identified with SAED. They appeared in all samples from suspensions with chromate (Figure 7.17) after 10 minutes. These more elongate crystals were not directly associated or connected to GR and contained very little chromium, if any. The XEDS analysis gave <1%, which is within the margin of error. Similar forms were also observed in AFM after reaction between GR and Cr(VI) (Figure 7.16) and these small elongate crystals resemble images of goethite crystals

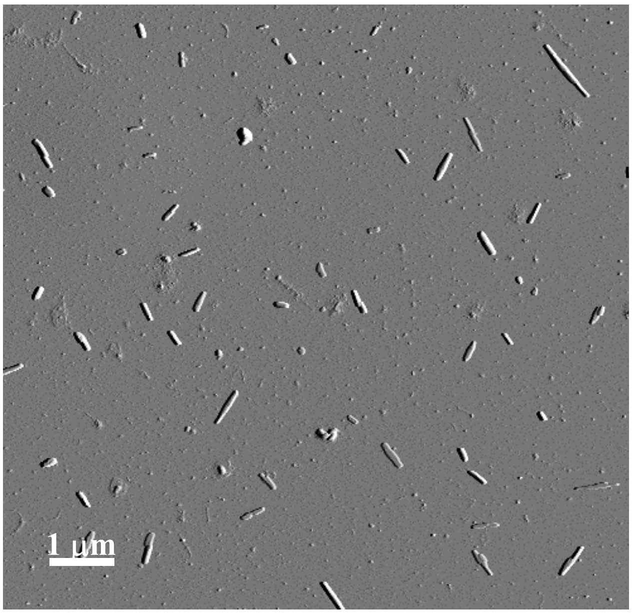

Figure 7.16: AFM deflection image of small particles, identified as goethite. A few similar particles were observed with TEM, but those were usually "trapped" under GR_{SO4} crystals. Total absence of GR associated with these particles suggests that these formed from nucleation in solution.

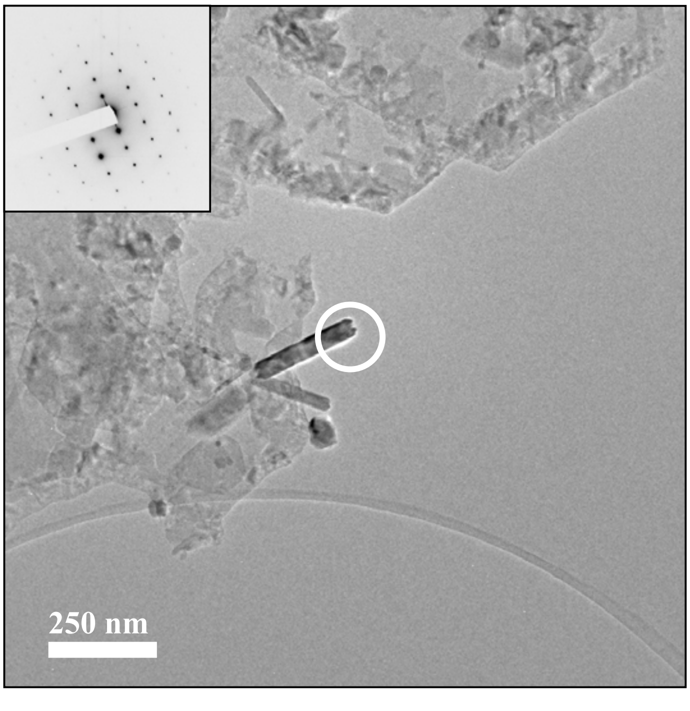

Figure 7.17: An isolated goethite particle from $M_{10\ days}$. It does not contain Cr and appears unassociated with the GR particles. The inset is an SAED pattern from within the white circle, which confirms phase identity, but note that the orientation is not the same as for the goethite crystals formed inside the GR morhs. Orientation, composition and lack of relationship to other grains suggest that this crystal formed by nucleation in solution. This crystal morphology did not appear in the suspension before Cr(VI) was added.

synthesised without Cr by Østergaard (2004). GR was completely absent suggesting that the crystals formed after nucleation in solution. Because this other type of goethite does not govern the Cr(III), it will not be treated in further detail as an end product.

The magnetite that was present in the TEM samples also needs to be considered, because some researchers determined magnetite to be an end product of GR oxidation by Cr(VI) (Bond and Fendorf, 2003) and magnetite could take up some of the Cr. In most samples, however, Cr associated with magnetite was below detection limits. Only in suspension *H* was it possible to find Cr associated with magnetite. An XEDS map of such a crystal (Figure 7.18) shows that the Cr concentration is almost evenly distributed, but slightly higher at the circumference of the crystals than in the "centre". Considering the ball-like crystal shape, and the fact that the crystal is viewed in transmission, a structural incorporation would yield higher Cr counts in the centre where the crystal is thickest, while a surface layer would yield higher Cr counts at the circumference of the crystal, such as we see. This indicates that Cr is deposited only on the outside of the crystal. For this reason and because Cr associated with magnetite is below detection in suspension *M*, it is unlikely that magnetite is an end product in these experiments. Furthermore, identical end products, i.e. Cr-substituted goethite, were obtained in experiments both with and without the initial presence of magnetite and oxidation features on GR crystals. These observations also imply that the result of too fast oxidation in the synthesis of GR_{SO4} is without significance for the obtained end product of

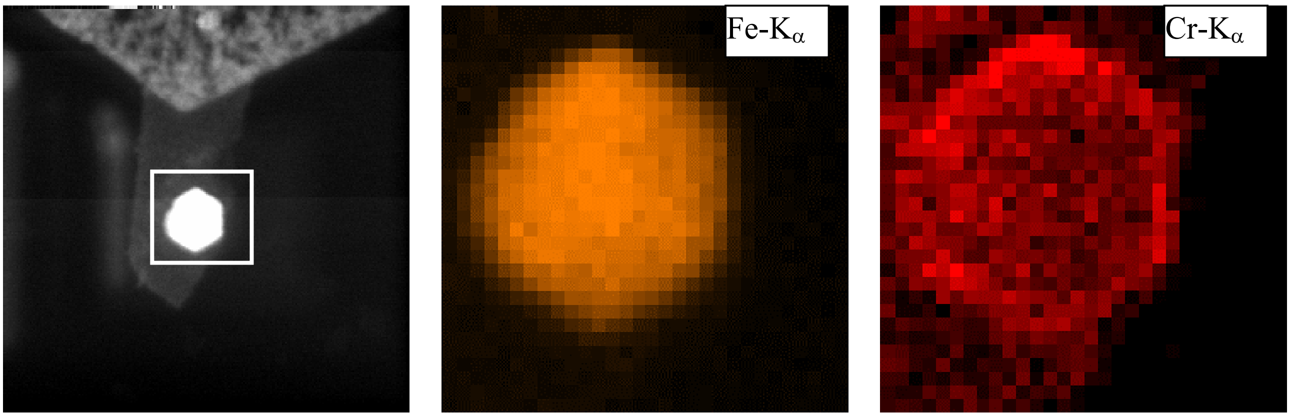

Figure 7.18: XEDS maps of ball-like magnetite crystal. These images do not represent a cross-section, but rather an averaging over the complete volume of the sphere. Lighter colors indicate higher intensity. The highest counts for Fe are found in the middle of the image, whereas the highest counts for Cr are found at the circumference. This suggests that Cr is found only at the surface, and not incorporated into the magnetite together with Fe. The XEDS boxes are about 70 nm^2.

the reaction between GR_{SO4} and Cr(VI), even though it probably influences the rate of reaction. This work has focussed on chromate concentrations *M* and *H* because of limited time available on the TEM. Experiments with very high concentrations of Cr(VI), however, indicate that the end product depends on whether there is an excess of Cr(VI). When Cr(VI) concentration is increased above the reduction capacity of GR_{SO4}, goethite is no longer the end product but rather only an intermediate product, as shown with XRD (Figure 7.19). The phase that evolved was not identified because it did not match any database patterns, but the broad peaks lie in the vicinity of the main peaks for GR_{SO4} and goethite, so probably represents relics of them. A quick AFM analysis of that suspension revealed interesting crystals, some of which were not observed among the solids resulting from solutions of lower Cr concentration (Figure 7.20). Determinations of this crystal structure and the reasons for its development are topics for future work.

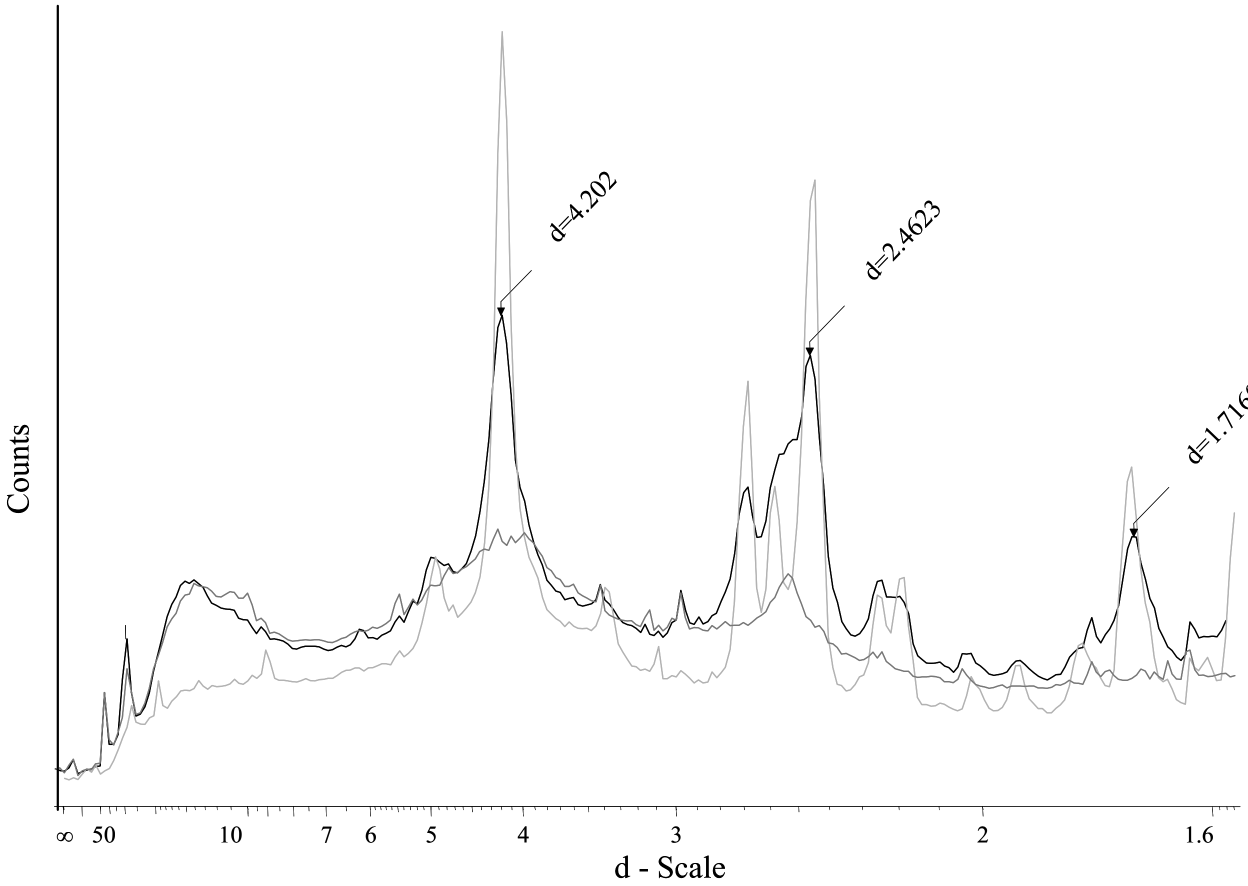

Figure 7.19: XRD trace of samples from *VH*. The light grey trace is goethite (G_{GR}) obtained by aerial oxidation of GR_{SO4} for reference. The black trace denoted with d-values is from $VH_{10\ min}$ and clearly shows goethite peaks, but others are also present. The dark grey trace is from $VH_{24\ hrs}$. Here, the goethite peaks have disappeared. There is a broad peak around d= 10-25 Å, which is probably, which is probably a relic from GR_{SO4}. The broad peaks near 4.25 Å and 2.55 Å are the remains of goethite.

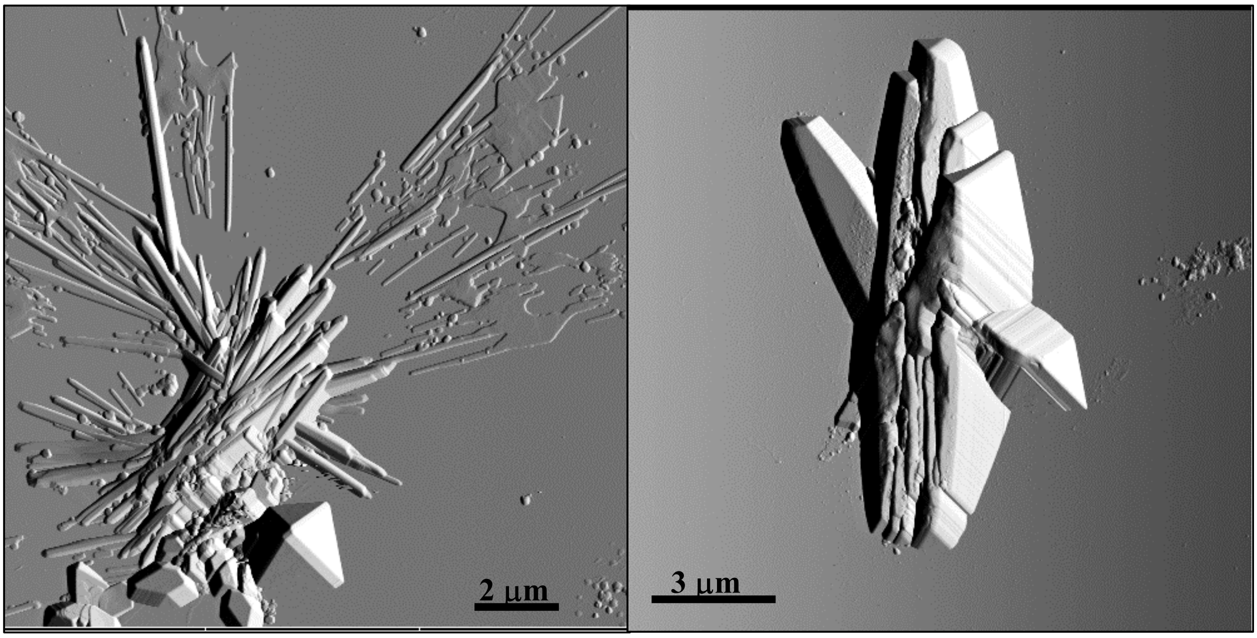

Figure 7.20: AFM deflection image from samples taken from the *VH* suspension showing unidentified phases and aggregate crystal habit. *Left*: Apart from the long thin ones, some smaller euhedral crystals are seen in the lower left corner. The large pyramid is an image of the tip. *Right*: Based on the evolved face morphology, these crystals have a crystal structure similar to that of the smaller crystals in the lower left corner of the left image; they are probably of the same phase.

7.2.2 End Products in The Literature

Loyaux-Lawniczak et al. (1999) were the first to investigate the reduction of chromate by GR, GR_{SO4} in this case, and determined the end product to be Cr-substituted ferrihydrite, which is a poorly ordered Fe(III) compound. GR_{SO4} was synthesised by the “non-static” pH method and when Eh started to rise steeply, enough chromate to oxidise all Fe(II) in the GR_{SO4} was added. Oxygen was not excluded from the system at this point, so the aerial oxidation was allowed to proceed. The continued oxidation by O_2 may have disturbed crystal growth. Also, it seems that the system was not allowed to equilibrate before the solids were extracted and analysed. This means that the solids could have been trapped in an intermediate state, considering that crystal growth can be a slow process. The oxidation state of the chromium was investigated with XPS and it was determined that more than 95% of all Cr atoms in the solid material were Cr(III). XPS is a highly surface sensitive technique so only those Cr atoms that are at the surface undergo investigation. Bombardment of the sample by X-rays releases electrons, so insulating samples, such as those studied here, accumulate charge and can oxidise as a result of the analysis (Astrup et al., 2000). However, Cr(VI) in this sample remains below detection, indicating that the concentration of Cr(VI) before analysis was very low.

Loyaux-Lawniczak et al. (2000) reinvestigated the reduction of chromate by GR_{SO4} and GR_{Cl} and similarly found the end product to be poorly ordered Cr(III)-Fe(III) hydroxide similar to 2-line ferrihydrite. They used three different concentrations of chromate: $Ox_{Cr(VI)/Fe(II)}$ = 25, 50 and 100%. In all cases, a portion of the solid product was collected about 40 seconds after addition of

chromate and analysed with TMS. The remaining suspension was oxidised for another hour or two by O_2 until no Fe(II) was left and samples for XRD were then collected. Loyaux-Lawniczak et al. (2000) speculate that Cr substitutes for the interlayer anion and the subsequent rearrangement of the hydroxide layers inevitably leads to a disordered form of Fe(III)-oxyhydroxide, but their argument is not convincing because evidence is lacking. Whether the system has equilibrated after such a short time and whether the poorly ordered Cr(III)-Fe(III) hydroxide is the final end product, or only an intermediate product, is uncertain. Again the simultaneous oxidation with O_2 presents a problem because interpretations about the action of Cr(VI) are based on observations from the combined action of Cr(VI) and O_2.

Bond and Fendorf (2003) studied the solid products from reactions between various concentrations of chromate and GR_{SO4}, GR_{CO3} and GR_{Cl} at pH 7 and found in all cases Cr(III)-substituted magnetite and lepidocrocite. The concentration of magnetite was found to be highest for GR_{CO3} followed by GR_{SO4} and GR_{Cl}, while the concentration of lepidocrocite was highest for GR_{SO4} followed by GR_{CO3} and GR_{Cl}. Several problems exist in this paper: There is no evidence that Cr(III) is, in fact, substituted into magnetite or lepidocrocite. The purity of the synthesised GR is not documented and the description of the synthesis methods is insufficient for comparison, so whether for example, the particular method chosen could lead to magnetite precipitation before addition of Cr(VI) is hard to tell. How long the suspensions have equilibrated after addition of chromate is not discussed. It is only stated that the solid products were collected after complete reduction of chromate. If magnetite was present as tiny particles before addition of chromate, a long equilibration time may have matured the magnetite enough to be observed with XRD and be interpreted as an end product. The authors do not present any results, such as XRD diagrams, to prove otherwise. The relatively long Cr(VI) reduction time indicates that the magnetite could in fact have been present before addition of chromium. Another factor of possible influence on the obtained end product is that the suspensions were buffered with an organic component (MOPS buffer), which may have influenced the crystallisation of the Cr(III)-Fe(III) end products.

Legrand et al. (2004a) investigated the hypothesis that Cr(III) monolayers are deposited on the surface of the ferric product resulting from oxidation of GR_{CO3}. One experiment was performed with $Ox_{Cr(VI)/Fe(II)}$ = 100% and the end product was identified with XRD and FTIR. The authors state that mainly because of their low relative concentration in the solid samples, it was not possible to identify any Cr(III)-bearing solids with these techniques. Calculating the weight percentage of Cr, however, this seems odd. Legrand et al. (2004) had 500 μmol Fe in GR_{CO3} (= 83.3 μmol GR_{CO3}) and added 111 μmol Cr, so assuming Na and Cl from the GR_{CO3} synthesis remain in solution and essentially all Cr is partitioned to the solid where Fe and CO_3 are also found, the weight percentage of Cr is:

Mass of Cr: 111 μmol × 52 g/mol = 58 mg

Total mass: (500 μmol Fe × 55.85 g/mol) + (500/6 μmol CO_3 × 60.01 g/mol) + 58 mg Cr = 387 mg

$$\text{Wt\% (Cr)} = \frac{58\,\text{mg Cr}}{387\text{mg Fe} + \text{CO}_3 + \text{Cr}} \times 100\% = 15\% \qquad \text{Eq. 13}$$

This means that the weight percentage of a Cr-oxide should be well above the detection limit of about 2-5 wt% for XRD. The authors did identify a Cr(III) compound with surface sensitive XPS. If the layer of Cr(III) species is thin enough, as the authors state, it should be possible to get information about the mineral it was deposited on, but Legrand et al. (2004a) chose to fully oxidise the material in air before investigations with XPS. So based on the lack of evidence of a Cr compound in the bulk solid and the confirmation of a Cr(III) compound at the surface of a bulk solid identified as ferric oxyhydroxycarbonate with XRD and TMS, they concluded that Cr is deposited as monolayers at the surface of ferric oxyhydroxycarbonate particles.

7.2.3 Conclusions About End Products

The information in the literature about end products of the reaction between GR and Cr(VI) is highly conflicting. Reduction of Cr(VI) by GR_{CO3} leads to magnetite and lepidocrocite (Bond and

Fendorf, 2003) or ferric oxyhydroxycarbonate with monolayers of Cr(III) on the surface (Legrand et al., 2004a). Cr(VI) reduction by GR_{Cl} and GR_{SO4} leads to Cr-substituted ferrihydrite (Loyaux-Lawniczak et al., 1999, 2000) or magnetite and lepidocrocite (Loyaux-Lawniczak et al., 1999, 2000; Bond and Fendorf, 2003). The results from this present work explain the formation of some phases, but lack evidence to support the formation of others. The formation of an amorphous or poorly ordered Fe-Cr solid in this study confirms what Loyaux-Lawniczak et al. (1999; 2000) obtained from the reaction between K_2CrO_4 and GR_{SO4} after a few minutes, i.e. Cr-ferrihydrite. However, in these experiments, it is clear that it is only an intermediate product and not the end product as Loyaux-Lawniczak et al. (1999; 2000) interpreted. When the suspension is left to equilibrate for 5 to 10 days, Cr-substituted goethite progressively becomes more stable as the amorphous solid dissolves and provides material for goethite formation. The stability of goethite is indicated by the growth of goethite crystals inside GR_{SO4} morphs as well as increasing and narrowing goethite peaks in XRD patterns. Bond and Fendorf (2003) obtained Cr-substituted lepidocrocite. Because aerial oxidation of GR_{SO4} can lead to formation of both goethite and lepidocrocite, the same may be true for oxidation by Cr(VI). So Cr-substituted lepidocrocite as an end product is consistent with Cr-substituted goethite obtained from GR_{SO4} in this work. The treatment of GR before reaction with Cr(VI), such as freeze-drying and rewetting, or the presence of organic components, does not seem to affect which solid forms as a result of the oxidation by Cr(VI) in the literature.

Goethite is only sparingly soluble and with Cr(III) substitution the solubility decreases even further. Schwertmann et al. (1989) tested the stability of a Cr-substituted goethite in a study with 7.8 mol% Cr in 6 M HCL at 25°C. The half dissolution time was 660 days compared to 8 days for pure goethite, indicating that the incorporation of Cr into goethite drastically decreases solubility. Assuming solid solution, the solubility of a Cr-substituted goethite can be interpolated if the equilibrium constants for the end members, α-FeOOH and α-CrOOH, are known. Unfortunately, a literature search did not reveal an equilibrium constant for the dissolution of bracewellite, the α-CrOOH phase. The experimental data of Schwertmann et al. (1989) does, however, strongly indicate that goethite is a very good sink for Cr(III).

7.3 MECHANISM

There are various mechanisms co-operating when Cr(VI) is reduced by GR_{SO4}. They may be grouped in two stages of the reaction. The first is the reduction stage, represented here with observations from TEM and AFM after 10 minutes. The other is the equilibration stage, which was observed in snapshots at various times from 20 to 240 hours.

7.3.1 Stage I - Reduction of Cr(VI)

The structure of GR_{SO4} is open along the interlayers, so CrO_4^{2-} ions feel the electrons from the Fe(II) inside the crystal as well from those on the surface of GR_{SO4}. The altered structure and composition, as observed with AFM and TEM, of the edges of GR_{SO4} crystals proves that GR_{SO4} has been oxidised through diffusion of chromate in and sulphate out. Once inside the crystal, Cr(VI) oxidises some Fe(II) to Fe(III) and is in return reduced to Cr(III). Both Cr(III) and Fe(III) form sparingly soluble compounds and essentially block the diffusion path way, so the Cr(VI) can only diffuse about 100 nm into the interlayer (Figure 7.4).

The cores of GR appear unchanged after 10 minutes, but a high amount of Cr, about Cr/(Cr+Fe) =10-40%, is detected there. The total XEDS counts of the cores are very low so the analyses can only be used as indications, but at least some Cr, and probably more than 10%, is present. There is no clear evidence of whether Cr is present on the surface or in the structure of the core. However, the edge that evolved upon initial reduction of Cr(VI) by GR_{SO4} indicated a limit for diffusion into the interlayer. For the Cr to be incorporated in the structure of the core, if would have to diffuse through the hydroxide sheet, which is unlikely because reduction occurs within minutes. Thus, it is interpreted that the Cr detected by XEDS from the core of the GR morphs is present as a surface layer. An explanation is that simultaneously with the interlayer penetration and reduction, there is electron transfer across the hydroxide layers to the surface of the GR crystals. The water in the interlayer combined with the presence of Fe(III) in the interlayers would make electron transfer very fast, so when Cr(VI) comes near the surface of a GR crystal, it would immediately be reduced unless other chromates were in its way.

The distribution of Cr argues for this mechanism as well. If the Cr was to be distributed evenly with Fe in the structure, the proportion should be as follows, assuming a stoichiometric reduction of Cr(VI) by Fe(II) in GR_{SO4}:

Stoichiometric reduction of Cr(VI) by GR_{SO4}:

$$3\,\mathrm{Fe(II)_4\,Fe(III)_2} + 4\,\mathrm{Cr(VI)} = 18\,\mathrm{Fe(III)} + 4\,\mathrm{Cr(III)} \qquad \text{Eq. 14}$$

Average Cr content in Fe phase:

$$\frac{\mathrm{Cr}}{\mathrm{Cr}+\mathrm{Fe}} = \frac{4}{4+18}\cdot 100\% = 18\% \qquad \text{Eq. 15}$$

Using the experiments with high Cr concentration as an example and assuming stoichiometric interlayer reaction between Fe(II) and Cr(VI), the resulting Cr/(Cr + Fe) of the GR edges should be at maximum 18%. It was measured to be 9%, suggesting that some amount of Fe(II) remains. However, because all Cr(VI) is reduced within 5 minutes and because almost all Fe(II) is needed for the reduction, it could also indicate that some Fe(II) had been oxidised on the surface at the edges by the same mechanism as in the cores, i.e. electron transfer across the Fe-hydroxide sheets to the surface .

A fast reaction at the surface of GR_{SO4} could also explain the formation of the observed amorphous compound. If 3 Fe(II) were to react head-to-head with 1 Cr(VI), the precipitate resulting from that reaction would have a Cr/(Cr + Fe) of 25% instead of 37% as observed. Fe, oxidised at the surface, has a higher solubility than Fe oxidised inside the crystal, so the high Cr concentration in the Cr-ferrihydrite becomes possible if electron transfer from the inner parts of the crystals reduces relatively more Cr(VI) than the amount of Fe released from the GR_{SO4}.

7.3.2 Stage II - Formation of Cr-Goethite in GR Morphs

The end product, Cr-substituted goethite, is formed gradually. Already after 10 minutes, traces of goethite are observed in the XRD patterns. Because the edges of the GR_{SO4} are oxidised through exchange in the interlayer and because the structure is so similar to goethite, it is interpreted that the edges approach a goethite structure as the Fe(II) is oxidised and Cr incorporated. This is supported by the ability of that material to act as nuclei for the growth of goethite crystals from the inside edges. Coincident zone axes for the edge and the core goethite crystals were observed with SAED, confirming topotactic growth. As the crystals become larger and grow away from the edge, the zone axis tilts slightly so composite spots are observed in the SAED pattern (Figure 7.12c). The goethite crystals grow as material from the dissolving amorphous Cr-Fe solid, as well as from the slowly dissolving cores, becomes available. The weakest area of the GR morph is the frontier between the Cr(III)-Fe(III) edges and the core, so dissolution begins here. The cores dissolve slowly and some remain semi-stable for several days. Dissolution happens layer by layer, which indicates that the bonds holding the layers together are still weaker than the bonds within the hydroxide layers, even though these consist mainly of Fe(III) by this time in the reaction.

The long, thin Cr-free goethite crystals that were observed in the suspension 10 minutes after addition of chromate were not associated with GR and must have formed separately in solution. Because goethite was able to form in the suspension and not incorporate Cr(III), it is interpreted that Cr(III) was not present as an aqueous species when they formed. If it was, Cr(III) would have sequestered into the goethite because of its affinity for it. Further, Cr(VI) in solution and perhaps adsorbed on the growing crystals could not be incorporated nor reduced by the goethite This means that Cr(VI) was only reduced when associated with GR_{SO4}. The Fe(II) of the supernatant may have contributed slightly to Cr(VI) reduction, but results suggest this was negligible.

7.3.3 Mechanisms in The Literature

The literature presents mostly vague discussions about the mechanisms responsible for the reduction of Cr(VI) by various GR types. Most interpretations are based on macroscopic observations and the models are primarily based on rate of reaction data. Bond and Fendorf (2003), who compared GR_{Cl}, GR_{SO4} and GR_{CO3}, argue for interlayer reactivity for all types. They suggest that the morphology of the interlayer anion compared to the morphology of chromate has an effect on the exchange rate and therefore the mechanism. Because CrO_4^{2-} is tetrahedrally coordinated, just as is SO_4^{2-}, chromate may have a higher affinity for interlayers of GR_{SO4} than of GR_{CO3} or GR_{Cl}, which both have a smaller anion. The introduction of chromate into the interlayers of both GR_{SO4} and GR_{Cl}, is also proposed by Loyaux-Lawnizcak et al. (1999, 2000) who argue that departure of interlayer anions, insertion of Cr and subsequent rearrangement of the hydroxide sheets produces the highly disordered form of ferric oxyhydroxide, i.e. 2-line ferrihydrite, they obtained in their work. There may exist a difference between mechanisms for Cr(VI) reduction by freshly synthesised GR and GR that has been freeze-dried and rewetted with subsequent shrinkage and reexpansion of the interlayer volume. However, thorough mechanistic studies lack in the literature, so whether this is the case is uncertain.

Though Bond and Fendorf (2003) point toward interlayer exchange of Cr(VI) in GR_{CO3}, surface reduction appears to be the major mechanism, as results by Williams and Scherer (2001) and Legrand et al. (2004a) strongly support. A mechanism for reduction of Cr(VI) and concomitant deposition of a Cr(III) precipitate at the surface of GR was proposed by Legrand et al. (2004a). After one Cr(III) monolayer has been deposited, the subsequent reduction requires electron transfer across the ferric oxyhydroxycarbonate (ex-GR) and Cr(III) layers, causing the relatively slow reduction rates compared to those obtained in this work. However, even though their model fits the data very well, the determination of the end product is not convincing so the proposed mechanism may have to be reconsidered.

7.3.4 Conclusions About Mechanism

Interlayer exchange of Cr(VI) into GR_{SO4}, proposed by several researchers, is supported by the results from this work. However, it is not the only mechanism responsible for the reduction of Cr(VI), which also involves electron transfer across the hydroxide sheets. The reaction between Cr(VI) and GR_{CO3} appears to follow another mechanism, i.e. primarily surface reduction with extensive electron diffusion, eventually across an increasingly thick Cr(III) precipitate on the surface. The reduction of Cr(VI) by GR_{Cl} has not been investigated thoroughly enough to allow proposing a mechanism, but based on the similarity with GR_{CO3} regarding interlayer spacing, it probably follows a similar pathway, i.e. surface reduction.

8 CONCLUSION

The mechanisms of Cr(VI) reduction by the various GR types decides the rate of reaction as well as the composition and structure of the Cr(III)-containing end product. When Cr(VI) is reduced by GR_{SO4}, the mechanism is interlayer exchange from the edges of the GR_{SO4} crystals coupled with extensive electron transfer across the Fe-hydroxide layers mainly in the cores of the GR_{SO4} crystals but also the edges. Interlayer exchange causes formation of a sparingly soluble Cr(III)-Fe(III) compound, probably goethite, whereby the edges are stabilised. Electron transfer is responsible for the initial formation of an amorphous Cr-Fe solid, probably Cr-ferrihydrite. However, this phase is only an intermediate product. It dissolves and re-precipitates as Cr-substituted goethite, growing inside the GR morphs, nucleating on the edges Cr-goethite. This phase is very stable at ambient conditions, so Cr is effectively trapped when reduced by GR_{SO4}.

Other work shows that when Cr(VI) is reduced by GR_{CO3}, the mechanism is primarily reduction at the surface (Williams and Scherer (2001); Legrand et al., 2004) with the possible formation of a thin Cr(III) surface layer. As the Cr-layer thickens, electron diffusion across it becomes difficult, causing the rate of reaction to be significantly slower than for GR_{SO4}. Cr(III) is not incorporated into the structure of a stable end product, so Cr(III) is much more prone to return to an aquatic environment and be reoxidised to Cr(VI) when reduced by GR_{CO3} than when reduced by GR_{SO4}. A similar mechanism may control the reaction between Cr(VI) and other GR1 compounds such as GR_{Cl}. Of the most commonly tested GR's, i.e. GR_{SO4}, GR_{CO3} and GR_{Cl}, Cr(VI) should therefore preferably be reduced by GR_{SO4} in order to limit bio-accessibility.

Whether redox sensitive, one-dimensional molecules have a higher affinity for GR1 compounds than for GR2 compounds is not treated in the literature. However, it is clear that at least two different models are needed to describe the reduction of Cr(VI) by GR1 and GR2 compounds. Extrapolating the results from this work to directly include the reduction of other redox-active contaminants by GR_{SO4} is difficult, because Cr is a special case. Reduction of Cr(VI) yields Cr(III), which is very similar to Fe(III), regarding size, valence state and bonding character, so it is easily incorporated into the structure of the ferric end product. Reduction of e.g. U(VI) and Se(VI), on the other hand, yields U(IV) and Se(IV), so substitution for Fe(III) would produce an electron deficiency. To restore neutrality, the compound could include monovalent anions or incorporate holes into the structure, which would therefore lead to a different mechanism. Even more complicated is the reduction of e.g. chlorinated organic compounds such as TCE, because their behaviour is far from that of chromium. What the end product might be in these cases and what phases govern the reduced elements needs to be examined experimentally.

8.1.1 Implications

The results from this work may be used when considering parameters that should be evaluated in order to optimise the performance of existing and future reactive barrier systems for groundwater remediation or waste disposal, such as iron PRBs and steel-containing spent nuclear fuel canisters. If possible, sulphate should be in the system to ensure GR_{SO4} formation over GR_{CO3} when the target element is Cr(VI). If other elements are the target, it may be wise to investigate its reactions with various GR types to identify which produce the best sink.

8.1.2 Future work

For the purpose of gaining further knowledge about the behaviour of GR, the following subjects would be relevant to investigate: i) Whether the behaviour of GR_{SO4} grown on pure iron, as in iron PRBs or in steel containing spent fuel canisters, is different from that of GR_{SO4} precipitated from a solution, ii) what happens when the concentration of Cr(VI) is above the reduction capacity of GR_{SO4}? iii) Also, it is important to determine the influence of organic material, silica and other passivating compounds on the interaction between GR_{SO4} and chromate or other redox sensitive contaminants. iv) Finally, it would be interesting to investigate the interaction between the most common GR's likely to exist in nature and various redox sensitive compounds that are unwanted in nature. GR_{CO3} or GR_{Cl} and GR_{SO4} could serve as models for GR1 and GR2 in similar experiments as was done in this work. A deeper understanding of the systems could be gained with complementary techniques that give information about the bonding environments of the individual elements, those in the bulk and those at the surface interacting with the surrounding media.

9 ACKNOWLEDGEMENTS

I am very grateful for the inspiring advisory of Susan L. S. Stipp. Your wisdom, enthusiasm and drive played a big part in making me choosing geochemistry as my profession. I would like to thank the entire NanoGeoScience group, especially Bo C. Christiansen for fruitful discussions and technical aid. The assistance of the technical staff of Copenhagen Geological Institute is greatly appreciated. Special thanks goes to Birgit Damgaard, Helene Almind and Peer Jørgensen. I appreciate the kindness of Rod Ewing for inviting me to interact with his group at the University of Michigan, USA. I am incredibly grateful for the assistance from Satoshi Utsunomiya who is a wizard with a TEM and I want to thank Frannie Skomurski and Kathy Traexler for all the help they provided me and for making me feel so welcome. I appreciate the help of Toncí Balíc-Zûníc, regarding XRD. I am grateful towards Hans Christian Bruun Hansen for inviting me to his laboratory to learn the GR synthesis method and thanks to Hanne Nancke-Krogh for teaching it to me. Finally, my family deserves the greatest acknowledgement for not deserting me during the harder times. Very special thanks to my beloved husband and son.

Research and travel expenses were provided by the Swedish Nuclear Waste Management Company (SKB) and the Danish Research Council.

10 REFERENCES

APHA, AWWA, WPCF, *Standard methods for the examination of water and wastewater*, American Public Health Association, American Water Works Association and Water Pollution Control Federation, Washington, USA, 14th ed, **1975**.

Astrup, T, Stipp, S.L.S., Christensen, T.H., *Immobilization of chromate from coal fly ash leachate using an attenuating barrier containing zero-valent iron*, Environmental Science and Technology, **2000** (34): 4163-4168.

Bentor, Y., *Periodic Table, Chromium*, [Online] Available from: http://www.chemicalelements.com/elements/cr.html, **2005**, accessed March 9, 2005.

Bernal, J.D., Dasgupta, D.R., Mackay, A.L., *The oxides and hydroxides of iron and their structural inter-relationships*, Clay Mineral Bulletin, **1959** (4): 15-30.

Binning, G., Quate, C.F., Gerber, Ch., *Atomic Force Microscope*, Physical Review Letters, **1986**, 56(9): 930-933.

Binning, G., Rohrer, H., Gerber, Ch., Weibel, E., *Tunneling through a controllable vacuum gap*, Appl. Phys. Lett., **1982**, 40(2): 178-180.

Bond, D.L., Fendorf, S., *Kinetics and structural constraints of chromate reduction by green rusts*, Environmental Science and Technology, **2003**, 37(12): 2750-2757.

Buerge, I.J., Hug, S.J., *Kinetics and pH dependence of Cr(VI) reduction by Fe(II)*, Environmental Science and Technology, **1997,** 31: 1426-1432.

CEQG, *Summary of Canadian Environmental Quality Guidelines*, update 2002 [Online] http://www.ccme.ca/assets/pdf/e1_06.pdf, **2002**.

Christiansen, B.C., *A transformational, structural and natural occurrence study of green rust*, Master Thesis, Geological Institute, Copenhagen University, Denmark, **2004**.

Chromiuminfo, *Chromium and healthy insulin metabolism*, [Online], Available from: http://www.chromiuminformation.org/WHAT_chromium_insulin.htm, **2004**, accessed January 21, 2004.

Chung, J.-B., Sa, T.-M., *Chromium oxidation potential and related soil characteristsics in arable upland soils*, Commun. Soil Sci. Plant Anal., **2001**, 32 (11&12), 1719-1733.

Cornell, R.M., Schneider, W., *Formation of goethite from ferrihydrite at physiological pH under the influence of cysteine*, **1989**, 8(2): 149-155.

Dodge, C.J., Francis, A.J., Gillow, J.B., Halada, G.P., Eng, C., Clayton, C.R., *Association of uranium with iron oxides typically formed on corroding steel surfaces*, Environmental Science Technology, 2002, 36: 3504-3511.

Drissi, S.H., Refait, P., Abdelmoula, M., Genín, J.-M.R., *The preparation and thermodynamic properties of Fe(II)-Fe(III) hydroxide-carbonate (green-rust-1) - Pourbaix diagram of iron in carbonate-containing aqueous-media*, Corrosion Science, **1995**, 37(12): 2025-2041.

Drits, V.A., Bookin, A.S., *Crystal structure and x-ray identification of layered double hydroxides*, In: Rives, V. (ed.), Layered double hydroxides: Present and future, Nova Science Publishers, Inc, New York, USA, **2001**: 39-92.

Eggleston, C., *High resolution scanning probe microscopy: Tip-surface interaction, artifacts, and applications in mineralogy and geochemistry*, In: Scanning probe microscopy of clay minerals, ed.: Nagy, K.L., Blum, A.E., The Clay Minerals Society, USA, **1994**: 1-90.

Erbs, M., Hansen, H.C.B., Olsen, C.E., *Reductive dechlorination of carbon tetrachloride using iron(II) iron (III) hydroxide sulfate (green rust)*, Environmental Science and Technology, **1999**, 33: 307-311.

Farmer, J.G., Graham, M.C., Thomas, R.P., Licona-Manzur, C., Paterson, E., Campbell, C.D., Geelhoed, J.S., Lumsdon, D.G., Meeussen, J.C.L., Roe, M.J., Conner, A., Fallick, A.E., Bewley, R.J.F., *Assessment and modelling of the environmental chemistry and potential for remediative treatment of chromium-contaminated land*, Environmental Geochemistry and Health, **1999**, 21: 331–337.

Feitknecht, von W., Keller, G., *Über die dunkelgrünen hydroxyverbindungen des eisens*, Zeitschrift für anorganische chemie, **1950**, Vol 262: 61-68.

Fendorf, S., Wielinga, B.W., Hansel, C.M. *Chromium transformations in natural environments: The role of biological and abiological. processes in chromium(VI) reduction*, International Geology Review , **2000**, 42 (8): 691-701.

Genín, J.-M.R., Ruby, C., *Anion and cation distributions in Fe(II–III) hydroxysalt green rusts from XRD and Mössbauer analysis (carbonate, chloride, sulphate, . . .); the "fougerite"* mineral, Solid State Sciences, **2004**, 6: 705–718.

Gibbs, C.R., *Characterization and application of ferrozine iron reagent as a ferrous iron indicator*, Analytical Chemistry, **1976**, 48 (8): 1197-1201.

Goonan, T.G., Papp, J.F., Chromium statistics, U. S. Geological Survey, http://minerals.usgs.gov/minerals/pubs/of01-006/chromium.pdf, **2003**, accessed January 18, 2004.

Hansen, H.C.B., Borggaard, O.K., Sørensen, J., *Evaluation of the free energy of formation of Fe(II)-Fe(III) hydroxide-sulphate (green rust) and its reduction of nitrite*, Geochimica et Cosmochimica Acta, **1994**, 58(12): 2599-2608.

Hansen, H.C.B., *Composition, stabilization , and light absorption of Fe(II)Fe(III) hydroxy-carbonate ('green rust')*, Clay Minerals, **1989**, 24(4): 663-669

Hansen, H.C.B., *Environmental chemistry of iron (II)-iron(III) LDHs (green rusts)*, In: Rives, V. (ed.), Layered double hydroxides: Present and future, Nova Science Publishers Inc., New York, USA, **2001**: 413-434.

Hansen, H.C.B., Guldberg, S., Erbs, M., Koch, C.B., *Kinetics of nitrate reduction by green rusts – effects of interlayer anion and Fe(II):Fe(III) ratio*, Applied Clay Science, **2001**, 18: 81-91

Hansen, H.C.B., Koch, C.B., *A comparison of nitrate reduction by carbonate and sulphate forms of green rust*, Proceedings of the international clay conference, **1997**: 296-302.

Hansen, H.C.B., Koch, C.B., Nancke-Krogh, H., Borggaard, O.K., Sørensen, J., *Abiotic nitrate reduction to ammonium: Key role of green rust*, Environmental Science and Technology, **1996**, 30: 2053-2056.

Hansen, H.C.B., Koch, C.B., *Reduction of nitrate to ammonium by suphate green rust: Activation energy and reaction mechanism*, Clay Minerals, **1998**, 33 (1): 87-101.

Hansen, H.C.B., Poulsen I.F., *Interaction of synthetic sulphate "green rust" with phosphate and the crystallization of vivianite*, Clays and Clay Minerals**, 1999,** 47 (3): 312-318.

Helmenstin, A. M., *Why is stainless steel stainless*, [Online] http://chemistry.about.com/library/weekly/aa071201a.htm, **2004**, accessed January 18, 2004.

Hendriksen, P.T., Hansen, H.C.B., *The effect of orthosilicic acid on nitrate reduction by iron(II)iron(III)hydroxide chloride (green rust)*, Poster based on thesis at KVL, Denmark: Hendriksen, P.T., Reduktion af nitrat med jern(II)jern(III)hydroxid-chlorid : effekt af orthokiselsyre, **2004**: In press.

Henriksen, K., Stipp, S.L.S., *Image distortion in scanning probe microscopy*, American Mineralogist, **2002**, 87 (1): 5-16.

Hoffmann, L., Grinderslev, M., Helweg, C., Rasmussen, J.O., *Massestrømsanalyse af chrom og chromforbindelser*, Miljøstyrelsen, Miljøministeret, Miljøprojekt nr. 738 [Online], http://www.mst.dk/default.asp?Sub=http://www.mst.dk/udgiv/publikationer/2002/87-7972-374-8/html/, **2002,** accessed January 18, 2004.

Ishikawa, T., Kondo, Y., Yasukawa, A., Kandori, K., *Formation of magnetite in the presence of ferric oxyhydroxides*, Corrosion Science, **1998**, 40(7): 1239-1251.

Kaplan, D.I, Bertsch, P.M., Adriano, D.C., Orlandini, K.A, *Actinide Association With Groundwater Colloids In A Coastal-Plain Aquifer*, Radiochimica Acta, **1994**, 66 (7): 181-187.

Kersting A.B., Efurd, D.W., Finnegan, D.L., Rokop D.J., Smith, D.K., Thompson, J.L., *Migration of plutonium in ground water at the Nevada Test* Site, Nature, **1999**, 397 (6714): 56-59.

Klein, C., Hurlbut, Jr., C.S., *Manual of mineralogy*, 21st ed., **1993**, revised after Dana, J.D., John Wiley & Sons, Inc, USA.

Koch, C.B., Hansen, H.C.B., *Reduction of nitrate to ammonium by sulphate green rust*, Advances in GeoEcology, **1997**, 30: 373-393.

Koch, C.B., Mørup, S., *Identification of green rust in an ochre sludge*, Clay Minerals, **1991** 26 (4): 577-582.

Krauskopf, K.B., Bird, D.K., *Introduction to geochemistry*, 3rd ed., McGraw-Hill, Singapore, **1995**.

Larsen, M.S., *Substitution af karbonat i sulfat grøn rust, samt omdannelsesprodukter ved varierende karbonatkoncentration*, Bachelor Thesis, Geological Institute, Copenhagen University, Denmark, **2003**.

Lee, W., Batchelor, B., *Abiotic reductive dechlorination of chlorinated ethylenes by iron-bearing soil minerals. 2. Green rust*, Environmental Science and Technology, **2002**, 36: 5348-5354.

Lee, W., Batchelor, B., *Reductive capacity of natural reductants*, Environmental Science & Technology, **2003**, 37: 535-541.

Legrand, L., Figuigui, A.E., Mercier, F., Chausse, A., *Reduction of aqueous chromate by Fe(II)/Fe(III) carbonate green rust: Kinetic and mechanistic studies*, Environmental Science & Technology, **2004 (a)**, 38: 4587-4595.

Legrand, L., Mazerolles, L., Chausse, A., *The oxidation of carbonate green rust into ferric phases: Solid-state reaction or transformation via solution*, Geochimica et Cosmochimica Acta, **2004 (b)**, 68 (17): 3497-3507.

Lewis, D.G., *Factors influencing the stability and properties of green rusts*, Advances in GeoEcology, **1997**, 30: 345-372.

Lin, Z., Puls, R.W., *Potential indicators for the assessment of arsenic natural attenuation in the subsurface*, Advances in Environmental Research, **2003**, 7: 825-834.

Lipscher J., Douma M., Webexhibits, Pigments through the ages – Chrome yellow http://webexhibits.org/pigments/indiv/history/cryellow.html, **2004(a)**, accessed January 18, 2004.

Lipscher J., Douma M., Webexhibits, Pigments through the ages – Chrome orange http://webexhibits.org/pigments/indiv/history/crorange.html, **2004(b)**, accessed January 18, 2004.

Loyaux-Lawniczak, S., Refait, Ph., Ehrhardt, J.-J., Lecomte, P., Genin, J.-M.R., *Trapping of Cr by formation of ferrihydrite during the reduction of chromate ions by Fe(II)-Fe(III) hydroxysalt green rusts*, Environmental Science and Technology, **2000**, 34(3): 438-443.

Loyaux-Lawniczak, S., Refait, Ph., Lecomte, P., Ehrhardt, J.-J., Genin, J.-M.R, *The reduction of chromate ions by Fe(II) layered hydroxides*, Hydrology and Earth System Sciences, **1999**, 3(4): 593-599.

Marty, R.C., Bennett, D., Thullen, P., *Mechanism of plutonium transport in a shallow aquifer in Mortandad canyon, Los Alamos National Laboratory, New Mexico*, Environmental Science and Technology, **1997**, 31 (7): 2020-2027.

McGill, I.R., McEnaney, B., Smith, D.C., *Crystal structure of green rust formed by corrosion of cast iron*, Nature, **1976**, 259: 200-201.

McLean, W., *The manufacture of leather – part 3*, **1997**, webpage: http://www.hewit.com/sd3-leat.htm, accessed May 24, 2004.

Miljøstyrelsen, *Håndbog om trykimprægneret træ og mulige alternativer*. Miljøministeriet, Miljønyt nr. 56 [Online]. http://www.mst.dk/udgiv/publikationer/2000/87-7944-496-2/pdf/87-7944-300-1.pdf, **2000**, accessed January 21, 2004.

Miljøstyrelsen, *Undersøgelse af indholdet af Cr(VI) og Cr(III) i lædervarer på det danske marked*, Miljøministeriet, kortlægning nr. 3 [Online] http://www.mst.dk/, **2002**, accessed January 24, 2004.

Miyata, S., *Anion –exchange properties of hydrotalcite-like compounds*, Clays and Clay Minerals, **1983**, 31 (4): 305-311.

Myneni, S.C.B., Tokunaga, T.K., Brown Jr., G.E., *Abiotic selenium redox transformations in the presence of Fe(II,III) oxides*, Science, **1997**, 278: 1106-1109.

Nordstrom, D.K; Wilde, F.D., *National field manual for the collection of water-quality data: Book 9, Section A6.5, Reduction-oxidation potential (electrode method)*, **1998**, U.S. Geological Survey.

Nuffield, E.W., *X-ray diffraction methods*, John Wiley & Sons, inc., New York, USA, **1966**.

O'Loughlin, E.J., Kelly, S.D., Cook, R.E., Csencsits, R., Kemner, K.M., *Reduction of Uranium(VI) by mixed iron(II)/iron(III) hydroxide (green rust): Formation of UO2 nanoparticles*, Environmental Science and Technology, **2003**, 37(4): 721-727.

Olowe, A.A., Rezel, D., Génin, J.-M.R., *Mechanism of formation of magnetite from ferrous hydroxide in aqueous corrosion processes*, Hyperfine Interactions, **1989**, 46: 429-436.

One-Nguema, G., Abdelmoula, M., Jorand, F., Benali, O., Gehín, A., Block, J.-C., Genín, J.-M.R., *Iron(II,III) Hydroxycarbonate Green Rust Formation and Stabilization from Lepidocrocite Bioreduction*, Environmental Science & Technology, **2002**, 36: 16-20.

Pepper, S.E., Bunker, D.J., Bryan, N.D., Livens, F.R., Charnock, J.M., Pattrick, R.A.D., Collison, D., *Treatment of radioactive wastes: An X-ray absorption spectroscopy study of the reaction of technetium with green rust*, Journal of colloid and Interface Science, **2003**, 268: 408-412.

Peterson, M.L., Brown, G.E., Parks, G.A., *Direct XAFS evidence for heterogeneous redox reaction at the aqueous chromium/magnetite interface*, Colloids and Surfaces, A:

Phillips, D.H., Watson, D.B., Roh Y., Gu B., *Mineralogical characteristics and transformations during long-term operation of a zerovalent iron reactive barrier*, Journal of Environmental Quality, **2003**, 32 (6): 2033-2045.

Randall, S.R., Sherman, D.M., Ragnarsdottir, K.V., *Sorption of As(V) on green rust ($Fe_4(II)Fe_2(III)(OH)_{12}SO_4 \cdot 3H_2O$) and lepidocrocite ($\gamma$-FeOOH): Surface complexes from EXAFS spectroscopy*, Geochimica et Cosmochimica Acta **2001**, 65 (7): 1015-1023.

Refait, Ph., Abdelmoula, M., Genin, J.-M.R., *Mechanisms of formation and structure of green rust one in aqueous corrosion of iron in the presence of chloride ions*, Corrosion Science, **1998**, 40(9), 1547-1560.

Refait, Ph., Charton, A., Genín, J.-M.R., *Identification, composition, thermodynamic and structural properties of a pyroaurite-like iron(II)-iron(III) hydroxy-oxalate green rust*, Eur. J. Solid State Inorg. Chem., **1998**, 35: 655-666.

Refait, Ph., Drissi, S.H., Pytkiewics, J., Génin, J.-M.R., *The anionic species competition in iron aqueous corrosion: Role of various green rust compounds*, Corrosion Science, **1997**, 39 (9): 1699-1710.

Refait, Ph., Génin, J.-M.R., *The oxidation of ferrous hydroxide in chloride-containing aqueous media and pourbaix diagrams of green rust one*, Corrosion Science, **1993**, 34(5): 797-819.

Refait, Ph., Memet, J.B., Bon, C., Sabot, R., Genin, J.-M.R., *Formation of the Fe(II)-Fe(III) hydroxysulphate green rust during marine corrosion of steel*, Corrosion Science **2003**, 45 (4): 833-845.

Refait, Ph., Simon, L., Génin, J.-M.R., *Reduction of SeO_4^{2-} anions and anoxic formation of iron(II)-iron(III) hydroxy-selenate green rust*, Environmental Science & Technology*,* **2000**, 34: 819-825.

Roy, A. de, Forano, C., Besse, J.P., *Layered double hydroxides: Synthesis and post-synthesis modification*, In: Rives, V. (ed.), Layered double hydroxides: Present and future, New York, USA: Nova Science Publishers Inc., **2001**: 1-37.

Sandvik, http://www2.steel.sandvik.com/sandvik/0140/internet/SE02946.nsf/(DocumentsInternetWeb)/1391938D212A86DDC1256A1F00276951, **2004**, accessed January 18, 2004.

Schwertmann, U., Fechter, H., *The formation of green rust and its transformation to lepidocrocite*, Clay Minerals, **1994**, 29: 87-92.

Schwertmann, U., Gasser, U., Sticher, H., *Chromium-for-iron substitution in synthetic goethites*, Geochimica et Cosmochimica Acta, **1989**, 53: 1293-1297.

Shannon, R.D. *Revised effective ionic radii and systematic studies of interatomic distances in halides and chalcogenide*, Acta Crystallographica, **1976**, A32 (5): 751-767.

Simon, L., Francois, M., Refait, Ph., Renaudin, G., Lelaurain, M., Genin, J.-M.R., *Structure of the Fe(II-III) layered double hydroxysulphate green rust two from Rietveld analysis,* Solid State Sciences, **2003**, 5 (2): 327-334.

Simon, L., Génin, J.-M.R., Refait, Ph*., Standard free enthalpy of formation of Fe(II)-Fe(III) hydroxysulphite green rust one and its oxidation into hydroxysulphate green rust two*, Corrosion Science **1997**, 39 (9): 1673-1685.

Sino-partner, Chromium Oxide Green, http://www.sino-partner.com/chromiumoxidegreen/chromeoxidegreen-3.htm, **2004**, accessed January 21, 2004.

Stampl, P.P., *Ein basisches eisen-II-III-karbonat in rost*, Corrosion Science, **1969** (5): 185-186.

Stumm , W., Morgan, J.J., *Aquatic chemistry: chemical equilibria and rates in natural waters 3.ed.*, John Wiley and Sons Inc., New York, USA, **1996**.

Tamura, Y., *Ferrite formation from the intermediate, green rust II, in the transformation reaction of γ-FeO(OH) in aqueous suspension*, Inorg. Chem., **1985**, 24: 4363-4366.

Tamura, Y., Saturno, M., Yamada, K., Katsura, T., *The transformation of γ-FeO(OH) to Fe_3O_4 and green rust II in an aqueous solution*, Bull. Chem. Soc. Jpn., **1984**, 57: 2417-2421.

Taylor, R.M., *Formation and properties of Fe(II)Fe(III) hydroxy-carbonate and its possible significance in soil formation*, Clay Minerals, **1980**, 15 (4): 369-382.

Taylor, R.M., Schwertmann, U., Fechter, H., *A rapid method for the formation of Fe(II)Fe(III) hydroxycarbonate*, Clay minerals, **1985**, 20: 147-151.

Trapp, D., *Origins of the element names* [Online]. Available from: http://homepage.mac.com/dtrapp/Elements/color.html, **2002**, accessed January 14, 2004.

Trolard, F., Genin, J.-M. R., Abdelmoula, M., Bourrie, G., Humbert, B., Herbillon, A., *Geochimica et Cosmochimica Acta*, **1997**, 61(5): 1107-1111.

Vins, J., Subrt, J., Zapletal, V., Hanousek, F., *Preparation and properties of green rust type substances*, Coll. Czech. Chem. Comm., **1987**, 52: 93-102.

White, A.F., Peterson, M.L., *Reduction of aqueous transition metal species on the surfaces of Fe(II)-containing oxides*, Geochimica et Cosmochimica Acta, **1996**, 60 (20): 3799-3814.

WHO, *Guidelines for drinking water quality*, 3rd ed., chapter 8.7, DRAFT [Online]. http://www.who.int/docstore/water_sanitation_health/GDWQ/Updating/draftguidel/draftchap87.htm, **2004**, accessed January 21, 2004.

Williams, A.G.B., Scherer, M.M., *Chromate reduction by hydroxycarbonate green ryst*, Proceedings of the 2000 Conference on Hazardous Waste Research, **2000**: 272-281.

Williams, A.G.B., Scherer, M.M., *Kinetics of Cr(VI) reduction by carbonate green rust*, Environmental Science and Technology, **2001**, 35 (17): 3488-3494.

Williams, B.W., Carter, C.B., *Transmission electron microscopy: A textbook for materials Science*, Plenum Press, New York, USA, **1996**.

Østergaard, L.F., *A study of iron oxides formed in solutions representing hydrothermal conditions*, Master Thesis, Geological Institute, Copenhagen University, Denmark, **2003**.

11 APPENDICES

11.1 APPENDIX A

11.1.1 Solution Data

	$m_{FeSO4·7H2O}$ (g)	V_{H2O} (mL)	$V_{1M\ NaOH}$ (mL)	Fe^{2+} in supernatant after synthesis (ppm)	$V_{sample\ before\ addition\ of\ Cr}$ (mL)	C_{K2CrO4} (mol/L)	V_{K2CrO4} (mL)	$Ox_{Cr(VI)/Fe(II)}$
S3	2.7815	200	16.144	240	166	0.8	1.7	88%
T1	2.7820	200	14.963	400	165	0.1	1.3	9%
T2	2.7815	200	16.001	190	166	0.8	0.9	46%
T3	2.7820	200	16.012	175	166	0.8	2.6	131%
T4	2.7824	200	15.884	160	166	0.3	1.4	40%
T5	2.7841	200	16.004	160	166	0.3	2.65	76%

11.2 Appendix B

11.2.1 Measured Chemical Values

Element/ Analysis Technique (unit)	**Pure GR$_{SO4}$**	**Low Cr concentration (*L*)** Ox$_{Cr(VI)/Fe(II)}$ ~ 9%						**Medium Cr concentration (*M*)** Ox$_{Cr(VI)/Fe(II)}$ ~ 43%						**High Cr concentration (*H*)** Ox$_{Cr(VI)/Fe(II)}$ ~ 82%						**Very high Cr concentration (*VH*)** Ox$_{Cr(VI)/Fe(II)}$ ~131%						**GR$_{SO4}$ + $C_6H_{12}O_6$** Ox$_{Cr(VI)/Fe(II)}$ = 82%	
	---	0 min	5 min	10-30 min	~1 day	5 days	10 days	0 min	5 min	10-30 min	~1 day	5 days	10 days	0 min	5 min	10-30 min	~1 day	3-5 days	10 days	0 min	5 min	10-30 min	~1 day	5 days	10 days	5 min	30 min
Fe$^{2+}_{(aq)}$/SP (ppm)		270	226	234	252			190	25	38	116			240	~0		19	24		175	0	0	0				
Total Fe$_{(aq)}$/AAS (ppm)			230	250	284			181	20	36	94					4	20	23		176	0	0	0				
Cr$^{6+}_{(aq)}$/SP (ppm)									0						0						235	173	82			141	51
Total Cr$_{(aq)}$/AAS (ppm)			0												0	0	0	0	0		292	204	94				
Cr$^{6+}_{(solid)}$/SP (%)																								0.11%			
Total Cr$_{(solid)}$/AAS (%)																								17.2%			
Cr/Cr+Fe of GR morphs/XEDS (%)									5%						9%												
Cr/Cr+Fe of amorphous solid/XEDS (%)										25%						37%											
S/S+Fe GR edges/XEDS (%)	6.5%								1.4%					3.1%													
Si/Si+Fe/XEDS (%)	2.2%								1.8%					2.6%													

SP: Spectrophotometry
AAS: Atomic absorption spectroscopy
XEDS: X-ray energy dispersive spectroscopy

11.3 APPENDIX C

11.3.1 Pourbaix Equations

a	$H_2 = 2H^+ + 2e^-$	$E^{\circ} = -0.059$ pH
b	$2H_2O = O_2 + 4H^+ + 4e^-$	$E^{\circ} = 1.22 - 0.059$ pH
1	$Cr^{3+} + 2H_2O = CrO_2^- + 4H^+$	$\log((CrO_4^{2-}) / (Cr^{3+})) = -26.99 + 4$ pH
5	$CrO_2^- + H_2O = CrO_3^{3-} + 2H^+$	$\log((CrO^{3-}) / (\ CrO_2^-)) = -29.76 + 2$ pH
6	$H_2CrO_4^0 = HCrO_4^- + H^+$	$\log((HCrO_4^-) / (H_2CrO_4^0)) = -0.75 +$ pH
7	$2H_2CrO_4^0 = Cr_2O_7^{2-} + H_2O + 2H^+$	$\log((Cr_2O_7^{2-}) / (H_2CrO_4^0)) = 0.18 + 2$ pH
9	$HCrO_4^- = CrO_4^{2-} + H^+$	$\log((CrO_4^{2-}) / (HCrO_4^-)) = -6.45 +$ pH
11	$Cr_2O_7^{2-} + H_2O = CrO_4^{2-} + 2H^+$	$\log((CrO_4^{2-}) / (Cr_2O_7^{2-})) = -14.59 + 2$ pH
12	$Cr^{2+} = Cr^{3+} + e^-$	$E^{\circ} = -0.407 + 0.0591 \log((Cr^{3+}) / (Cr^{2+})$
15	$Cr^{2+} + 2H_2O = CrO_2^- + 4H^+ + e^-$	$E^{\circ} = -1.188 - 0.2364$ pH $+ 0.0519 \log((CrO_2^-) / (Cr^{2+}))$
16	$Cr^{3+} + 4H_2O = H_2CrO_4^0 + 6H^+ + 3e^-$	$E^{\circ} = 1.335 - 0.1182$ pH $+ 0.0197 \log((H_2CrO_4^0) / (Cr^{3+}))$
17	$Cr^{3+} + 4H_2O = HCrO_4^- + 7H^+ + 3e^-$	$E^{\circ} = 1.350 - 0.1379$ pH $+ 0.0197 \log((HCrO_4^-) / (Cr^{3+}))$
18	$2Cr^{3+} + 7H_2O = Cr_2O_7^{2-} + 14H^+ + 6e^-$	$E^{\circ} = 1.333 - 0.1379$ pH $+ 0.0098 \log((Cr_2O_7^{2-}) / (Cr^{3+}))$
19	$Cr^{3+} + 4H_2O = CrO_4^{2-} + 8H^+ + 3e^-$	$E^{\circ} = 1.477 - 0\text{-}1576$ pH $+ 0.0197 \log((CrO_4^{2-}) / (Cr^{3+}))$
26	$CrO_2^- + 2H_2O = CrO_4^{2-} + 4H^+ + 3e^-$	$E^{\circ} = 0.945 - 0.0788$ pH $+ 0.0197 \log((CrO_4^{2-}) / (CrO_2^-))$
27	$2CrO_2^- + 3H_2O = Cr_2O_7^{2-} + 6H^+ + 6e^-$	$E^{\circ} = 0.801 - 0.0591$ pH $+ 0.0098 \log((Cr_2O_7^{2-}) / (CrO_2^-))$
28	$CrO_3^{3-} + H_2O = CrO_4^{2-} + 2H^+ + 3e^-$	$E^{\circ} = 0.359 - 0.0394$ pH $+ 0.0197 \log((CrO_4^{2-}) / (CrO_3^{3-}))$
30	$2Cr + 3H_2O = Cr_2O_3^{\mathbf{a}} + 6H^+ + 6e^-$	$E^{\circ} = -0.654 - 0.0591$ pH
34	$2Cr^{3+} + 3H_2O = Cr_2O_3^{\mathbf{a}} + 6H^+$	$\log(Cr^{3+}) = 4.00 - 3$ pH
38	$Cr_2O_3 + 3H_2O = 2CrO_3^{3-} + 6H^+$	$\log(CrO_3^{3-}) = -52.15 + 3$ pH
39	Cr = Cr2+ + 2e-	$E^{\circ} = -0.913 + 0.0295 \log(Cr^{2+})$
42	$Cr + 3H_2O = CrO_3^{3-} + 6H^+ + 3e^-$	$E^{\circ} = 0.374 - 0.1182$ pH $+ 0.0197 \log(CrO_3^{3-})$
47	$2Cr^{2+} + 3H_2O = Cr_2O_3^{a} + 6H^+ + 2e^-$	$E^{\circ} = -0.136 - 0.1773$ pH $+ 0.0591 \log(Cr^{2+})$
52	$Cr_2O_3^{a} + 5H_2O = 2HCrO_4^- + 8H^+ + 6e^-$	$E^{\circ} = 1.259 - 0.0788$ pH $+ 0.0197 \log(HCrO_4^-)$
53	$Cr_2O_3^{a} + 4H_2O = Cr_2O_7^{2-} + 8H^+ + 6e^-$	$E^{\circ} = 1.242 - 0.0788$ pH $+ 0.0098 \log(Cr_2O_7^{2-})$
54	$Cr_2O_3^{a} + 5H_2O = 2CrO_4^{2-} + 10H^+ + 6e^-$	$E^{\circ} = 1.386 - 0.0985$ pH $+ 0.0197 \log(CrO_4^{2-})$

---

[a] Cr_2O_3 is used by Pourbaix (1966) to designate Cr_2O_3, $Cr(OH)_3$ and $Cr(OH)_3 \cdot nH_2O$, but with varying Gibbs free energy and enthalpy incorporated in the expression for each compound.